Computational Geodesy

Deterministic and Stochastic Approaches for the Integrated Modelling of Geodetic Earth Observation Data

Kumulative Habilitationsschrift
zur Erlangung der der Lehrbefähigung
im Fachgebiet Computational Geodesy
eingereicht an der
Agrar-, Ernährungs- und Ingenieurwissenschaftlichen Fakultät der
Rheinischen Friedrich-Wilhelms-Universität Bonn

von

Jan Martin Brockmann

aus Nachrodt-Wiblingwerde

Bonn 2026

Habilitationskolloquium: 26.11.2025

Abstract

THE OBSERVATION of the dynamically changing system Earth is one major task in geodesy. To measure the temporal changes globally, observations collected by satellites are analyzed to highlight the changes with respect to some long term mean, for instance comparing the measurements to reference surfaces. Furthermore, reference surfaces are required for the realization of reference systems, e.g. the geoid for the definition of the vertical datum. Therefore, an accurate knowledge of these reference surfaces is important in geodesy and other geoscientific disciplines, such as oceanography or geophysics.

This thesis covers the estimation of three different reference surfaces: the geoid — or more generally the Earth's gravity field, the Mean Dynamic ocean Topography (MDT), and the Mean Sea Surface (MSS). The basic idea for the determination of these reference surfaces is to formulate the problem as a (constrained) least squares parameter estimation problem. As a consequence of this design, a tailored parametric representation of the reference surface has to be established. In the framework of least squares estimation, it is immediately possible to account for the stochastic characteristics of the observations and to combine various complementary observation groups in a joint one-step estimation. The solution of the inverse problems becomes numerically and computationally demanding, as a large number of parameters (10^5 to 10^6) is required to adequately model the surfaces of interest. Furthermore, a huge number of (correlated) observations (10^7 to 10^8) has to be analyzed. Therefore, these challenges have to be solved utilizing specific numerical properties and High Performance Computing (HPC). In this context, the model design, the stochastic modelling and an efficient solution and implementation is referred to as *Computational Geodesy*.

The first reference surface studied in this contribution is the geoid. The main focus is on the computation of a static global gravity field model from the observations taken by the Gravity Field and Steady-State Ocean Circulation Explorer (GOCE) satellite. While the general idea is inline with the time-wise GOCE-only models published previously, the improved EGM_TIM_RL06 model benefits from reprocessed gravity gradients and a refined stochastic model. The approach is summarized and the improvements of the new model are presented. Additionally, it is shown how EGM_TIM_RL06 is used as input in the GOCO06S satellite-only model and aspects for the combination with terrestrial gravity data are discussed.

To estimate a geodetic MDT, a parametric least squares estimation approach is proposed and studied in different configurations. The proposed approach is used to jointly estimate the geoid and the MDT from altimetric Sea Surface Height (SSH) observations. A parameterization tailored to the characteristics of the MDT by a C^1-smooth linear combination of Finite Element (FE) basis functions is derived, which is used to approximate the unknown MDT surface. The approach enables to include information about the geoid as stochastic data sets and allows observations related to surface currents to be included (e.g. surface drifters or Synthetic Aperture Radar (SAR) derived Radial Surface Velocity (RSV)). It is shown with the help of simulated and real data experiments, that this kind of complementary observations strongly support the signal separation of the SSH into geoid and MDT.

Similarly, an alternative estimation approach to estimate a parametric MSS model is proposed and numerically studied. Although basically 'just' the temporal average of altimetric SSHs in the analysis period has to be computed, this is challenging due to the spatial and temporal sampling characteristics of the different altimetry missions. Therefore, it is shown how the ocean variability can be coestimated as an additional Sea Level Anomalies (SLAs) model. For both model components, MSS and MDT, a tailored continuous C^1-smooth FE model function is derived. In case of the SLA, it is extended towards a spatio-temporal model using separable basis functions. Numerical real data studies are used to demonstrate the performance of the proposed approach.

For all applications studied, it can be concluded that the parametric approaches accounting for the stochastic characteristics of the observations and using the developed parametric models are well suited and offer advantages compared to the existing (grid based) approaches.

Acknowledgments

This work was made possible via the direct and indirect financial support of several granted projects. The European Space Agency supported the work via the GOCE High Level Processing Facility (Main Contract No. 18308/04/NL/MM). The funding by the DFG in scope of the project PARASURV (Grant BR5470/1-1) is gratefully acknowledged. Additional financial support was received from TRA Modelling (University of Bonn) as part of the Excellence Strategy of the federal and state governments for the project "Development of Continuous Spatio-Temporal Finite Element Based Models for Sea Surface Approximation". The project STAMPED was supported by TRA Modelling and the CRC 1502 DETECT (funded by DFG). Contributions from the DFG funded project NonStopLSC are acknowledged (SCHU 2305/7-1).

The numerical results were obtained with the help of various computing resources. I would like to thank the Gauss Centre for Supercomputing e.V. (`www.gauss-centre.eu`) for funding the work by providing computing time through the John von Neumann Institute for Computing (NIC) on the GCS Supercomputer JURECA/JUWELS at Jülich Supercomputing Centre (JSC). Additionally, I would like to thank the University of Bonn for hosting and granting access to the Bonna cluster and to the DFG for funding the institute/faculty cluster via a Forschungsgroßgeräteantrag (INST 217/749-1 FUGG).

Furthermore, the analyzed data sets were preprocessed and provided by different institutions. The altimetry products were produced and distributed by Aviso+ (`https://www.aviso.altimetry.fr/`), as part of the Ssalto ground processing segment. The used GOCE L1B and L2 input data are freely provided by ESA via the GOCE Online Dissemination Service (`https://goce-ds.eo.esa.int/oads/access/`).

I would like to thank all co-authors of the included manuscripts for the joint work and the fruitful discussions and all partners in the involved projects. Special thanks to Torsten Mayer-Guerr (IfG, TU Graz) for the SST-hl contributions to the GOCE models and Andreas Kvas (IfG, TU Graz) for the efforts in the context of the GOCO project. Thanks to all GOCE High Level Processing Facility team members for the excellent collaboration, e.g. in the context of model validation and for providing feedback. Additionally, I want to thank Sandrine Mulet (CLS) for providing and discussing drifter derived surface current data and Artem Moiseev (NERSC) for the discussions about the Doppler derived radial surface velocity products.

This thesis would not have been possible without Christian Neyers, Moritz Borlinghaus and Lukas Jendges, who have done a great job in performing most of the project work, and have always been a pleasure to work with. Furthermore, I want to thank all members of the (former) Theoretical Geodesy group, most recently Johannes Korte and Till Schubert for the joint work and all the discussions, and Silvia Müller who did the initial work introducing me to geodetic MDT determination. Many thanks to the administrative staff, especially Janina, Sandra, Cathrin and Michael for all the support over the years. Thanks to Bernd for reading the thesis and all the discussions about everything. Similarly, many thanks to all my other colleagues from the institute, faculty and university, for the joint work, discussions and conversations in the last years.

Biggest thanks go to Wolf-Dieter Schuh for all the support, guidance and patience. As a great supervisor and mentor, he provided me with the independence and freedom to pursue my own ideas, while offering support whenever needed. It was a great pleasure learning from and working with him!

Finally, I want to thank Susanne Glaser for adopting me in the new Space Geodesy Group, making it possible to complete the thesis and to continue my work. I am looking forward to contributing to the success of the new group with my knowledge and experience, while getting in touch with new applications and problems in the context of space geodetic techniques!

Contents

Publication List of the Cumulative Habilitation

Peer-reviewed articles (journal and book)

Becker, S., J. M. Brockmann, and W.-D. Schuh (2014a). “Mean Dynamic Topography Estimates Purely Based on GOCE Gravity Field Models and Altimetry.” In: *Geophysical Research Letters* 41.6, pp. 2063–2069. DOI: `10.1002/2014GL059510`.

Becker, S., M. Losch, J. M. Brockmann, G. Freiwald, and W.-D. Schuh (2014b). “A Tailored Computation of the Mean Dynamic Topography for a Consistent Integration into Ocean Circulation Models.” In: *Surveys in Geophysics* 35.6, pp. 1507–1525. DOI: `10.1007/s10712-013-9272-9`.

Borlinghaus, M., C. Neyers, and J. M. Brockmann (2023a). “Development of a Continuous Spatiotemporal Finite Element-Based Representation of the Mean Sea Surface.” In: *Journal of Geodesy* 97.2, p. 16. DOI: `10.1007/s00190-023-01709-1`.

Brockmann, J. M., T. Schubert, and W.-D. Schuh (2021). “An Improved Model of the Earth’s Static Gravity Field Solely Derived from Reprocessed GOCE Data.” In: *Surveys in Geophysics* 42.2, pp. 277–316. DOI: `10.1007/s10712-020-09626-0`.

Fecher, T., R. Pail, T. Gruber, and the GOCO Consortium (2017). “GOCO05c: A New Combined Gravity Field Model Based on Full Normal Equations and Regionally Varying Weighting.” In: *Surveys in Geophysics* 38.3, pp. 571–590. DOI: `10.1007/s10712-016-9406-y`.

Kvas, A., J. M. Brockmann, S. Krauss, T. Schubert, T. Gruber, U. Meyer, T. Mayer-Gürr, W.-D. Schuh, A. Jäggi, and R. Pail (2021). “GOCO06s – a Satellite-Only Global Gravity Field Model.” In: *Earth System Science Data* 13.1, pp. 99–118. DOI: `10.5194/essd-13-99-2021`.

Neyers, C. and J. M. Brockmann (2024). “Radial Surface Currents from Space: An Opportunity for Mean Dynamic Topography Estimation?” In: *Advances in Space Research* 74.4, pp. 1563–1575. DOI: `10.1016/j.asr.2024.05.041`.

Schubert, T., J. Korte, J. M. Brockmann, and W.-D. Schuh (2020). “A Generic Approach to Covariance Function Estimation Using ARMA-Models.” In: *Mathematics* 8.4, p. 591. DOI: `10.3390/math8040591`.

Schuh, W.-D. and J. M. Brockmann (2018). “The Numerical Treatment of Covariance Stationary Processes in Least Squares Collocation.” In: *Handbuch der Geodäsie: 6 Bände*. Ed. by W. Freeden and R. Rummel. Springer Reference Naturwissenschaften. Springer Berlin Heidelberg, pp. 1–36. DOI: `10.1007/978-3-662-46900-2_95-1`.

Peer-reviewed conference proceedings

Borlinghaus, M., C. Neyers, and J. M. Brockmann (2023b). “Refinement of Spatio-Temporal Finite Element Spaces for Mean Sea Surface and Sea Level Anomaly Estimation.” In: *X Hotine-Marussi Symposium on Mathematical Geodesy*. Ed. by J. T. Freymueller and L. Sánchez. Springer International Publishing, pp. 119–128. DOI: `10.1007/1345_2023_205`.

Brockmann, J. M., M. Borlinghaus, C. Neyers, and W.-D. Schuh (2023). “On the Coestimation of Long-Term Spatio-Temporal Signals to Reduce the Aliasing Effect in Parametric Geodetic Mean Dynamic Topography Estimation.” In: *X Hotine-Marussi Symposium on Mathematical Geodesy.* Ed. by J. T. Freymueller and L. Sánchez. Springer International Publishing, pp. 129–137. DOI: `10.1007/1345_2023_224`.

Korte, J., J. M. Brockmann, and W.-D. Schuh (2023a). “A Comparison between Successive Estimate of TVAR(1) and TVAR(2) and the Estimate of a TVAR(3) Process.” In: *Engineering Proceedings* 39.1, p. 90. DOI: `10.3390/engproc2023039090`.

Korte, J., T. Schubert, J. M. Brockmann, and W.-D. Schuh (2021). “A Mathematical Investigation of a Continuous Covariance Function Fitting with Discrete Covariances of an AR Process.” In: *Engineering Proceedings* 5.1, p. 18. DOI: `10.3390/engproc2021005018`.

— (2023b). “On the Estimation of Time Varying AR Processes.” In: *X Hotine-Marussi Symposium on Mathematical Geodesy.* Ed. by J. T. Freymueller and L. Sánchez. Springer International Publishing, pp. 113–118. DOI: `10.1007/1345_2023_188`.

Schubert, T., J. M. Brockmann, J. Korte, and W.-D. Schuh (2021a). “On the Family of Covariance Functions Based on ARMA Models.” In: *Engineering Proceedings* 5.1, p. 37. DOI: `10.3390/engproc2021005037`.

Schubert, T., J. M. Brockmann, and W.-D. Schuh (2021b). “Identification of Suspicious Data for Robust Estimation of Stochastic Processes.” In: *IX Hotine-Marussi Symposium on Mathematical Geodesy.* Ed. by P. Novák, M. Crespi, N. Sneeuw, and F. Sansò. International Association of Geodesy Symposia. Cham: Springer International Publishing, pp. 199–207. DOI: `10.1007/1345_2019_80`.

Schuh, W.-D., J. Korte, T. Schubert, and J. M. Brockmann (2023). “Modeling of Inhomogeneous Spatio-Temporal Signals by Least Squares Collocation.” In: *X Hotine-Marussi Symposium on Mathematical Geodesy.* Ed. by J. T. Freymueller and L. Sánchez. Springer International Publishing, pp. 149–158. DOI: `10.1007/1345_2023_202`.

Data sets citable with DOI

Brockmann, J. M., T. Schubert, T. Mayer-Gürr, and W.-D. Schuh (2019d). *The Earth’s Gravity Field as Seen by the GOCE Satellite - an Improved Sixth Release Derived with the Time-Wise Approach (GO_CONS_GCF_2_TIM_R6).* DOI: `10.5880/icgem.2019.003`.

Kvas, A., T. Mayer-Gürr, S. Krauss, J. M. Brockmann, T. Schubert, W.-D. Schuh, R. Pail, T. Gruber, A. Jäggi, and U. Meyer (2019b). *The Satellite-Only Gravity Field Model GOCO06s.* DOI: `10.5880/icgem.2019.002`.

Pail, R., T. Gruber, T. Fecher, and the GOCO Consortium (2016). *The Combined Gravity Model GOCO05c.* DOI: `10.5880/icgem.2016.003`.

Zingerle, P., J. M. Brockmann, R. Pail, T. Gruber, and M. Willberg (2019). *The Polar Extended Gravity Field Model TIM_R6e.* DOI: `10.5880/ICGEM.2019.005`.

Miscellaneous contributions[1]

Borlinghaus, M., C. Neyers, and J. M. Brockmann (2022a). *Schätzung eines kontinulierlichen raumzeitlichen Modells der Meeresoberfläche.* Talk at Frontiers of Geodetic Science. Essen, Germany.

— (2022b). *Towards the Development of a Continuous Spatio-Temporal Finite Element Based Representation of the Mean Sea Surface.* Technical Report IGG-TG-2022-01. Bonn, Germany: University of Bonn, Institute of Geodesy and Geoinformation. HDL: `20.500.11811/9592`. URL: `https://hdl.handle.net/20.500.11811/9592`.

---

[1] The thesis explicitly contains results, materials and findings taken from the preprints, reports, talks and posters collected as *miscellaneous contributions.* To correctly reference these studies and to acknowledge all authors, these are added as an extra category here.

Brockmann, J. M., M. Borlinghaus, C. Neyers, and W.-D. Schuh (2022). *On the Use of Surface Current Observations for the Joint Estimation of Geodetic Mean Dynamic Topography Models and the Geoid.* Poster at the World Ocean Circulation User Consultation Meeting. Frascati, Italy.

Brockmann, J. M., S. Müller, and W.-D. Schuh (2016). *Analysis and Refinement for an Integrated Approach Estimating the Ocean's MDT from Altimetry and GOCE.* Poster. Poster at the ESA Living Planet Symposium. Preague, Czech Republic.

Brockmann, J. M., C. Neyers, and W.-D. Schuh (2019a). *A Parametric Representation to Integrate Current Observations into the Estimation of the Mean Dynamic Topography.* Poster. Poster at the World Ocean Circulation User Consultation Meeting. Frascati, Italy.

Brockmann, J. M., T. Schubert, and W.-D. Schuh (2019b). *Gravity Field Processing with the Time-Wise Approach - the Time-Wise RL06 Release Candidate Solution(s).* Talk at ESA HPF CCN10 Final Meeting. online.

Brockmann, J. M. and W.-D. Schuh (2016a). "Computational Aspects of High-Resolution Global Gravity Field Determination - Numbering Schemes and Reordering." In: *NIC Symposium 2016.* Ed. by K. Binder, M. Müller, M. Kremer, and A. Schnurpfeil. Vol. 48. NIC Series. Jülich, Germany.

— (2016b). *Stochastic Modeling of Altimetric Sea Surface Height Measurements - Refined AR Models from Iterative Residual Analysis.* Talk. Talk at Gravity, Geoid and Height Systems. Thessaloniki, Greece. HDL: `20.500.11811/9495`. URL: `https://hdl.handle.net/20.500.11811/9495`.

Brockmann, J. M., W.-D. Schuh, and B. Kargoll (2015). *A Case Study on the Potential of Robust Decorrelation Filter Design for a Reprocessing of a Gravity Field Model from GOCE Data.* Talk. Talk at the EGU General Assembly. Vienna, Austria. URL: `http://presentations.copernicus.org/EGU2015-12307_presentation.pdf`.

Brockmann, J. M., W.-D. Schuh, and W. Team (2017). *Improving the Official GOCE-only Gravity Field Model - Strategies Inline with the 'classical' Time-Wise Rocessing.* Talk at the ESA HPF Reprocessing Workshop. Munich, Germany.

Gruber, T. and G. H. Team (2018). *The GOCE Reprocessing Campaign.* Talk. Vienna, Austria. URL: `https://mediatum.ub.tum.de/1437641`.

Jendges, L. and J. M. Brockmann (in review). "Refining Linear Trend Estimates from One Dimensional Time Series Data with Autoregressive Covariance Modelling - An Application to GRACE Total Water Storage Time Series Data." In: *Stochastic Environmental Research and Risk Assessment* preprint. DOI: `10.21203/rs.3.rs-5439927/v1`.

Neyers, C., M. Borlinghaus, and J. M. Brockmann (2022a). *Exploring the Opportunities of Geostrophic Current Observations from Space in the Joint Estimation of Mean Dynamic Topography and Geoid Undulation.* Poster at the ESA Living Planet Symposium. Bonn, Germany.

— (2022b). *About the Potential of Satellite-based One-dimensional Geostrophic Current Observations to Improve the Separation of the Mean Dynamic Topography and Geoid Undulation.* Poster at the X Hotine-Marussi Symposium. Milano, Italy.

Neyers, C., J. M. Brockmann, and W.-D. Schuh (2019). *Parametric Finite Element Based Models to Represent the Mean Dynamic Ocean Topography.* Poster at the ESA Living Planet Symposium. Milano, Italy.

Schuh, W.-D. and J. M. Brockmann (2016). *Refinement of the Stochastic Model for GOCE Gravity Gradients by Nonstationary Decorrelation Filters.* Poster. Poster at the ESA Living Planet Symposium. Prague, Czech Republic.

Schuh, W.-D., J. Franken, J. M. Brockmann, C. Esch, and J. Köhler (2018). *Design of Frequency Selective Filters for Non-Equispaced Data.* Talk at the IX Hotine-Marussi Symposium. Rome, Italy. URL: `https://doi.org/10.48565/bonndoc-43`.

Chapter 1

Introduction, Motivation and Contributions

1.1 Introduction and Motivation

Monitoring changes in the system Earth on all spatial and temporal scales is a key task of geodesy (Müller et al., 2022). To represent and quantify the changes, reference systems — or more specifically in the context of this thesis reference surfaces — are essential (Plag and Pearlman, 2009; Rothacher et al., 2011). In this thesis, three important reference surfaces are of interest: (i) the (static) geoid (or gravity field), (ii) the Mean Dynamic ocean Topography (MDT) and (iii) the Mean Sea Surface (MSS). All these reference surfaces have in common that they reflect the long-term mean with respect to a specific reference period.

These reference surfaces can be used to characterize the long-term or steady-state signals. Examples are the unification of global height systems using the geoid as reference (e.g. Gruber et al., 2012; Gerlach and Rummel, 2013), or the determination of steady-state ocean circulation from the MDT (e.g. Volkov and Zlotnicki, 2012; Rio et al., 2014). Another example for the application of the MSS is the determination of the MDT applying a multi-step approach (e.g. Knudsen et al., 2011; Mulet et al., 2021b), or the recovery of the marine gravity field (e.g. Hwang et al., 2002).

The reference surfaces can serve as the input for studies on the changes and the temporal behavior of the modeled signals. These studies are typically performed on the level of anomalies relative to these mean reference surfaces. Examples are studies of mass redistribution and corresponding variations of (temporal) gravity anomalies (e.g. Kusche et al., 2014; Pail et al., 2015) for climate studies (e.g. Jensen et al., 2019), hydrology (e.g. Sneeuw et al., 2014; Döll et al., 2014) or cryospheric studies (Baur, 2013; Talpe et al., 2017). The MSS is used as a reference for sea level studies, for example based on altimetric Sea Level Anomalies (SLAs) (see e.g. Nerem et al., 2018; Uebbing et al., 2019).

This contribution will not focus on the applications of the different reference surfaces, but rather on methodological aspects of the representation and the estimation of the actual reference surfaces. Within the "geodetic approaches" (e.g. for the MDT see Chapter 4 and Albertella et al., 2008), observational data are used for the estimation. Different functionals are combined in the estimation approach to determine a representation of the reference surface. As the observations are typically considered as a realization of a random variable, uncertainties can be propagated throughout the estimation process. Consequently, uncertainty estimates can be provided as quality description for the resulting reference surfaces (e.g. Kvas et al., 2019a; Becker et al., 2012).

The estimation of the reference surfaces can be done utilizing either deterministic or stochastic approaches. In the deterministic approaches, the reference surfaces are represented by a parametric mathematical function. Its parameters are estimated from the observations via the solution of an inverse problem. This results in a kind of large dimensional approximation – or data fitting – problem, which is solved by applying for instance the least squares principle. As an alternative, stochastic approaches like Least Squares Collocation (LSC) or Kriging exist (Moritz, 1973; Wackernagel, 2010). Instead of choosing a continuous parametric approximation function, stochastic approaches utilize the covariance structures of the signal and the data as a measure for spatial similarity to predict a filtered version of the signal at an arbitrary point in the domain of interest.

In the examples considered here, the complexity of the approximation problem is increased, as the estimations of the mean surfaces contain a signal separation task. In other words, the functional of the target signal is not observed directly, but it is disturbed by signals, which have to be accounted for. This can be a dominant noise (as can be seen in the gravity field example, cf. Chap. 3); temporal signals resulting from physical dynamics (as can be seen in the MSS and MDT examples, cf. Chap. 4 and 5); or multiple signals of interest (as shown later in the MSS estimation example, cf. Chap. 5).

Especially since the launch of the dedicated gravity field satellite missions, starting with the CHAllenging Minisatellite Payload (CHAMP) mission in 2000 (Reigber et al., 1999), continued by Gravity Recovery and Climate Experiment (GRACE) (Tapley et al., 2004), the Gravity Field and Steady-State Ocean Circulation Explorer (GOCE) and currently by GRACE Follow-On (GRACE-FO) (Landerer et al., 2020) the determination of global gravity field models made a huge progress (Rummel, 2020; Flechtner et al., 2021). As the gravity field can not be observed directly, the effect of the gravity field on the satellite and/or specific on board test masses are observed. This is realized via the observation of orbit perturbations (for CHAMP, GRACE, GRACE-FO and GOCE, see e.g. Baur et al., 2014; Jäggi et al., 2015), the relative distance (change) of two satellites (for GRACE and GRACE-FO, see e.g. Kvas et al., 2019a) or via Satellite Gravitational Gradiometry (SGG) as realized with the GOCE mission (Rummel et al., 2011; Pail et al., 2011). From all these missions, the static gravity field can be determined (despite the main focus of GRACE being the time-variable gravity field to monitor mass changes) from solving an ill-posed inverse problem.

Due to the different measurements principles utilized, mission specific quality characteristics and sensitivity of the instruments exist by design. In a first step, typically mission-only solutions are derived by processing centers and scientific institutions (e.g. Reigber et al., 2003; Kvas et al., 2019a; Pail et al., 2011). For the global solutions, mostly deterministic approaches are applied, where the Earth's gravity field is represented as a finite series of spherical harmonic base functions (e.g. Heiskanen and Moritz, 1993). This is, depending on the spatial resolution and the number of available observations (in the order of 10^8), a computational challenging inverse problem, especially as the individual measurements are often highly correlated. Only in case a high-quality stochastic model is used in the analysis of the individual missions, it is possible to derive a realistic covariance matrices of the spherical harmonic parameters. With that available, it is quite straight forward to combine the solutions in a second step on the level of normal equations to obtain a satellite-only gravity field solution which combines all the advantages of the individual missions (Pail et al., 2010; Meissl, 1982).

The so called 'geodetic MDT' estimation relies on availability of a gravity field model and altimetric Sea Surface Height (SSH) observations. The geodetic estimation of the MDT as the difference between the temporal mean of SSH and the geoid remains, despite the simple relation, still a difficult task (Albertella et al., 2008; Bosch and Savcenko, 2010). Mainly, the spectral inconsistency between the available altimetric SSH observations and the geoid information leads to problems in the separation process. This is caused by the accuracy characteristics of the satellite derived geoid information, as it is only sufficiently accurate for a resolution of about 100 km. In contrast to the gravity field, there exists no physically motivated natural choice of basis functions to represent the MDT as a function, consequently stochastic approaches are often used for the computation of state-of-the-art models (e.g. Mulet et al., 2021b; Andersen and Knudsen, 2009). These approaches consider the geoid as known, e.g. from a global gravity field model, without considering improvements based on the SSH observations. The estimated MDT is the spatially and temporally filtered difference between the SSH and the geoid. This spatial and temporal filtering of the along-tack SSH measurements is often done in a separate processing step.

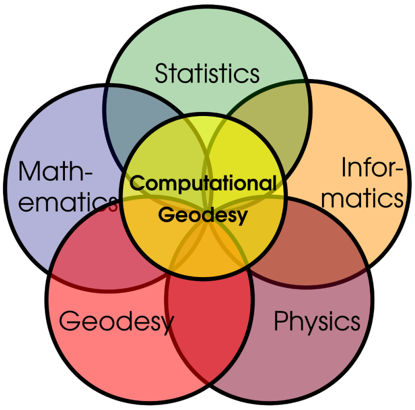

Figure 1.1: *Computational Geodesy*, at the interface between geodesy, statistics, mathematics, informatics and physics.

The temporal averaged and gridded product is defined as the MSS, containing the temporal averaging and geophysical corrections of the SSH observations from various altimetry missions with significantly different spatial and temporal sampling characteristics (Andersen et al., 2021). The challenge in MSS estimation is the joint analysis of Exact Repeat Missions (ERMs), which are important for temporal averaging and Geodetic Missions (GMs) (or at least GM phases) which are important to obtain a sufficient spatial sampling. As for the MDT, stochastic approaches are often applied in the established procedures, as again no natural and physically motivated set of basis functions exists to represent the MSS (Andersen et al., 2015; Pujol et al., 2018).

Based on the discussions above, the established procedures are multi-step approaches. I.e. for the MDT example, the gravity field is determined in a first step. In the second step, the MSS is determined from the SSH observations. Finally, in a third step, the geoid is introduced as fixed, without updates and often without accounting for its uncertainties to estimate the MDT from the difference to the MSS; similarly, uncertainties of the MSS are also often not accounted for. Additionally, when estimating the MSS, the SSH observations are corrected for temporal ocean variability (i.e. the so called SLA) and other geophysical signals as a preprocessing step.

Within this thesis, contributions towards a more rigorous processing and estimation of the geodetic reference surfaces are collected. This comprises methodological developments, which are introduced in steps to demonstrate the applicability and to decrease the numerical complexity. In general, several aspects are involved, bringing together concepts and tools from various disciplines,

(i) problems relevant for geodesy,
(ii) the model design, requires concepts and tools from mathematics and scientific computing while accounting for physical laws and properties,
(iii) the stochastic modeling, requires concepts and tools from statistics and mathematics,
(iv) the efficient numerical solutions and computations, require strategies from scientific computing, mathematics and algorithms from informatics,
(v) an efficient numerical implementation requires concepts and libraries from High Performance Computing (HPC) and strategies established in scientific computing and informatics.

The combination of all these are referred to as *Computational Geodesy* (cf. Fig. 1.1).

1.2 Contributions

As demonstrated in the introduction the geoid, the MDT and the MSS are important reference surfaces. Over the ocean, these three reference surfaces are connected and (indirectly) observable via altimetric instantaneous SSH observations. Mathematically speaking, the SSH at a location $(\lambda,\, \phi)$ in ellipsoidal coordinates at epoch t can be represented as a continuous, but unknown spatio-temporal function

$$f_{\text{SSH}}\left(\lambda,\, \phi,\, t\right) = f_{\text{MSS}}\left(\lambda,\, \phi\right) + f_{\text{SLA}}\left(\lambda,\, \phi,\, t\right), \tag{1.1}$$

which results from the definition of the MSS and the SLA respectively (see for instance Aviso, 2020). Note that by definition of the altimetry community, the SSH measurements are already corrected for solid earth tides, Ocean Tides (OT), pole tides, atmospheric effects etc. (e.g. Jason-3 Team, 2021), thus they are not included in this (idealized) function. Again, f_{MSS} is an unknown spatial and f_{SLA} a generally unknown spatio-temporal function, which represent the MSS and SLA, respectively.

Introducing the definition of the MDT as the difference between the MSS and the (static) geoid written as function yields

$$f_{\text{MDT}}\left(\lambda,\, \phi\right) := f_{\text{MSS}}\left(\lambda,\, \phi\right) - N\left(\lambda,\, \phi\right), \tag{1.2}$$

where the function $N\left(\lambda,\, \phi\right)$ represents the geoid. In combination with (1.1) it becomes

$$f_{\text{SSH}}\left(\lambda,\, \phi,\, t\right) = N\left(\lambda,\, \phi\right) + f_{\text{MDT}}\left(\lambda,\, \phi\right) + f_{\text{SLA}}\left(\lambda,\, \phi,\, t\right). \tag{1.3}$$

Again, $f_{\text{MDT}}\left(\lambda,\, \phi\right)$ is an unknown spatial function which represents the MDT.

In contrast, for the geoid $N\left(\lambda,\, \phi\right)$ a proper representation as a spherical harmonic series is well established via the harmonicity of the gravitational potential (e.g. Hofmann-Wellenhof and Moritz, 2005, Sect. 2.5, 2.13).

The deterministic and stochastic analysis of SSH measurements and the relations from (1.2) to (1.3) serve as the basis for the contributions of this thesis. They can be formally grouped into five major parts.

Estimation of global gravity field models with realistic uncertainty description

To separate the left hand side of (1.3) into geoid and MDT (and SLA), an accurate knowledge of the geoid is required. In case (1.3) is used as the basis for least squares observation equations of altimetric SSH observations (cf. Chapter 4) complementary information/observations sensitive to the geoid are required to solve the adjustment problem for the geoid and the MDT. When introducing satellite derived gravity field information into the adjustment, e.g. in form of already preprocessed normal equations (**Becker et al., 2014b; Becker et al., 2014a**), a high quality covariance modeling and careful propagation throughout the analysis procedure is essential.

In **Brockmann et al., 2021** and **Brockmann et al., 2019d**, an improved satellite-only gravity field model from GOCE observations is derived. It is the sixth release of the so called GOCE time-wise (GOCE-TIM) gravity field models which are internationally well established, and also the only existing GOCE-only gravity field model computed from the entire reprocessed mission data set. Despite using re-calibrated input observations, the stochastic modeling of the gravity gradients is significantly improved (**Schubert et al., 2021b**) which results in a high-quality covariance matrix of the model. This allows one to substitute the original observations by the model without loss of information and to still use it as a stochastic data set in the further applications.

To compensate for mission specific weaknesses, the model is extended and stabilized with ground data in polar regions (**Zingerle et al., 2019**); or it is alternatively combined with models derived from the other dedicated gravity field missions in the framework of the Gravity Observation COmbination (GOCO) consortium (**Kvas et al., 2021**). The most recent model GOCO06S (**Kvas et al., 2019b**) is one of the most accepted satellite-only gravity field models currently available and serves as a basis for many applications. Additionally, in **Fecher et al., 2017** the predecessor model GOCO05S is combined with terrestrial data, to obtain a combined global gravity field model GOCO05C (**Pail et al., 2016**). Again, due to the efforts in stochastic modeling, the strengths of the individual input data sets are optimally exploited.

Establishing finite element based basis functions for spatial and spatio-temporal approximation tasks

As mentioned above, there is no natural choice of basis functions to represent f_{MDT}, f_{MSS} and f_{SLA}. Instead, it is required to approximate the unknown function space and its characteristics by well suited basis functions. Within this thesis, Finite Element Spaces (FESs) are studied for that purpose. Basis functions as known from the Finite Element Method (FEM) are used as local basis functions to compose the unknown function space.

Whereas in **Becker et al., 2014a** and **Becker et al., 2014b** linear, i.e. C^0-smooth elements are used to represent the MDT, this is extended to C^1-smooth spaces in **Neyers and Brockmann, 2024** and **Brockmann et al., 2023**. The C^1-smooth elements applied to the MDT are transferred to approximate the MSS in **Borlinghaus et al., 2023a** and **Borlinghaus et al., 2023b**. Additionally, these are extended to spatio-temporal functions to represent the SLA with different filtering characteristics.

Establishing deterministic finite element based approaches for the joint estimation of the geoid and the MDT

In most geodetic approaches for MDT estimation, the geoid is not updated within the estimation. Using an integrated deterministic approach, i.e. setting up a parametric model for the MDT and setting up least squares observation equations based on (1.3), allows for a joint estimation of both – the geoid and MDT. This is started in **Becker et al., 2014b** and **Becker et al., 2014a** and continued in **Neyers and Brockmann, 2024** and **Brockmann et al., 2023**.

Despite the joint estimation using FESs (cf. **Becker et al., 2014b**), the use of satellite-only gravity field information as a stochastic data set (see **Becker et al., 2014a**), the co-estimation of filtered long-term SLA (**Brockmann et al., 2023**) and the flexible use of C^1-smooth FESs, the key contribution is the in-situ assimilation of surface currents. As these can be linked in geostrophic approximation to the gradient of the MDT, the separation of the SSH into geoid and MDT is strongly supported (**Neyers and Brockmann, 2024**). Adding both, stochastic satellite-based gravity field information, which is only sensitive for the geoid, and surface drifters or Synthetic Aperture Radar (SAR) derived Radial Surface Velocities (RSVs) (see **Neyers and Brockmann, 2024; Brockmann et al., 2022; Brockmann et al., 2019a; Neyers et al., 2022b**) as complementary data types to the analysis of the SSH significantly improves the separation. Consequently, it is shown in simulation scenarios and real data analysis that both, MDT and geoid solutions, are improved.

A deterministic approach for MSS determination including a coestimation of a spatio-temporal model of the ocean variability

The successful modeling of MDT with the C^1-smooth FESs serves as the motivation to study the applicability of this representation for the MSS. In **Borlinghaus et al., 2023a**, spatial FESs are used to represent the MSS. The joint use of altimetric SSH measurements from ERMs and GMs is required to obtain a sufficient spatial and temporal coverage. Whereas the first are required to obtain a sufficient temporal sampling, the latter are required to obtain the required spatial resolution of a few kilometers. As the GMs have a poor temporal sampling, the temporal variability of the ocean has to be considered to avoid an aliasing problem.

In **Borlinghaus et al., 2023a** least squares observation equations are formulated based on (1.2) to estimate a continuous spatial model for the MSS and a continuous spatio-temporal model for SLA. Thus, the ocean variability is co-estimated from the data. Despite identifying a proper spatial resolution for the MSS and for the SLA, mainly via the choice of a triangulation for the Finite Elements (FEs) (cf. **Borlinghaus et al., 2023b**), the spatio-temporal model component for the SLA is designed from separable functions in the spatial and the temporal domain. Various basis functions are studied in the combination and it is shown that the combination of C^1-smooth FEs in the spatial and finite B-Splines in the temporal domain yields the highest-quality MSS and filtered SLA estimates (**Borlinghaus et al., 2023a**).

Methodological and implementational contributions for the solution of large-dimensional deterministic approximation problems including advanced stochastic modeling

As discussed above, mainly parametric approaches are used in the applications for gravity field recovery, geodetic MDT estimation and for joint MSS and SLA determination. In contrast to the established grid based stochastic approaches, which are often processed in patches, it is required to solved large, overdetermined systems of equations, which include a signal separation problem. Hundreds of thousands parameters have to be estimated from millions of observations. This requires the implementation of dedicated massive parallel algorithms in HPC environments, for which the developments from the PhD thesis serve as a basis (Brockmann, 2014).

Whenever observations with different characteristics and sensitivity are combined in a joint adjustment, the stochastic modeling of the observations is essential to optimally exploit the strengths – and to suppress the weaknesses – of the individual data sets. In this context, the stochastic approaches enter this thesis. The relative weighting of the input data sets and the uncertainty characteristics are typically described by the stochastic model. Different strategies exists, to describe the correlations and covariances in the data and to apply them in the decorrelation process. One can distinguish between the filter and the covariance approach (see **Schuh and Brockmann, 2018**), which both have their pros and cons in the context of decorrelation in least squares problems. While the filter approach uses digital filters to remove the correlations, the covariance approach use the covariance matrix, e.g. derived from covariance functions iteratively fitted to the least squares residuals. Different strategies exist to estimate the filters or covariances. One strategy is the approximation of the least squares residuals by either AutoRegressive (AR) or AutoRegressive Moving Average (ARMA) processes. The processes are iteratively adjusted to the residuals, which can be seen as a realization of the estimate for the noise (e.g. as applied in **Brockmann et al., 2016; Brockmann and Schuh, 2016b**). The estimation can be refined in various ways, e.g. robustifying the estimation of the process coefficients, which directly detects outliers and suspicious data (**Schubert et al., 2021b; Brockmann et al., 2021**) or accounting for non-stationarity introducing a family of time-variable processes (**Korte et al., 2023b; Schuh et al., 2023**).

Using the stochastic processes, there is a close connection between the processes themselves and corresponding families of covariance functions, which are theoretically studied for AR and ARMA processes in (**Korte et al., 2021; Schubert et al., 2021a; Schubert et al., 2020**). This allows a switch between the representations and provides a valid interpolation between discrete covariance functions.

1.3 Structure of the Thesis

In contrast to the formulation of the five main contributions, the thesis is more organized with respect to the research projects and the applications (gravity field, MDT and MSS) as most of the publications are focused on an application.

The methodological contributions are thus spread across the various publications. To support this, Chapter 2 provides the required general theoretical background and introduces the methodological contributions in a generic way. Starting with Chapter 3, the specific applications are discussed, covering the satellite-based gravity field determination with an advanced uncertainty modeling. In addition to the numerical and computational characteristics of the approximation problem, the obtained results from the real-data analysis are summarized. Starting with the GOCE time-wise release six model and the underlying project, the chapter is concluded with the combined GOCO06S global satellite-only gravity field model and the progress achieved. As this serves as stochastic input for the proposed parametric geodetic MDT estimation approach, this and the underlying research project are introduced in more detail in Chapter 4. After discussing numerical and computational challenges and the chances and limitations of the proposed approach, the obtained results for the geoid and the MDT are examined. Depending on data availability and its quality, either simulation scenarios or real-data scenarios are analyzed for different promising data sets and in different regions of interest. In Chapter 5, the FE based modeling approach is transferred to the estimation of a model of the MSS. As in the proposed modeling approach only finite basis functions are involved, the numerical and computational characteristics are significantly different. Thus, the specific numerical and computational challenges are discussed. It is shown that the co-estimation of a spatio-temporal SLA, composed from separable basis function for the spatial and temporal domain, significantly improves the MSS estimate as it reduces the aliasing problem. Finally, Chapter 6 summarizes the contributions of this thesis, draws some conclusions and provides further ideas for future research projects for which the thesis can serve as the basis.

Chapter 2

Theoretical Background and Common Methodological Contributions

This chapter summarizes the general theoretical background and the corresponding notations which are common to the applications discussed in the following chapters.

2.1 Background and Notation

All the applications discussed in Chapters 3, 4 and 5 involve a large dimensional adjustment problem. The reference surfaces – either the gravity field/geoid, the MDT or MSS – are represented as linear combination of basis functions. The scaling coefficients of the basis functions are supposed to be estimated as unknown parameters $\tilde{\boldsymbol{\mathcal{X}}}$ in an adjustment procedure using the stochastic view. These parameters are estimated from observations $\boldsymbol{\mathcal{L}}$ which can be linked to the parameters via the design matrix $\mathbf{A}$, possibly after a linearization. The vector of observations is represented as a random variable (calligraphic)

$$\boldsymbol{\mathcal{L}} = \boldsymbol{\lambda} + \boldsymbol{\mathcal{E}}, \tag{2.1}$$

with

$$\boldsymbol{\lambda} = \mathbf{A}\boldsymbol{\xi} \tag{2.2}$$

the true values of the observations, $\boldsymbol{\xi}$ the true parameters and $\boldsymbol{\mathcal{E}}$ the random variable which represents the measurement errors.

It is assumed that $E\left\{\boldsymbol{\mathcal{E}}\right\} = \mathbf{0}$, such that $E\left\{\boldsymbol{\mathcal{L}}\right\} = \boldsymbol{\lambda}$. Therfore, the variance of the observations is

$$\begin{aligned}
\boldsymbol{\Sigma}\left\{\boldsymbol{\mathcal{L}}\right\} = \boldsymbol{\Sigma}\left\{\boldsymbol{\mathcal{E}}\right\} &= \sigma_0^2 \mathbf{Q}_{\boldsymbol{\mathcal{L}},\boldsymbol{\mathcal{L}}} = \sigma_0^2 \mathbf{Q}_{\boldsymbol{\mathcal{E}},\boldsymbol{\mathcal{E}}} && (2.3)\\
&= \sigma_0^2 \mathbf{P}^{-1}_{\boldsymbol{\mathcal{L}},\boldsymbol{\mathcal{L}}} = \sigma_0^2 \mathbf{P}^{-1}_{\boldsymbol{\mathcal{E}},\boldsymbol{\mathcal{E}}} && (2.4)\\
&= \boldsymbol{\Sigma}_{\boldsymbol{\mathcal{L}},\boldsymbol{\mathcal{L}}} := \boldsymbol{\Sigma}, && (2.5)
\end{aligned}$$

where $\mathbf{Q}$ are the cofactor and $\mathbf{P}$ weight matrices. σ_0^2 is the variance of unit weight. The expectation and the variance, as second central moment is used as the stochastic model in the adjustment.

With that, and given a realization of the measurements $\boldsymbol{l}$, the observation equations (OEQs) read

$$\boldsymbol{l} + \mathbf{v} = \mathbf{A}\mathbf{x} \tag{2.6}$$

where $\mathbf{v}$ are the residuals. Eq. (2.6) serves as the functional model in the adjustment. Furthermore, as $\boldsymbol{l}$ is some realization of $\boldsymbol{\mathcal{L}}$, the covariance matrix which enters the adjustment problem as stochastic model follows from (2.3) to (2.4), where the covariance matrix $\mathbf{\Sigma}$, or $\mathbf{P}$, $\mathbf{Q}$ and σ_0^2, might be unknown and need to be determined.

Assuming σ_0^2 and either $\mathbf{P}$ or $\mathbf{Q}$ are available, the least squares solution $\tilde{\mathbf{x}}$ for the unknown parameters results from the solution of the normal equations (NEQs), which follow from minimizing $\mathbf{v}^\top\mathbf{P}\mathbf{v} = \mathbf{v}^\top\mathbf{Q}^{-1}\mathbf{v} \hat{=} \mathbf{v}^\top\mathbf{\Sigma}^{-1}\mathbf{v}$ in the deterministic view or from the Best Linear Unbiased Estimator (BLUE) properties in the stochastic view (e.g. Meissl, 1982, Sect. A.6, B.4; Koch, 1999, Sect. 3)

$$\mathbf{A}^\top\mathbf{\Sigma}^{-1}\mathbf{A}\tilde{\mathbf{x}} = \mathbf{A}^\top\mathbf{\Sigma}^{-1}\mathbf{l} \tag{2.7}$$

$$\mathbf{A}^\top\left(\sigma_0^2\mathbf{Q}\right)^{-1}\mathbf{A}\tilde{\mathbf{x}} = \mathbf{A}^\top\left(\sigma_0^2\mathbf{Q}\right)^{-1}\mathbf{l} \tag{2.8}$$

$$\mathbf{A}^\top\mathbf{Q}^{-1}\mathbf{A}\tilde{\mathbf{x}} = \mathbf{A}^\top\mathbf{Q}^{-1}\mathbf{l} \tag{2.9}$$

$$\underbrace{\mathbf{A}^\top\mathbf{P}\mathbf{A}}_{:=\mathbf{N}}\tilde{\mathbf{x}} = \underbrace{\mathbf{A}^\top\mathbf{P}\mathbf{l}}_{:=\mathbf{n}} \tag{2.10}$$

$$\mathbf{N}\tilde{\mathbf{x}} = \mathbf{n}. \tag{2.11}$$

2.2 Stochastic Modeling Approaches and Decorrelation Strategies for Large Dimensional Observations

Most of the measurement errors of the observations analyzed in the applications are highly correlated due to the sensor design or the measurement principle. For instance, the gravity gradients as observed by GOCE (cf. Chap. 3) are highly correlated due to the drift of the accelerometers and the altimetric SSH errors contain correlations as the along-tack footprints overlap. This kind of measurement can be seen as an equidistant time series along the satellites orbit, as the instruments typically have a fixed sampling rate (or the user products are produced for a fixed sampling rate).

2.2.1 Representing the Stochastic Model

Methods and approaches from time-series analysis like one-dimensional covariance functions or stochastic processes are a good and flexible choice to model the correlated measurement errors (Schuh, 2016, **Schuh and Brockmann, 2018**). The basic idea is an iterative scheme to estimate a stochastic model from the residuals $\tilde{\mathbf{v}}^{(i)}$ (cf. (2.6)) which are computed with respect to the parameter estimates $\tilde{\mathbf{x}}^{(i)}$ of a previous iteration or with respect to some initial parameters.

The first approach which estimates/determines a covariance matrix $\mathbf{\Sigma}$ (or cofactor matrix $\mathbf{Q}$) is referred to as *covariance approach* in **Schuh and Brockmann, 2018**. To obtain redundancy for the estimation of a covariance model from a single realization of the residuals $\tilde{\mathbf{v}}^{(i)}$, stationarity has to be assumed. One option is to approximate empirically derived binned covariances by one-dimensional positive-definite covariance functions of a specific manually selected family (e.g. **Schubert et al., 2020**). Depending on the chosen family, different characteristics of the correlations are reflected by the analytic function, which is then used to setup the covariance matrix $\mathbf{\Sigma}$.

For instance **Becker et al., 2014b** use a linear combination of exponentials which results in a fully populated covariance matrix, or **Brockmann et al., 2016** a linear combination of exponentials and the cosine function, which is then made finite to obtain a sparse, i.e. banded covariance matrix. Alternatively, a more generic approach is proposed by **Schubert et al., 2020**, where the connection between AR or ARMA processes and the covariances is used to find a generic fitting procedure.

Within the filter approach (cf. **Schuh and Brockmann, 2018**) a so called pre-whitening filter is determined, which transforms observations $\mathbf{l}$ with $\mathbf{\Sigma}_{\mathcal{L},\mathcal{L}} = \mathbf{\Sigma}$ to observations $\bar{\mathbf{l}}$ with $\mathbf{\Sigma}_{\bar{\mathcal{L}},\bar{\mathcal{L}}} = \mathbf{I}$. Instead of covariances, the time series of residuals is approximated by an AR processes of order P.

Reorganizing the general process definition of an AR process

$$\mathcal{V}_t = \sum_{i=1}^{P} \alpha_i \mathcal{V}_{t-i} + \mathcal{E}_t \tag{2.12}$$

to the white noise component $\mathcal{E}_t \sim \mathcal{N}\left(0, \sigma^2\right)$, i.e.

$$\mathcal{E}_t = \mathcal{V}_t - \sum_{i=1}^{P} \alpha_i \mathcal{V}_{t-i} \tag{2.13}$$

can be written in matrix vector form for the entire (finite) time series of length N as

$$\begin{bmatrix} \mathcal{E}_1 \\ \mathcal{E}_2 \\ \mathcal{E}_3 \\ \vdots \\ \vdots \\ \vdots \\ \mathcal{E}_N \end{bmatrix} = \underbrace{\begin{bmatrix} 1 & & & & & & \\ -\alpha_1 & 1 & & & & & \\ -\alpha_2 & -\alpha_1 & 1 & & & & \\ \ddots & \ddots & \ddots & \ddots & & & \\ \ddots & \ddots & \ddots & \ddots & & & \\ \ddots & \ddots & \ddots & \ddots & \ddots & & \\ & -\alpha_P & \dots & -\alpha_2 & -\alpha_1 & 1 & \\ & \ddots & \ddots & \ddots & \ddots & \ddots & \\ & & -\alpha_P & \dots & -\alpha_2 & -\alpha_1 & 1 \end{bmatrix}}_{:=\mathbf{F}^\top} \begin{bmatrix} \mathcal{V}_1 \\ \mathcal{V}_2 \\ \mathcal{V}_3 \\ \vdots \\ \vdots \\ \vdots \\ \mathcal{V}_N \end{bmatrix} \tag{2.14}$$

$$\boldsymbol{\mathcal{E}} = \mathbf{F}^\top \boldsymbol{\mathcal{V}}. \tag{2.15}$$

This transformation results in $\boldsymbol{\mathcal{E}}$, which is white noise with variance σ^2 by definition. Consequently, the matrix $\mathbf{F}^\top$ transforms the vector $\boldsymbol{\mathcal{V}}$ which has the variance as represented by the AR process to white noise. Considering $-\boldsymbol{\mathcal{V}}$ as an estimate of the measurement errors, the AR process is a stochastic model for the measurement errors. The transformation from $\mathbf{l}$ to

$$\bar{\mathbf{l}} = \frac{1}{\sigma} \mathbf{F}^\top \mathbf{l} \tag{2.16}$$

is linear and results in decorrelated observations $\bar{\mathbf{l}}$ with $\boldsymbol{\Sigma}\left\{\bar{\boldsymbol{\mathcal{L}}}\right\} = \mathbf{I}$.

This filter approach, especially the estimation of the AR process coefficients is studied in detail to model the stochastic characteristics of the gravity gradients as observed by the GOCE mission in **Schubert et al., 2021b** and **Brockmann et al., 2021**. Due to its flexibility, AR processes are used as they are able to represent various signal characteristics just by adjusting the coefficients and its order. A strategy for a robust estimation of the AR process coefficients is developed based on several statistical tests of the residuals. The residuals v_i are iteratively approximated by an AR process of order P (cf. (2.12)), using

$$v_i + r_i = \sum_{j=1}^{P} \alpha_j v_{i-j} \tag{2.17}$$

as OEQ for the ith residual. α_j are the process coefficients and r_i is the ith entry of the residual vector $\mathbf{r}$ of the process fit.

The adjustment of the process coefficients α_j is performed iteratively in order to detect suspicious data, which do not fit to the process. Hypothesis tests for screening the process fit residual time-series $\mathbf{r}$ are used to reject any suspicious data from $\mathbf{v}$. An entire sequence of tests is available, see **Schubert et al., 2021b**. In moving windows, the data is tested for

- outliers/gross errors,
- changes in the mean value,

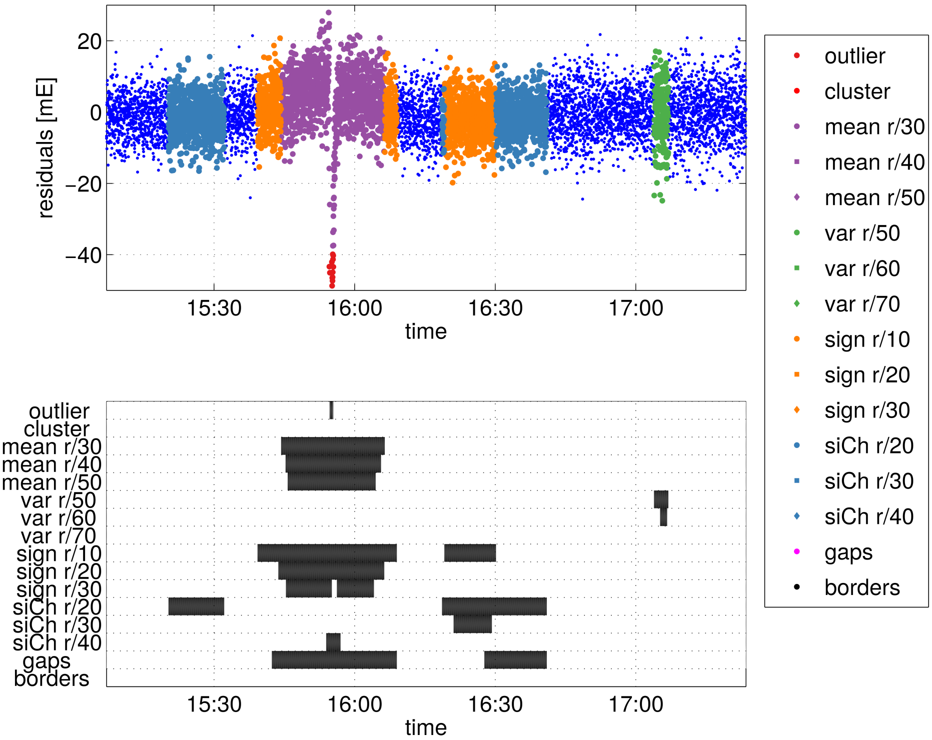

Figure 2.1: Visualization of an example output from the suspicious data detection tool. The plot shows a part of the GOCE gravity gradient time-series. The figure is taken from **Schubert et al., 2021b**.

- changes in the variance,
- distribution of signs, and
- the distribution of sign changes

applying tailored statistical tests. All central data points for which at least one of the enabled tests detects an anomaly, i.e. the alternative hypothesis is accepted, are rejected and not used in the iterative estimation of the AR process coefficients $\boldsymbol{\alpha}$ in next iteration. This is realized by an iteratively weighted least squares estimator (e.g. Kleiner et al., 1979). In addition, data points for which the null hypothesis is accepted but are located within a cluster of rejected data points are flagged as suspicious. An example plot for a small segment of the results is shown in Fig. 2.1. The detected suspicious data points are shown color coded, depending on the test which has been rejected. The example data set is a tiny part of the GOCE gravity gradient time series and is taken from **Schubert et al., 2021b**. More details about the applications for the GOCE example can be found in Chap. 3.

Following this strategy does not only provide a data adaptive estimate of the stochastic model represented by the AR process coefficients, it provides additionally a kind of outlier information/suspicious data detection, i.e. all data points are flagged, which neither agree with the functional model (2.6) nor fit to the stochastic model (2.3)–(2.5). This information is then optionally available for the parameter estimation task as a kind of outlier information when solving the overdetermined system of equations (2.6).

With the so-called *Yule-Walker equations* (e.g. Brockwell and Davis, 2016, Chap. 5) a close connection between the AR process coefficients $\boldsymbol{\alpha}$ and the covariances $\boldsymbol{\gamma}$ exists. This allows to compute the AR process coefficients from a given sequence of covariances $\boldsymbol{\gamma}$. Vice versa, given the set of AR process coefficients the covariances γ_l for a specific lag l can be computed using the *reorganized Yule-Walker equations* (**Schuh and Brockmann, 2018**). This discrete sequence of covariances can be used to directly setup a covariance matrix $\boldsymbol{\Sigma}$, or the sequence can be approximated by a

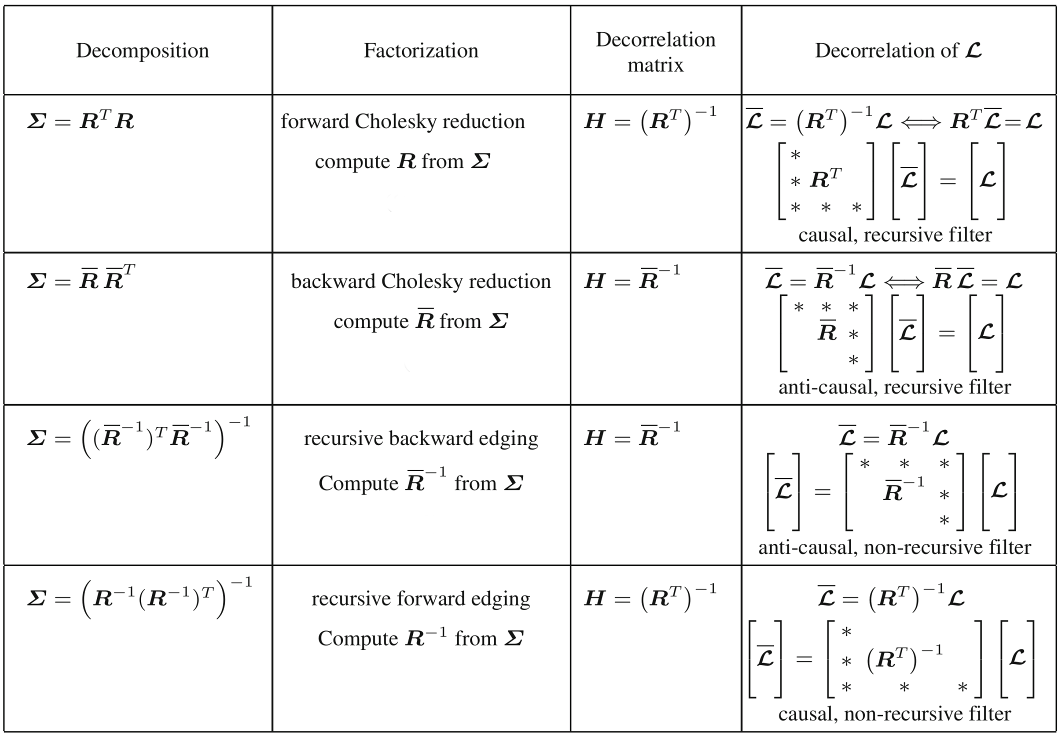

Decomposition	Factorization	Decorrelation matrix	Decorrelation of $\boldsymbol{\mathcal{L}}$
$\boldsymbol{\Sigma} = \boldsymbol{R}^T\boldsymbol{R}$	forward Cholesky reduction compute $\boldsymbol{R}$ from $\boldsymbol{\Sigma}$	$\boldsymbol{H} = (\boldsymbol{R}^T)^{-1}$	$\overline{\boldsymbol{\mathcal{L}}} = (\boldsymbol{R}^T)^{-1}\boldsymbol{\mathcal{L}} \iff \boldsymbol{R}^T\overline{\boldsymbol{\mathcal{L}}} = \boldsymbol{\mathcal{L}}$ $\begin{bmatrix} * & & \\ * & \boldsymbol{R}^T & \\ * & * & * \end{bmatrix} \begin{bmatrix} \\ \overline{\boldsymbol{\mathcal{L}}} \\ \\ \end{bmatrix} = \begin{bmatrix} \\ \boldsymbol{\mathcal{L}} \\ \\ \end{bmatrix}$ causal, recursive filter
$\boldsymbol{\Sigma} = \overline{\boldsymbol{R}}\,\overline{\boldsymbol{R}}^T$	backward Cholesky reduction compute $\overline{\boldsymbol{R}}$ from $\boldsymbol{\Sigma}$	$\boldsymbol{H} = \overline{\boldsymbol{R}}^{-1}$	$\overline{\boldsymbol{\mathcal{L}}} = \overline{\boldsymbol{R}}^{-1}\boldsymbol{\mathcal{L}} \iff \overline{\boldsymbol{R}}\,\overline{\boldsymbol{\mathcal{L}}} = \boldsymbol{\mathcal{L}}$ $\begin{bmatrix} * & * & * \\ & \overline{\boldsymbol{R}} & * \\ & & * \end{bmatrix} \begin{bmatrix} \\ \overline{\boldsymbol{\mathcal{L}}} \\ \\ \end{bmatrix} = \begin{bmatrix} \\ \boldsymbol{\mathcal{L}} \\ \\ \end{bmatrix}$ anti-causal, recursive filter
$\boldsymbol{\Sigma} = \left((\overline{\boldsymbol{R}}^{-1})^T\overline{\boldsymbol{R}}^{-1}\right)^{-1}$	recursive backward edging Compute $\overline{\boldsymbol{R}}^{-1}$ from $\boldsymbol{\Sigma}$	$\boldsymbol{H} = \overline{\boldsymbol{R}}^{-1}$	$\overline{\boldsymbol{\mathcal{L}}} = \overline{\boldsymbol{R}}^{-1}\boldsymbol{\mathcal{L}}$ $\begin{bmatrix} \\ \overline{\boldsymbol{\mathcal{L}}} \\ \\ \end{bmatrix} = \begin{bmatrix} * & * & * \\ & \overline{\boldsymbol{R}}^{-1} & * \\ & & * \end{bmatrix} \begin{bmatrix} \\ \boldsymbol{\mathcal{L}} \\ \\ \end{bmatrix}$ anti-causal, non-recursive filter
$\boldsymbol{\Sigma} = \left(\boldsymbol{R}^{-1}(\boldsymbol{R}^{-1})^T\right)^{-1}$	recursive forward edging Compute $\boldsymbol{R}^{-1}$ from $\boldsymbol{\Sigma}$	$\boldsymbol{H} = (\boldsymbol{R}^T)^{-1}$	$\overline{\boldsymbol{\mathcal{L}}} = (\boldsymbol{R}^T)^{-1}\boldsymbol{\mathcal{L}}$ $\begin{bmatrix} \\ \overline{\boldsymbol{\mathcal{L}}} \\ \\ \end{bmatrix} = \begin{bmatrix} * & & \\ * & (\boldsymbol{R}^T)^{-1} & \\ * & * & * \end{bmatrix} \begin{bmatrix} \\ \boldsymbol{\mathcal{L}} \\ \\ \end{bmatrix}$ causal, non-recursive filter

Figure 2.2: Decorrelation strategies depending on the different factorizations of the covariance matrix $\mathbf{\Sigma}$ and the corresponding filter type. The figure is taken from **Schuh and Brockmann, 2018**.

continuous analytic covariance function, in case it is required to interpolate between the discrete covariances, i.e. evaluation between the equidistant lags is required (**Korte et al., 2021**).

The estimation strategy using the robustified estimation of AR process coefficients is applied for GOCE gravity gradients (see Chap. 3 for details, **Schubert et al., 2021b; Brockmann et al., 2021**) and for the SSH measurements in the context of MDT estimation (see Chap. 4 for details, **Brockmann et al., 2016; Brockmann and Schuh, 2016b**). A similar strategy is applied in **Jendges and Brockmann, in review** to model the covariance of the signal and the noise in GRACE and model derived Total Water Storage (TWS) time series. These covariance models are applied in the context of the project STAMPED[1] to improve the linear TWS trend estimates and their covariances, which are required for significance tests to detect drying or wetting regions.

2.2.2 Decorrelation Strategies

With the discussions and relations introduced in Sect. 2.2.1, for both the covariance approach and the filter approach, the stochastic model has to be accounted for in the computation of the NEQs (cf. (2.7) – (2.11)). In **Schuh and Brockmann, 2018** the computationally most efficient way is discussed in detail. Both approaches are presented in the framework of decorrelation (e.g. Koch, 1999, Sect. 3.2) and are linked to different variants of the Cholesky decomposition of the covariance matrix $\mathbf{\Sigma}$ (or cofactor matrix $\mathbf{Q}$), see Fig. 2.2 as an overview and **Schuh and Brockmann, 2018** for more details.

---

[1] Statistical Testing and stochastic processes for the Analysis of Modeled and observed Earth system Data (STAMPED). PI J. M. Brockmann. Funded by Transdisciplinary Research Area 1: Mathematics, Modelling and Simulation of Complex Systems (TRA1 Modelling), University of Bonn as part of the Excellence Strategy of the federal and state governments and supported by CRC 1502 DETECT: Regional Climate Change: Disentangling the Role of Land Use and Water Management (DETECT) which is funded by Deutsche Forschungsgemeinschaft/German Research Foundation (DFG) SFB 1502/1–2022 project number: 450058266 (2023-2024).

The basic idea of decorrelation is to decompose the weight matrix with the standard version of the Cholesky decomposition, i.e.

$$\mathbf{P} = \mathbf{G}^\top\mathbf{G}, \tag{2.18}$$

with the upper triangular matrix $\mathbf{G}$. Inserting this into (2.10) yields

$$\begin{aligned}
\mathbf{A}^\top\mathbf{G}^\top \underbrace{\mathbf{G}\mathbf{A}}_{:=\bar{\mathbf{A}}}\tilde{\mathbf{x}} &= \mathbf{A}^\top\mathbf{G}^\top \underbrace{\mathbf{G}\mathbf{l}}_{:=\bar{\mathbf{l}}} && (2.19)\\
\bar{\mathbf{A}}^\top\bar{\mathbf{A}}\tilde{\mathbf{x}} &= \bar{\mathbf{A}}^\top\bar{\mathbf{l}} && (2.20)\\
\mathbf{N}\tilde{\mathbf{x}} &= \mathbf{n}. && (2.21)
\end{aligned}$$

It can be easily shown that $\mathbf{\Sigma}\left\{\bar{\mathcal{L}}\right\} = \sigma_0^2\mathbf{I}$ by applying linear variance propagation to the linear transformation $\bar{\mathbf{l}} = \mathbf{G}\mathbf{l}$. As $\mathbf{G}$ is multiplied and is an upper triangular matrix, the corresponding filter is an anti-causal non-recursive filter (i.e. the third row in Fig. 2.2). Performing this kind of decorrelation requires the Cholesky decomposition of the weight matrix (in-place operation) and is applied by an in-place multiplication with a triangular matrix multiplication (in terms of the Basic Linear Algebra Subprograms (BLAS) it is a call to `trmm`). The computation of $\mathbf{N}$ remains a symmetric rank update (`syrk` in terms of BLAS).

Similarly, in case the cofactor matrix (or covariance matrix) is available the standard version of the Cholesky decomposition can be applied, i.e. the decorrelation is then

$$\mathbf{Q} = \mathbf{R}^\top\mathbf{R}. \tag{2.22}$$

Again, inserting the decomposition into (2.9) yields

$$\begin{aligned}
\mathbf{A}^\top\left(\mathbf{R}^\top\mathbf{R}\right)^{-1}\mathbf{A}\tilde{\mathbf{x}} &= \mathbf{A}^\top\left(\mathbf{R}^\top\mathbf{R}\right)^{-1}\mathbf{l} && (2.23)\\
\mathbf{A}^\top\mathbf{R}^{-1}\underbrace{\mathbf{R}^{-\top}\mathbf{A}}_{:=\hat{\mathbf{A}}}\tilde{\mathbf{x}} &= \mathbf{A}^\top\mathbf{R}^{-1}\underbrace{\mathbf{R}^{-\top}\mathbf{l}}_{:=\hat{\mathbf{l}}} && (2.24)\\
\hat{\mathbf{A}}^\top\hat{\mathbf{A}}\tilde{\mathbf{x}} &= \hat{\mathbf{A}}^\top\hat{\mathbf{l}} && (2.25)\\
\mathbf{N}\tilde{\mathbf{x}} &= \mathbf{n}. && (2.26)
\end{aligned}$$

Here, the decorrelation results from the solution of

$$\mathbf{R}^\top\hat{\mathbf{l}} = \mathbf{l} \tag{2.27}$$

for the observation vector (and analogously for the design matrix). Again, the in-place Cholesky decomposition, but now of the covariance matrix, is required. The decorrelation is then performed by an in-place forward substitution as $\mathbf{R}^\top$ is lower triangular (`trsm` using the BLAS convention). As above, the computation of $\mathbf{N}$ remains a symmetric rank update (`syrk` in terms of BLAS). Thus, the corresponding filter is causal and recursive (i.e. the first row in Fig. 2.2). Special properties of $\mathbf{\Sigma}$, e.g. in case of a finite covariance matrix, can be easily accounted for by using a band representation of $\mathbf{\Sigma}$ and $\mathbf{R}$. Compared to the first version, this has the advantage, that the weight matrix is not required, the inversion of the covariance matrix can be avoided.

When considering the filter approach, the decorrelation of the design matrix (or of the observations) with a causal non-recursive filter can be written as a matrix vector product $\bar{\mathbf{l}} = \mathbf{F}^\top\mathbf{l}$ (cf. (2.16)). $\mathbf{F}^\top$ is a lower triangular band matrix of order P with unit diagonal and the negative AR process coefficients on the super diagonals (see (2.14)). Computing the NEQs – the weight matrix can be neglected after pre-whitening – with this transformation yields

$$\begin{aligned}
\left(\mathbf{F}^\top\mathbf{A}\right)^\top\left(\mathbf{F}^\top\mathbf{A}\right)\tilde{\mathbf{x}} &= \left(\mathbf{F}^\top\mathbf{A}\right)^\top\left(\mathbf{F}^\top\mathbf{l}\right) && (2.28)\\
\mathbf{A}^\top\mathbf{F}\mathbf{F}^\top\mathbf{A} &= \mathbf{A}^\top\mathbf{F}\mathbf{F}^\top\mathbf{l}. && (2.29)
\end{aligned}$$

Comparing (2.29) with (2.19) shows that while $\mathbf{P} = \mathbf{G}^\top\mathbf{G}$ is the forward Cholesky decomposition of $\mathbf{P}$, $\mathbf{F}\mathbf{F}^\top$ is the backward Cholesky decomposition of $\mathbf{P}$ (or the recursive forward edging of $\boldsymbol{\Sigma}$). The advantage of this procedure is that given the AR process coefficients the matrix $\mathbf{F}$ can be directly setup and the decorrelation is efficiently applied by a product of a lower triangular band matrix with a general matrix. This corresponds to the fourth row in Fig. 2.2.

Comparing the filter and the covariance approach, both show their pros and cons. The covariance approach is very well suited in case a covariance function is chosen to describe the stochastic model. The covariance matrix can be set up for any vector of observations and data gaps can be easily accounted for. In case of a finite covariance function, the sparsity is maintained in the decorrelation. As it corresponds to a causal filter, there are no issues at the start of the observation vector as only future values are required.

In case the stochastic processes are used to describe the characteristics, the filter approach is best suited, as the banded triangular filter matrix follows directly from the process. But, its application is restricted to equidistant observations, i.e. explicit data gaps require a special handling. Due to the structure when using AR processes, values from the past are required for decorrelation, which do not exist for the first data points of the time-series. The representation as in (2.14) implicitly assumes them as zero – which results in the first P data points being improperly decorrelated (warmup phase of the filter). In practical applications they are not usable and have to be discarded. This warmup phase occurs for each data gap, which results in a large number of discarded observations in case of frequent data gaps.

To combine the strengths of both – the numerical efficiency of the filter approach and the flexibility of the covariance approach – the relations between the approaches as discussed above are used together with the Yule-Walker equations to derive a filter matrix which accounts for the warmup phase and data-gaps (for details see **Schuh and Brockmann, 2018**, Sect. 6). The filter matrix is derived from the covariance approach and the backward Cholesky decomposition by recursive forward edging. Basically, all data points affected by the warmup and data-gaps can be computed from the covariance approach. Still the filter matrix is a lower triangular matrix, but the bandwidth is increased depending on the length of the data gap and the process order (see Fig. 2.3).

2.2.3 Treatment of Stationarity

To estimate a stochastic model from a single realization of the residuals $\mathbf{v}$, redundancy is required. A typical procedure is to assume covariance stationarity of the time series or the generating process (e.g. Schuh, 2016; Hayes, 1996, Sect. 3.3), i.e. the independence of the covariance of (absolute) time. In case the assumption is violated, e.g. after a change on the measurement platform or changing characteristics are detected, a segmentation into multiple time series can be applied. These are then assumed to be independent and individual processes are estimated. This strategy is applied in **Schubert et al., 2021b; Brockmann et al., 2021** and **Brockmann and Schuh, 2016b**.

To avoid the manual segmentation, alternatives using time-variable stochastic processes are theoretically studied in **Korte et al., 2023b** and **Korte et al., 2023a**. In these studies, AR processes are parameterized via the roots of their characteristic polynomials and a linear motion model for the roots is assumed, which introduces the time-dependence to the process. Approaches to estimate the AR process of time varying coefficients (TVAR) are derived (see **Korte et al., 2023b**) and studied for different process orders (**Korte et al., 2023a**).

2.3 FES for Spatio-Temporal Approximation Tasks

In case there exists no closed mathematical model function – e.g. derived from physical laws – to represent the reference surface of interest (cf. Sect. 1.1), the model function is an additional unknown quantity. In those cases, either stochastic approaches (e.g. Moritz, 1974, Sect. 2; Wackernagel, 2010;

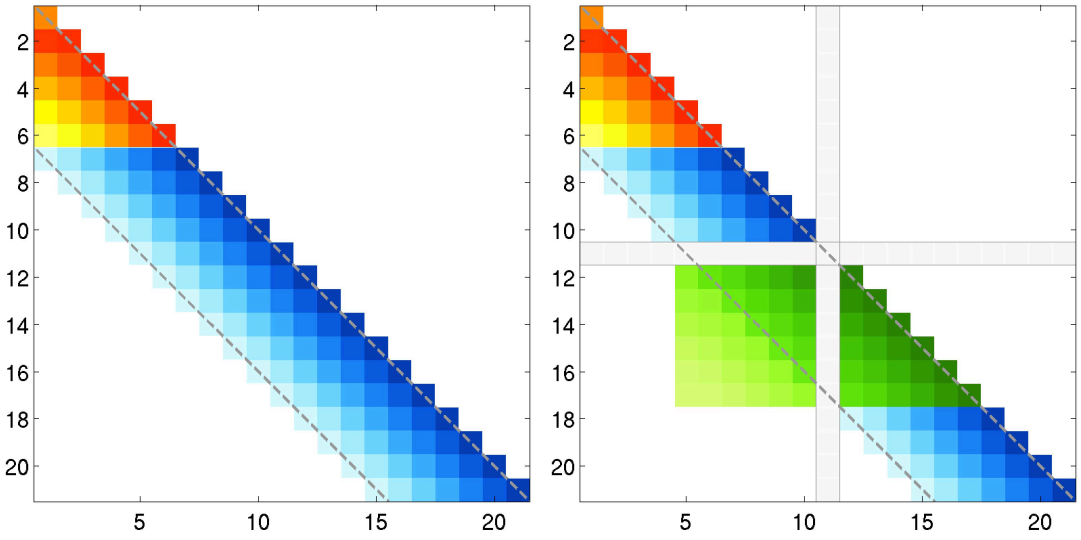

(a) Finite sequence with 21 equi-spaced data points.

(b) Finite sequence with 21 equi-spaced data points and missing data at position 11.

Figure 2.3: Example structure of the filter matrix for an AR(6) process deduced by the backward Cholesky approach. Blue elements directly follow from the process coefficients, red elements are modified due to the warmup and green elements are modified/occur due to data gaps. Grey lines indicate the original band matrix structure.

Schuh, 2016 or **Schuh et al., 2023**) relying on the estimated stochastic signal characteristics can be used, or deterministic approaches, which approximate the unknown function space as well. In general just considering the two-dimensional case required for geo spatial modeling of reference surfaces, the surface is approximated by a linear combination of I basis functions, given by

$$\bar{f}(x,y) \approx f(x,y) = \sum_{i=1}^{I} a_i b_i(x,y) \quad f : \mathbb{R}^2 \rightarrow \mathbb{R}. \tag{2.30}$$

The characteristics of the basis functions $b_i(x,y)$ determine the characteristics of the function $f(x,y)$ defined in the entire domain of interest Ω.

Due to their flexibility in representing various characteristics and their numerical properties, basis functions with local support are a good choice for approximating surfaces with complicated and irregular shape (e.g. Fahrmeir et al., 2021, Chap. 8). Possible candidates are Splines, Wavelets or FEs (Fahrmeir et al., 2021; Keller, 2008; Ahlberg et al., 1967; Ciarlet, 1978a), which are not common in the context of MDT and MSS modeling but often used in other surface-like approximation tasks (e.g. Keller and Borkowski, 2019; Lieb et al., 2016; Durmaz and Karslioglu, 2015; Dettmering et al., 2011; Harmening and Neuner, 2020; Schuh, 1984; Becker et al., 2012).

2.3.1 FEs for Spatial Approximation Tasks

In this contribution, the focus is on FEs (**Becker et al., 2014b; Borlinghaus et al., 2022a; Borlinghaus et al., 2023a; Neyers and Brockmann, 2024**) as they are rarely used for reference surface approximation tasks. In contrast to the FEM, where FE are used to solve discretized differential equations numerically (e.g. Hahn, 1975; Ciarlet, 1978b), the basis functions of the underlying FES are used to approximate the unknown function space of $\bar{f}(x,y)$, which is then used to approximate the surface. For the approximation task, existing FE from the FEM are selected and utilized.

For constructing these so called FES, the entire domain of interest Ω is partitioned into a finite number of sub-regions, thus generating a mesh. Each region has its own locally defined basis functions and the corresponding degrees of freedom (DOF), these are finally the parameters in the approximation task. A single FE is defined by the shape, the local DOF and the local function space spanned by the basis functions of such a sub-region (Ciarlet, 1978b). By an appropriate choice of local basis functions based on literature, a piece-wise global function space is composed with at least C^0-smoothness, aggregating the local parameters to a global parameter set. Higher orders of continuity are possible and depend on the employed FEs.

Given the definition of a FES (i.e. the mesh, the DOF and the FE), the global function can then be written as in (2.30), or specifically introducing the notation used for the FE based approximation (see **Borlinghaus et al., 2023b; Borlinghaus et al., 2022a**) as

$$g_s(x,y) = \sum_{i \in I_s} a_{s,i} b_{s,i}(x,y) \quad g_s : \mathbb{R}^2 \to \mathbb{R} \tag{2.31}$$

to construct the function g_s which is supposed to model the signal s. Here, $i \in I_s$ describes the global indexing of all aggregated I_s piece-wise defined basis functions $b_{s,i} : \mathbb{R}^2 \to \mathbb{R}$ collected in the set $\mathrm{S}_s := \{b_{s,i}\}$, and $a_{s,i} \in \mathbb{R}$ the corresponding scaling coefficients/parameters.

2.3.2 Construction and Refinement of Meshes

As discussed above, the definition of the FES requires that the domain of interest is partitioned into a mesh. For the chosen two dimensional (planar) approximation tasks, either a partitioning of the domain Ω into triangles – i.e. a triangulation, or a partitioning into rectangles is required. This depends on the selected FE. As the geometry of Ω often becomes complex, e.g. the ocean bounded by coastlines in the applications from Chap. 4 and 5, a triangulation is well suited for the approximation of the domain. Consequently the focus here and in the application in Chapters 4 and 5 is on FE defined on triangles.

As soon as a specific FE is selected, the mesh/triangulation defines the spatial resolution of the FES. Several characteristics exist, which, depending on the application, can be used to construct and optimize the mesh, i.e. in this case the triangulation of Ω:

(i) A specific homogeneous target resolution.
(ii) The distribution of the observations.
(iii) Prior knowledge or other measures of the spatial signal variability.

For the triangulations the software package JIGSAW(GEO) (Engwirda, 2017; Engwirda, 2019) is used, which can optimize generalized Delaunay/Voronoi triangulations based on flexible user input. As an example, Fig. 2.4 shows generated triangulations for the North Atlantic ocean. These meshes are generated by JIGSAW(GEO) from a bounding polygon of the region of interest (including the coastlines) and the definition of a homogeneous target edge length in the entire domain of interest, thus it corresponds to mesh optimization strategy (i).

In general, within the approximation tasks the meshes are static, i.e. they are created once in the beginning, focusing on one of the characteristics (i) to (iii). Together with the selected FE, the mesh defines the spatial resolution. Although the mesh is kept static for the approximation, the mesh can be iteratively refined, i.e. the approximation can be repeated with an updated or refined mesh.

A specific strategy is studied in detail in **Borlinghaus et al., 2023b**, where the proposed strategy is to use the least squares residuals of the approximation to detect sub-regions in Ω which show an anomalous behavior in statistical measures derived from the residuals. E.g., standard deviation and mean values are empirically derived from all residuals in a triangle. Using for instance the standard deviation (cf. **Borlinghaus et al., 2023b**) a large value is an indicator for a mesh refinement (i.e. under-parameterization), whereas a specifically low value is an indicator for a too fine mesh (i.e. over-parameterization).

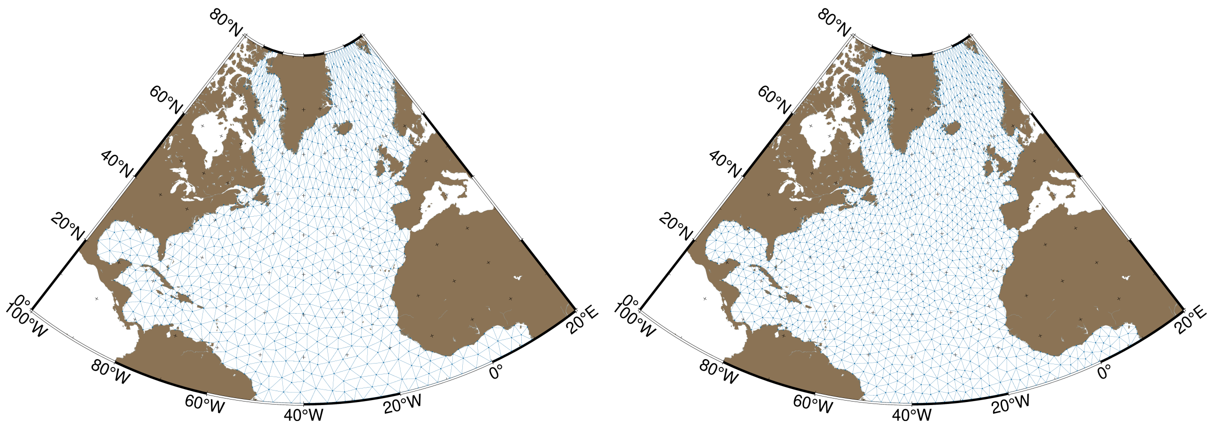

(a) Target edge length 320 km.

(b) Target edge length 255 km.

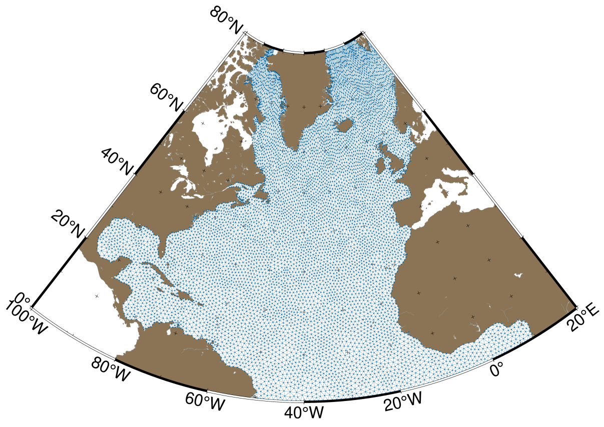

(c) Target edge length 100 km.

mesh	# nodes	# edges
(a) 320 km	937	1562
(b) 255 km	1437	2450
(c) 100 km	8084	15 108

(d) Statistics about the meshes.

Figure 2.4: Example meshes generated with JIGSAW(GEO) for the North Atlantic Ocean from a given boundary polygon and different but homogeneous target edge lengths of the individual triangles.

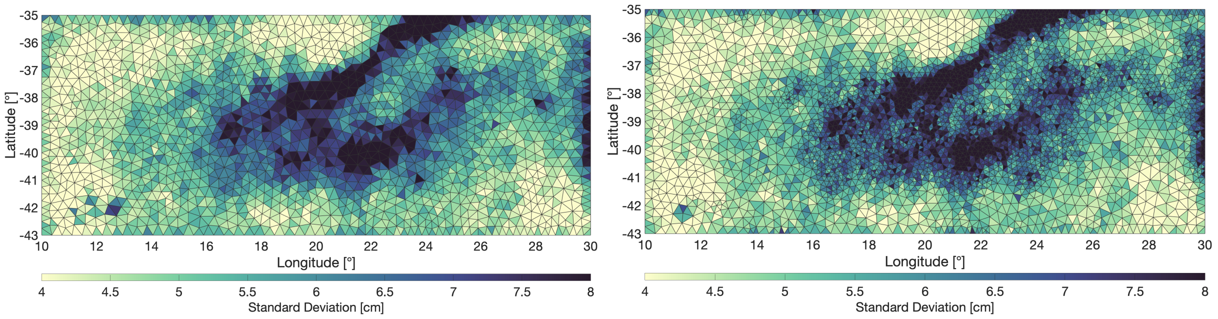

(a) For the homogeneous mesh.

(b) For the refined mesh.

Figure 2.5: Visualization of the spatial distribution of the standard deviations computed empirically from all approximation residuals inside each triangle for the initial and refined mesh. Figure taken from **Borlinghaus et al., 2023b**.

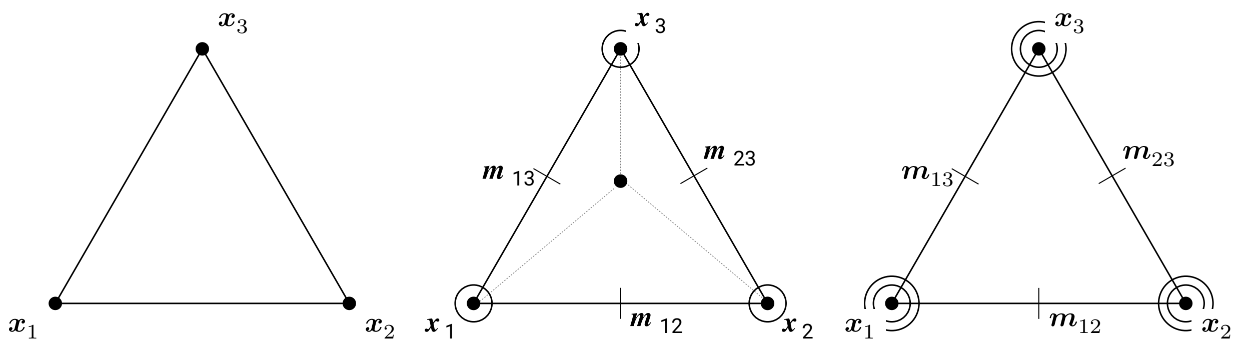

(a) For the Linear element. (b) For the HCT element. (c) For the Argyris element.

Figure 2.6: Classical representation of the used triangular FEs. Figure is taken from **Neyers et al., 2019**.

Fig. 2.5 shows an example from a spatial approximation taken from **Borlinghaus et al., 2023b**. Fig. 2.5a shows the spatial plot of standard deviation per triangle computed from the residuals which result from the approximation with an initial homogeneous mesh derived by JIGSAW(GEO). This map is transformed to an input to JIGSAW(GEO), requesting a smaller target edge length in regions of higher standard deviations, and larger (or same) target edge lengths for the other regions. Fig. 2.5b shows the resulting refined mesh. Again, the triangles are color-coded with the empirical standard deviations, but now computed from the approximation residuals with the refined mesh. It is shown and discussed in detail in **Borlinghaus et al., 2023b**, that the refinement mesh includes both – regions with successful refinement and regions which are over-parameterized. It is concluded that external validations are required, as the least squares residuals become smaller by definition.

2.3.3 Overview of Studied FEs

As discussed above, the focus here – as well as in the applications in Chap. 4 and 5 – is on two-dimensional FEs defined on a triangle, three of them with different characteristics are used.

The first one is the simplest element, it is the Linear element, which establishes C^0-smoothness (e.g. Ciarlet, 1978b). It is defined by a polynomial of degree one i.e. a plane, the conditions for C^0-smoothness of the global functions can be easily obtained by a parameterization via the function values in the nodal points (cf. Fig. 2.6a). Thus, the element has three DOF, and the parameters are easily interpretable as function values in the nodes.

When increasing the smoothness requirement to C^1 while still sticking to polynomial local basis functions, this results in the Argyris element (Argyris et al., 1968). Using degree five polynomials, i.e. 21 DOF the global C^1-smoothness can be obtained using a parameterization via the function values, the two first derivatives in x and y direction, the second derivatives in x, y and in mixed direction in the three nodal points and finally the normal derivatives in the midpoints of the three edges (see Fig. 2.6c and Argyris et al., 1968; Foster, 2013; Foster et al., 2014; Domínguez and Sayas, 2008; Neyers, 2017).

The high degree of the polynomial used for the Argyris element, and thus the DOFs can be reduced using the so called composite elements (see e.g., Ciarlet, 1978a, Chap. 6.1). Basic idea of the composite elements is – it can be seen as a kind of recursion – a decomposition of a triangle into sub-regions, for which lower degree polynomials are composed to local basis functions establishing the smoothness requirements at the borders. The third element considered here is the Hsieh–Clough–Tocher (HCT) element (cf. Clough and Toche, 1966), which is a composed element. As indicated in Fig. 2.6b, the triangle is decomposed into three sub-triangles, in each of which polynomials of degree three are defined. These are combined with C^1-smoothness conditions at the borders, resulting in the definition of the local basis functions. Consequently, these do not span the entire space of the polynomials of degree three but are restricted. The composed HCT basis functions

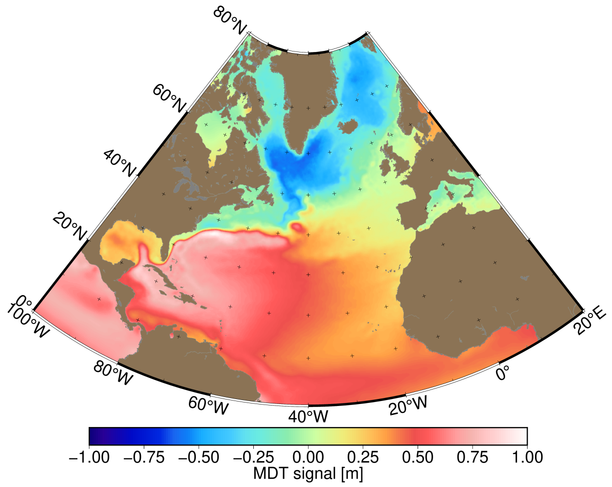

Figure 2.7: Gridded MDT model MDT_CNES_CLS18 used for the approximation with the different FEs in the domain of interest (DOI) which is the North Atlantic.

Table 2.1: Number of parameters for surface approximation with the three considered FEs using the three meshes as shown in Fig. 2.5.

	FES		
mesh	linear	HCT	Argyris
320 km	920	5248	**8008**
255 km	1414	**8116**	12 358
100 km	**8084**	47 459	71 711

have 12 DOF and are parameterized via the function values, the two first derivatives in x and y direction in the three nodal points and the normal derivatives in the midpoints of the three edges (see Fig. 2.6b). Similar to the Argyris element, C^1-smoothness is obtained with the HCT element but with significantly lower number of parameters.

To demonstrate the characteristics of the different FEs, one of the reference surfaces of interest is approximated using the three elements on the three triangulations shown in Fig. 2.4 (similar to the study from **Neyers et al., 2019**). The regularly gridded values of the highly oversampled and smooth MDT_CNES_CLS18 model are used to approximate the MDT signal with the different FESs. Using the original 1/8° sampling, about 320 000 observations are used to approximate the MDT in the North Atlantic (cf. Fig. 2.7). As the different meshes do not exactly cover the same DOI the number of data points used as observations slightly differs depending on the mesh. Tab. 2.1 shows the total number of parameters for the estimation in the DOI, which justifies the — at first glance strange — selected meshes with 100 km, 255 km and 320 km target edge length: Whereas the 100 km mesh results in about 8000 parameters for the linear element, the 255 km mesh results in roughly the same number of parameters for the HCT element and finally the same holds true for the 320 km mesh and the Argyris element.

Figure 2.8 shows the least squares residuals of the approximations with all three elements on three meshes for a sub-region including the strong signal of the Gulf stream, computed with Massive Parallel FRAmework for the Adjustment of Geodetic MEasureMENTs (mpFRAGMENT). The statistics for the minimum, maximum as well as the Root Mean Square error (RMS) are summarized in Table 2.2 for the entire DOI and the region shown. The anti-diagonal plots, i.e. 2.8g, 2.8e and 2.8c refer to roughly the same number of unknown parameters.

Table 2.2: Statistics of the least squares residuals of the nine different approximations of the MDT_CNES_CLS18 with the different FESs. Again the anti-diagonal elements for the global and regional statistics are comparable with respect to the number of parameters estimated and are thus highlighted in bold.

(a) For the entire DOI.

mesh	linear			HCT			Argyris		
mesh	min [cm]	max [cm]	RMS [cm]	min [cm]	max [cm]	RMS [cm]	min [cm]	max [cm]	RMS [cm]
320 km	-38.2	35.6	3.3	-19.7	20.6	1.3	**-14.8**	**12.3**	**0.7**
255 km	-39.5	35.2	2.7	**-15.7**	**14.6**	**0.8**	-6.3	6.4	0.4
100 km	**-13.0**	**15.3**	**0.7**	-5.1	5.0	0.2	-3.6	4.0	0.1

(b) For the sub-region, cf. Fig. 2.8.

mesh	linear			HCT			Argyris		
mesh	min [cm]	max [cm]	RMS [cm]	min [cm]	max [cm]	RMS [cm]	min [cm]	max [cm]	RMS [cm]
320 km	-38.2	35.6	6.7	-19.7	20.6	2.6	**-14.8**	**12.3**	**1.2**
255 km	-39.5	35.2	5.5	**-15.7**	**14.6**	**1.5**	-6.3	6.4	0.6
100 km	**-13.0**	**15.3**	**1.3**	-3.8	4.5	0.3	-3.5	3.0	0.2

It is challenging to provide a measure for the average spatial resolution of the FEs, as it strongly depends on the local structure of the meshes. The number of parameters per area is a good indicator. From Table 2.1 it is concluded that the three 'anti-diagonal' models with about 8000 parameters have a spatial resolution of about 100 km, which follows in the easiest way from the linear element.

Despite the obvious conclusion that the higher the number of parameters – either due to a finer mesh, or the larger DOF of the FE, or both – the anti-diagonals of 2.2 and Fig. 2.8 provide a justification for a focus on the linear and the Argyris elements in the applications from Chap. 4 and 5. It is shown, and confirmed by similar (unpublished) studies not explicitly shown here, that even in case of the same amount of parameters the Argyris element performs best. Compared to the HCT element on the 255 km mesh, RMS as well as extreme values are smaller for the coarser 320 km mesh when using the Argyris element while slightly less parameters are estimated. Furthermore less systematic oscillations are visible, which can occur for the HCT element around the sub-triangles especially in case of (correlated) noise in the data (not explicitly shown here). Although the linear element does not provide C^1-smoothness, its performance on the 100 km mesh is only slightly worse compared to the Argyris element. As it has the advantage of the simplicity, it is considered in the applications as well (e.g. **Becker et al., 2014b; Becker et al., 2014a**) in case C^1-smoothness is not required/desired.

2.3.4 Extensions Towards a Spatio-Temporal FES

For the spatio-temporal modeling, the flexible strategy based on FEs is extended to the temporal domain (**Borlinghaus et al., 2022a; Borlinghaus et al., 2023a; Brockmann et al., 2023**). For that purpose, the spatio-temporal function is composed from separable functions, i.e the spatial FES is combined with a one-dimensional function in the temporal domain.

Just considering the temporal signal s in a first step, the one-dimensional function can be represented as a linear combination of J_s basis functions $d_{s,j}(t)$ in the time-domain, similar to

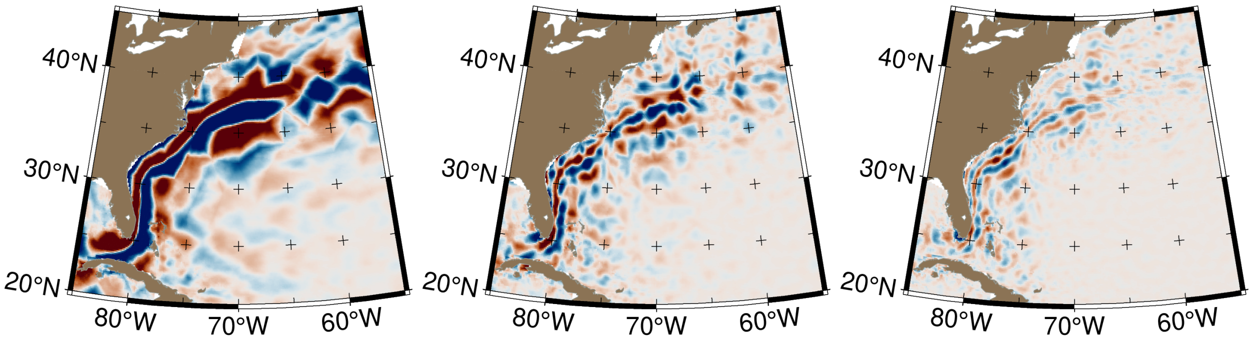

(a) Linear element, 320 km mesh. (b) HCT element, 320 km mesh. (c) Argyris element, 320 km mesh.

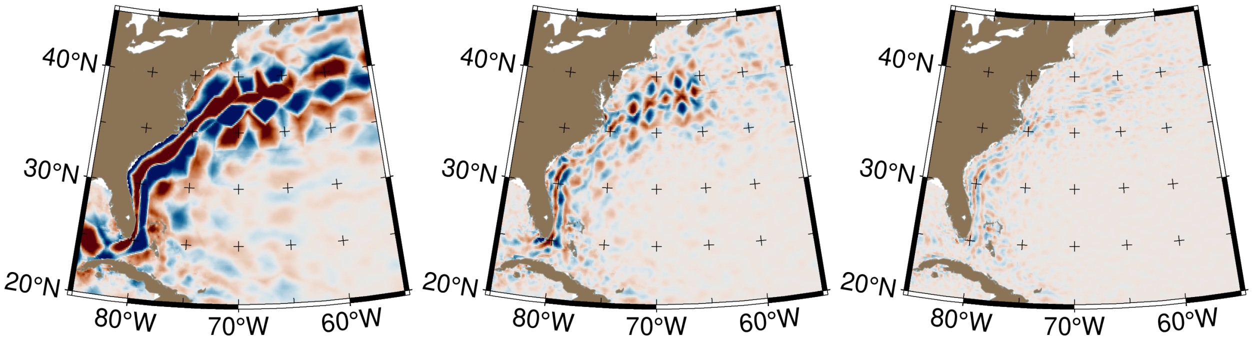

(d) Linear element, 255 km mesh. (e) HCT element, 255 km mesh. (f) Argyris element, 255 km mesh.

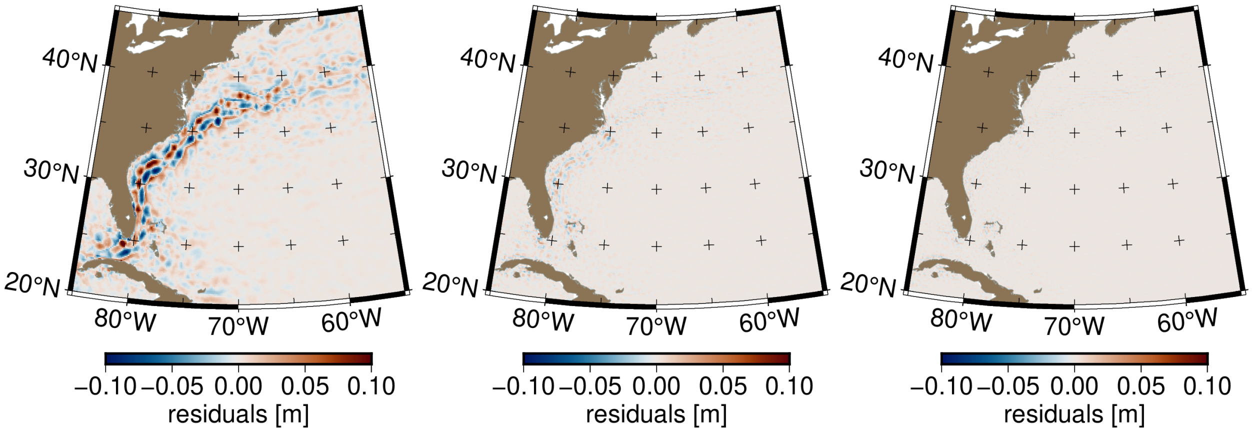

(g) Linear element, 100 km mesh. (h) HCT element, 100 km mesh. (i) Argyris element, 100 km mesh.

Figure 2.8: Zoom to the least squares residuals for the different approximations of the MDT_CNES_CLS18 for the different FEs and meshes. First column shows the results for the linear element, the second for the HCT and the third for the Argyris element. The first row solutions use the 320 km mesh, the second the 255 km and the third the 100 km mesh. Consequently the anti-diagonal plots are for the results with a comparable amount of unknown parameters.

(2.31), i.e.

$$h_s(t) = \sum_{j \in J_s} c_{s,j} d_{s,j}(t) \quad h_s : \mathbb{R} \to \mathbb{R}. \tag{2.32}$$

Depending on the choice of the set of basis functions $\mathrm{T}_s := \left\{d_{s,j}\right\}$, the function space can be very flexible. A typical choice can be basis functions with global support, indicated by superscript ^{g}, e.g.

$$\mathrm{T}_s^g := \{1,\, t,\, \cos(\omega_1 t),\, \sin(\omega_1 t)\} \tag{2.33}$$

which allow the modeling of long-term signals like mean, trend and for instance annual oscillations with just a few DOF (e.g. Agha Karimi et al., 2020; **Borlinghaus et al., 2023b**, **Brockmann et al., 2023**).

As this kind of function is rigid, alternatively basis functions with local support can be used for the temporal function, similar to the choice of FEs for the spatial domain. Typical choices can be one-dimensional piecewise polynomials, i.e. one-dimensional FE, or spline function spaces, like B-Splines (e.g. De Boor, 2001; Fahrmeir et al., 2021; **Borlinghaus et al., 2023b**). By design, a large number of DOFs are required for a flexible function space. Uniform B-Splines with constant node spacing $\Delta\kappa$ in the entire domain have the advantage of well-known low-pass filter characteristics which only depend on $\Delta\kappa$ and their order (cf. Sünkel, 1985; Köhler et al., 2019; **Schuh et al., 2018**).

Whereas the parameters in case of basis functions with global support are physically interpretable as mean, trends and amplitudes, the parameters of the local basis functions are not directly interpretable. Instead, the large flexibility to model signals with various and non-homogeneous components are the advantage.

Independent of the type of the selected deterministic temporal model (2.31) and (2.32) are composed to a spatio-temporal model. Under the assumption of separability, the combined set of basis functions C_s result from the tensor product of the two sets T_s and S_s, i.e.

$$\mathrm{C}_s := \mathrm{T}_s \otimes \mathrm{S}_s = \left\{d_{s,j}(t) b_{s,i}(x,y) \quad | \, i \in 1...I_s,\, j \in 1..,J_s\right\}, \tag{2.34}$$

which results in $I_s \cdot J_s$ spatio-temporal basis functions. The linear combination

$$f_s(x,y,t) = \sum_{i=1}^{I_s} \sum_{j=1}^{J_s} e_{s,i,j} d_{s,j}(t) b_{s,i}(x,y) \quad f_s : \mathbb{R}^3 \to \mathbb{R}. \tag{2.35}$$

results in the spatio-temporal function in the new basis. $e_{s,i,j}$ are the scaling coefficients, which are then the unknown parameters in the spatio-temporal approximation task for some signal s.

Evaluating (2.35) for some constant time $t = t_c$ results in the function

$$\hat{f}_s(x,y) := f_s(x,y,t_c) \quad \hat{f}_s : \mathbb{R}^2 \to \mathbb{R}, \tag{2.36}$$

which describes the spatial signal s at t_c with the same smoothness properties as defined for the spatial FES. Furthermore, evaluating (2.35) for some constant location, i.e. $x = x_c$ and $y = y_c$ results in the time series

$$\bar{f}_s(t) := f_s(x_c, y_c, t) \quad \bar{f}_s : \mathbb{R} \to \mathbb{R}. \tag{2.37}$$

for the location with smoothness as for (2.32).

The same spatio-temporal model can be derived from a different point of view, i.e. the constant coefficients $a_{s,i}$ from the spatial function in (2.31) are allowed to vary in time. For that purpose, they are replaced by a one-dimensional functions in the time domain, i.e. they become

$$\alpha_{s,i}(t) := \sum_{j=1}^{J} e_{s,i,j} d_{s,j}(t), \tag{2.38}$$

where the temporal change of the coefficients is again represented as a linear combination of basis functions. Substituting (2.38) for all coefficients $a_{s,i}$ (2.31) results in the same spatio-temporal function as shown in (2.35).

Due to the flexibility of the FEs in spatial domain and the flexible choice of basis functions in the temporal domain, a wide range of spatio-temporal signals with different characteristics can be represented with this kind of deterministic functions. As a disadvantage, especially in case the temporal model has many parameters, the number of unknowns, as it is $I \cdot J$ can become huge, which requires either the use of HPC or a utilization of the special properties of the resulting system of equations. For instance, separability of spatial and temporal in case of identical measurement positions in all time series can lead to highly efficient implementations (for details see **Schuh et al., 2023**).

2.4 Utilizing Modern Concepts of HPC

Using deterministic approaches for spatial – and especially spatio-temporal – approximation tasks requires the solution of a high-dimensional, sometimes even ill-posed data fitting problem. In the applications discussed in Chapters 3 to 5, 10^4 to 10^6 unknown parameters are estimated from 10^5 to 10^7 correlated observations within a (constrained) least squares adjustment. Iterative refinements, e.g. either of the stochastic model (cf. Sect. 2.2), for outlier detection, for optimal design of the mesh in case of FE or, when optimizing relative weights for the combination of complementary data sets by variance component estimation (VCE), even require a repeated assembly and solution of the problem.

Due to the nature of the basis functions which are mainly spherical harmonics in the applications from Chap. 3 and 4, mostly dense matrices are involved while solving the problem. To handle the computational challenges and to derive a rigorous solution, dedicated tailored algorithms and strategies are developed and a generic implementation for a massive parallel compute cluster is derived in the C++ programming language. The general strategies applied here are inline with the strategies proposed and followed in Brockmann et al., 2014b; Brockmann et al., 2014c and Brockmann, 2014. Within the implementation, all involved matrices are managed by distributing individual blocks onto several compute nodes in order to flexibly handle a wide range of problems. This means all matrix data is stored (blockcyclically) distributed along the available compute cores which are arranged as a two-dimensional compute core grid (e.g. Blackford et al., 1997; Brockmann, 2014; Kurzak et al., 2017).

Consequently, all algorithms are designed and implemented to operate on the distributed matrix data either based on the Scalable Linear Algebra PACKage (ScaLAPACK) layout (Blackford et al., 1997) or the modern and newly implemented Software for Linear Algebra Targeting Exascale (SLATE) layout (Kurzak et al., 2017). This includes for instance the decorrelation and filtering strategies discussed in Sect. 2.2, the reordering required for data combination on the level of NEQs, or the evaluation of basis functions to setup design matrices based on symbolic numbering schemes (**Brockmann and Schuh, 2016a**) in its distributed layout.

Whereas the application from Chap. 3 is based on a classical implementation with ScaLAPACK, the implementation derived for the applications from Chap. 4 and partially Chap. 5 uses the modern SLATE library with an updated tile based memory layout. Within the work and projects associated to this thesis, the software package mpFRAGMENT is designed as a generic solver for high-dimensional adjustment problems from complementary data[2]. It is implemented in C++ and parallelized with Message Passing Interface (MPI). The intensive use of BLAS, Linear Algebra PACKage (LAPACK) and SLATE for the basic matrix computations ensures the optimization for different hardware platforms. Compared to the ScaLAPACK layout, the tile based approach

---

[2] Based on the initial developments from the DFG project Rigorous computation of high resolution spherical harmonic gravity models on massively parallel computer systems (G/O2000) funded by DFG (2012-2014) and extended in the context of the project PARASURV, see Chap. 4.

is more flexible. Whereas ScaLAPACK stores all local matrix data within a single heap block, i.e. all local matrix blocks jointly, the tile based approach allocates heap memory for all local matrix blocks individually. Consequently, memory management gets more complicated and an overhead is introduced. But, as all tiles are individually accessible, this is very well suited for hybrid parallelization approaches, e.g. via an integrated support of Graphical Processing Units (GPUs), accelerators or Open Multi-Processing (OpenMP) for local, i.e. tile based computations (Gates et al., 2019; Kurzak et al., 2017; Gates et al., 2020). Additionally, individual tiles can be empty, which is in contrast not possible due to the continuous layout in ScaLAPACK, thus making SLATE memory and computationally efficient for symmetric, triangular, banded and sparse matrices. As an early adopter of the library some feedback and bug-fixes have been contributed to SLATE. Furthermore, required extensions have been developed and implemented locally, e.g. for matrix reordering.

The developed software package mpFRAGMENT is successfully used on various HPC systems, including a local HPC cluster with 1984 nodes[3], the Bonna cluster operated by the University of Bonn and on the Jülich Wizard for European Leadership Science (JUWELS) system in context of the projects HBN15[4] and MAPSTER[5].

In the MSS application from Chap. 5, the computational challenges are different. As only FEs are involved in the spatial domain of the approximation task, the matrices are extremely sparse. Due to the combination of the spatial and the temporal basis functions (cf. Sect. 2.3.4), the parameter space is large, especially in case of basis functions with local support for the temporal model. But, optimizing the numbering scheme, or applying reordering strategies (e.g. George and Liu, 1981) the sparsity can be well preserved and utilized while assembling and solving the approximation task. As an example, Fig. 2.9 shows the sparsity pattern for NEQ matrix of a spatial approximation with the Argyris element in an arbitrary ordering, and after reordering with the reverse Cuthill-McKee algorithm and nested dissection (e.g. George and Liu, 1981) both of which are very well suited for exploiting the sparsity while solving the system of equations.

Although the spatio-temporal approximation is implemented in mpFRAGMENT as well and applied for MDT estimation in Chap. 4, for the application from Chap. 5 an environment which supports flexible handling of sparsity is more important. The results presented in **Borlinghaus et al., 2023a** and **Borlinghaus et al., 2023b** have been computed entirely with MatLab® with its efficient realization of sparse matrix support (Gilbert et al., 1992).

---

[3] Financed via a DFG Forschungsgroßgeräteantrag (INST 217/747-1 FUGG)

[4] Project Adaptive Optimization of Global Gravity Field Modeling and the Ocean's Dynamic Topography (HBN15), application for computing time on supercomputers granted by the John von Neumann Institute for Computing (NIC) on the GCS Supercomputer JUWELS at Jülich Supercomputing Centre (JSC) (CO-PI: J.M. Brockmann).

[5] Project MAssive Parallel Approximation of Static and Time-VariablE Reference Surfaces with C^1-smooth Finite Element Model Functions (MAPSTER), application for computing time on supercomputers granted by the NIC on the GCS Supercomputer JUWELS at JSC (PI J.M. Brockmann).

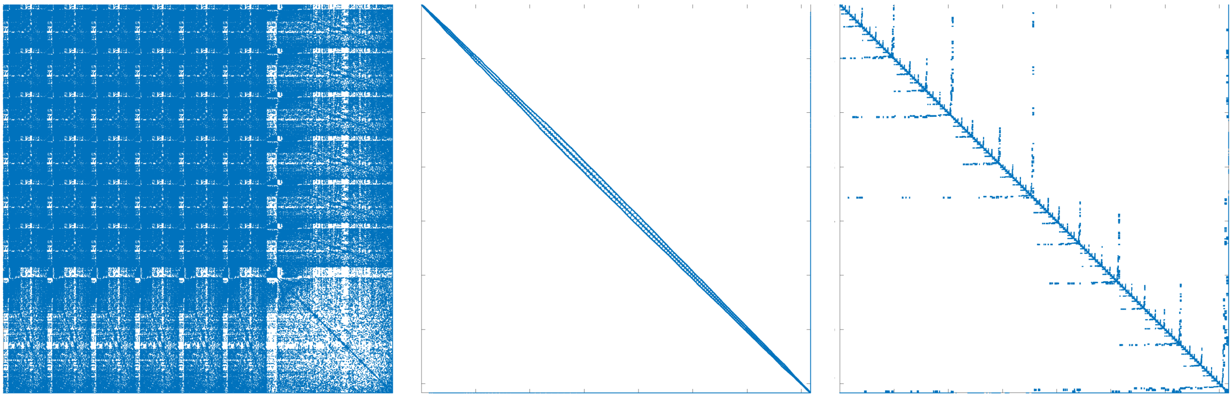

(a) Spy plot for the matrix in arbitrary ordering.

(b) Spy plot after reverse Cuthill-McKee reordering.

(c) Spy plot after nested dissection reordering.

Figure 2.9: Spy plot for a NEQ matrix (71 714 × 71 714) from a spatial approximation with the Argyris element in different orderings. The example matrix contains 3 523 132 non-zero elements, i.e. 0.69 ‰.

Chapter 3

Determination of Satellite Based Global Gravity Field Models

This chapter is based on the work performed in the GOCE-HPF[1] and the unfunded GOCO[2] consortium. Therefore, parts of this chapter are taken in an updated version from the proposal, project reports, technical notes, resulting joint project publications and conference contributions.

3.1 Introduction and State of the Art

The mean Earth's gravity field is an important physical reference surface in various disciplines. For example, the static geoid serves as a reference for the definition of height systems in geodesy (e.g. Gruber et al., 2012; Gerlach and Rummel, 2013) or it is required for the (geodetic) determination of the MDT and the steady-state ocean circulation (see e.g. Volkov and Zlotnicki, 2012; Rio et al., 2014 and Chap. 4). At global scales, the models are parameterized by global Spherical Harmonic (SH) basis functions (e.g. Barthelmes, 2013; Heiskanen and Moritz, 1993, Chap. 2). As this parameterization is used in the contributions discussed here, the alternatives using local basis functions like splines or wavelets are not discussed, instead the reader is referred to Schmidt et al., 2007 and the references therein for a detailed discussion.

Especially since the launch of the dedicated satellite missions CHAMP, GRACE, GOCE and GRACE-FO various approaches have been developed to determine static and time-variable global gravity field models from the collected observations. For an overview see the excellent review papers by Rummel et al., 2002, Rummel, 2020 or Flechtner et al., 2021 and the corresponding references. As in this thesis and the included contributions the focus is on static reference surfaces – a detailed discussion of the estimation of time-variable gravity fields is excluded (see for instance Kvas et al., 2019a; Dahle et al., 2019; Kurtenbach et al., 2012; Tapley et al., 2004).

The use of (dedicated) satellites for the recovery of the Earth's gravity field has the advantage that a homogeneous global data sampling becomes possible. For each mission a consistent set of observations is available for gravity field recovery. This allows for a rigorous stochastic modeling, characterizing the uncertainties of the observations. Propagating the uncertainties through the recovery procedures yields in addition to the gravity field a realistic covariance matrix describing its uncertainties (e.g. Schuh et al., 2010; Farahani et al., 2013; Kvas and Mayer-Gürr, 2019; Kvas et al., 2019a; Lasser, 2023).

Typically, in a first step, the observations of the different missions like CHAMP, GRACE, GOCE or GRACE-FO are analyzed by processing centers, which estimate mission-only solutions, using tailored approaches depending on the observed functionals (e.g. Reigber et al., 2005; Beutler

---

[1] Project GOCE High Level Processing Facility (GOCE-HPF), European Space Agency (ESA) contract no 18308/04/NL/MM (2004-2020)

[2] Project Gravity Observation COmbination, unfunded consortium, `www.goco.eu` (2006-ongoing)

et al., 2010; Mayer-Gürr et al., 2018; Dahle et al., 2019; Chen et al., 2018; Brockmann et al., 2014a; Gatti et al., 2016; Wu et al., 2017). With the focus on the static gravity field — i.e. the mean — the mission-only solutions reflect the average signal over the observation period, which defines the mission-specific reference period of the static solutions.

Mainly for missions with a long observational record, or missions with a high sensitivity for the (relatively small) temporal signal at large spatial scales (especially GRACE, GRACE-FO and Satellite Laser Ranging (SLR) and Low Earth Orbiters (LEOs) derived models) the long term temporal signal is often co-estimated (e.g. Löcher and Kusche, 2020; Lück et al., 2018; Förste et al., 2016). Similar to the approach discussed in Sect. 2.3.4, separable basis functions for the spatial and the temporal domain (e.g. linear trends and seasonal harmonics) are combined to obtain a spatio-temporal model. Long-term temporal variations are co-estimated to avoid aliasing and to obtain a clear definition of the reference epoch. Due to the huge number of observations (e.g., 440×10^6 for GOCE mission) collected by the satellites over their mission lifetimes with a quite high sampling rate, gravity field recovery is a computationally challenging task (Brockmann, 2014, Chap. 6) requiring the use of HPC. Often, these global gravity field models are parameterized by a SH series. Depending on the mission and the measurement principle, the spatial resolution of the models is limited – a maximum resolution of spherical harmonic degree and order (d/o) 300 can be obtained from the GOCE mission. This results in 90 597 SH parameters, which are typically estimated from the observations via the solution of a linear or linearized ill-posed inverse problem (e.g. Kusche and Klees, 2002; Ditmar et al., 2003; Pail and Plank, 2003). Each of the derived gravity field models have different strengths and weaknesses – depending on the quality of the observations, the measurement principle and the mission design. Using a proper stochastic model and rigorous variance propagation, the individual strengths and weaknesses are included in the full covariance matrix of the SH parameters of the individual solutions.

To reduce the mission specific weaknesses in the gravity field models, the model specific solutions can be combined — in a first step to the so-called satellite-only models. Satellite-only models still have the advantage that they are computed from a homogeneous data-distribution with consistent quality. Various models (e.g. Farahani et al., 2013) and even model series (e.g. Reigber et al., 2002) are published. For a nearly complete overview see the database as published by International Centre for Global Earth Models (ICGEM) (Ince et al., 2019). The recently most accepted series are the GOCO0*S (Pail et al., 2010) models[3], the European Improved Gravity model of the Earth by New techniques (EIGEN)*S models (e.g. Förste et al., 2008) and the GOCE models computed with the so called direct approach, which are in fact combined satellite-only models (Bruinsma et al., 2013; Bruinsma et al., 2014). Main contributors to the combined satellite-only models are GRACE/GRACE-FO and GOCE followed by gravity field models derived from orbit perturbations of LEOs (e.g. Löcher, 2010; Baur et al., 2014) and from SLR observations (e.g. König et al., 1999; Sośnica et al., 2015; Maier et al., 2012). Whereas SLR is very important for the lowest SH degrees (especially degrees 2 to 4, e.g. Maier et al., 2012), the orbit derived models are mainly sensitive to the longer wavelengths up to degree 10 and some sectorial coefficients of higher degrees (e.g. **Kvas et al., 2021**). Due to the measurement principle, GRACE/GRACE-FO K-band range-rate measurements contribute to the low to the medium degree range 100 to 150 (e.g. Pail et al., 2010). The maximal resolution of the combined satellite-only models is defined by the GOCE contribution. Depending on the utilized data, the GOCE models are resolved up to SH d/o 250 to 300. Except for the zonal coefficients, which are affected by a polar data gap resulting from the sun-synchronous orbit, GOCE gravity gradient measurements contribute from degree 100 onwards. The computation of the combined models is typically performed combining the unconstrained individual mission-only solutions on the level of NEQs (e.g. Pail et al., 2010; Brockmann et al., 2014c; Brockmann, 2014). Although, due to an iterative estimation of relative weights (e.g. Koch and Kusche, 2002) the procedure has to be repeated, the computational challenge is limited. A weighted sum of preprocessed NEQs is computed and solved, which due to limited SH resolution

---

[3] To which we contribute as a member of the GOCO consortium, see `www.goco.eu` for further details.

is an easily manageable task when applying massive parallel HPC (Brockmann, 2014). A more important part is to establish efficient reordering strategies to combine the different NEQs assembled for different subsets of the SH parameters (**Brockmann and Schuh, 2016a**).

Last but not least, combined gravity field models can make use of regionally available terrestrial gravity data sets, topography derived gravity and altimetry derived gravity over the oceans (e.g. Pavlis et al., 2012; Förste et al., 2014; Zingerle et al., 2020) to combine all information available. Densely sampled terrestrial gravity observations increase the spatial resolution of the gravity field models significantly – down to a few kilometers. In terms of SHs, models are resolved even above d/o 2000, resulting in millions of unknown parameters for which the estimation is a large computational challenge (Brockmann, 2014; Brockmann et al., 2014c). Often, block-diagonal approximations are introduced (e.g. Schuh, 1996; Boxhammer and Schuh, 2006; Pavlis et al., 2012; Förste et al., 2014; Zingerle et al., 2020) which requires a regular gridding of available data. In addition a homogeneous data quality is required to obtain block-diagonal NEQs, which is obviously not the case for data bases collecting data from several measurement campaigns spread over decades. Furthermore, gravity derived from altimetry is biased towards an a-priori MDT model and, therefore, to an a priori geoid as well (see Chap. 4 for a more detailed discussion on the dependence).

3.2 Objectives and Contributions

For the geodetic determination of the MDT, a (static) geoid model is required as a reference (cf. Chap. 4). To use the geoid as a stochastic data set, a realistic covariance matrix is required. This can be provided in case consistently processed observations enter the estimation approach. This is the case for satellite based observations of a single mission. Therefore, in a first step, typically mission-only models are estimated, which are combined to satellite-only models in a second step. In this thesis, contributions to both entered, i.e. to the estimation of mission-only and based on that satellite-only models, which serve as a basis for the MDT estimation from Chap. 4. In the GOCO consortium, the satellite-only models were further processed to consistently derive combined gravity field models, which can serve as reference for other geodetic applications.

In the context of gravity field determination the contribution is mainly within the processing of GOCE gravity gradient data (SGG). After the official completion of the GOCE mission with the publication of the release 5 models, where the so called time-wise solution is the official ESA GOCE-only solution (Brockmann, 2014; Brockmann et al., 2014a), further studies on the quality and the characteristics of the unique gravity gradient data set were performed. It was found that on the one-hand the calibration, which is required to derive the Level 1b data from the Level 0 data, was imperfect. Methods to improve the calibration were developed (Siemes, 2018b; Siemes, 2018a). This directly leads to improved gravity gradient observations, which serve as input for gravity field recovery. On the other hand, it was shown that the estimation of the stochastic characteristics can be improved applying a robustified estimation strategy, which directly identifies suspicious data in the huge number of measurements (cf. Sect. 2.2, **Schubert et al., 2021b**). The improved methodology yields a significantly better gravity field estimate, as the relative weighting of the different components of the gravitational tensor is improved — the individual strengths and weaknesses of the different gravity gradient components are better kept in the combination (**Brockmann et al., 2015; Schuh and Brockmann, 2016; Brockmann et al., 2017**). These studies served as a basis for a reprocessing campaign initiated by ESA towards a new Level1B data set and a sixth release of the gravity products, including the global gravity field models (**Gruber and Team, 2018**). In this reprocessing campaign, the sixth release of the GOCE time-wise solution was derived (**Brockmann et al., 2021; Brockmann et al., 2019d**) applying the improved stochastic modeling (**Schubert et al., 2021b**) to the improved input Level1B data (Siemes et al., 2019b; Siemes et al., 2019a). This does not only lead to a significantly improved GOCE-only solution but to a more realistic covariance matrix of SH parameters as well (**Brockmann et al., 2021; Brockmann et al., 2019d**). This is essential when the model is used in the combination for deriving satellite-only models (**Kvas et al., 2021; Kvas et al., 2019b**). The published sixth release of the time-wise model is one of just a few GOCE-only models and internationally accepted and known for the quality of the covariance estimate.

The aforementioned features make the time-wise GOCE models (in an unconstrained version) a perfect input for combined satellite-only models. In the framework of the GOCO consortium[4], where experts for GRACE/GRACE-FO, GOCE, SLR, LEOs and terrestrial and altimetry derived gravity from TU Graz, TU München, University of Bern and University of Bonn jointly produced satellite-only and combination models for several years (Pail et al., 2010). The work from this thesis contributed to the sixth release, i.e. GOCO06S (**Kvas et al., 2019b; Kvas et al., 2021**) mainly with the GOCE gravity gradient processing, methodological contributions (e.g. **Brockmann and Schuh, 2016a**) and model validation/verification.

Within the GOCO consortium, the satellite-only models are extended for some releases to combined models, e.g. for the fifth release, ground gravity and satellite altimetry derived data was added to obtain a combined model up to SH d/o 720 to obtain GOCO05c (**Pail et al., 2016; Fecher et al., 2017**). Alternatively, terrestrial data can be included to overcome data gaps. The GOCE mission has a sun-synchronous orbit with an inclination of 96.7° (Floberghagen et al., 2011), which leads to a data gap in the polar areas. Whereas this gap is filled with pseudo zero gravity observation in the GOCE-only time-wise model (**Brockmann et al., 2021**), real terrestrial data – filtered down to the maximal resolution of the GOCE contribution – is used in **Zingerle et al., 2019** to fill the gap.

3.3 Background and Key Features of the Approach and the Estimated Models

3.3.1 Representation with Spherical Harmonics

Satellite derived global gravity field modes are typically parameterized by a finite spherical harmonic series, truncated at a maximal SH degree $l_{\max}$. The gravity potential as a function of the evaluation point with spherical coordinates $(r,\ \lambda,\ \varphi)$ then reads (cf. Hofmann-Wellenhof and Moritz, 2005; Barthelmes, 2013)

$$V(r,\lambda,\varphi) = \frac{GM}{R} \sum_{l=0}^{l_{\max}} \left(\frac{R}{r}\right)^{l+1} \sum_{m=0}^{l} P_{lm}\left(\sin\varphi\right)\left(c_{lm}\cos(m\lambda) + s_{lm}\sin(m\lambda)\right). \tag{3.1}$$

Here GM and R are the gravitational constant of the Earth and the mean equatorial radius respectively, and $P_{lm}\left(\cdot\right)$ are the fully normalized associated Legendre functions. c_{lm} and s_{lm} are the Stokes coefficients, which are the unknowns in the context of gravity field determination. Reducing the potential by the normal potential $U\left(r,\varphi\right)$ generated by a reference ellipsoid results in the disturbing potential, i.e.

$$T(r,\lambda,\varphi) = V(r,\lambda,\varphi) - U\left(r,\varphi\right). \tag{3.2}$$

Given the spherical harmonic coefficients, various functionals like the geoid, deflections of the vertical or gravity can be evaluated, see Barthelmes, 2013 for an excellent summary and the required formulas.

3.3.2 Key Features of the Time-Wise GOCE Models

One of the core instruments of GOCE is the unique three axis gradiometer. Operating in a drag free environment, SGG derives the gravity gradients via differential accelerometers, i.e. the six second derivatives of (3.1) are measured in the Gradiometer Reference Frame (GRF). The GRF

---

[4] For details see `www.goco.eu`.

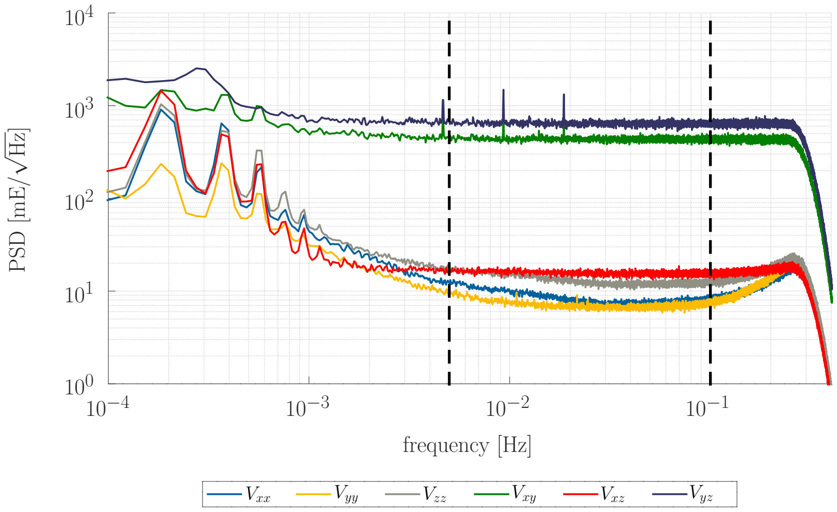

Figure 3.1: PSD of the gradiometer noise estimate for the different gravity gradient components. It is computed by Welch's method (e.g. Oppenheim et al., 1999, Sect. 10.6) from residuals with respect to the EGM_TIM_RL06 solution from the time series August to September 2013. Figure is taken from **Brockmann et al., 2021**.

is a local Cartesian reference frame fixed to the gradiometer, with the x-axis roughly pointing in flight direction, the y-axis is orthogonal to the orbital plane, and the z-axis radially pointing downwards (cf. Rummel et al., 2011). Together with the satellite positions, derived from tracking with the Global Positioning System (GPS) constellation, the orientation of the satellite in space, derived from star cameras and a time stamp for synchronization, the SGG observations are the main observable for GOCE static gravity field recovery (Pail et al., 2011).

Although GOCE measures all six gravity gradients, i.e. V_{XX}, V_{XY}, V_{XZ}, V_{YY}, V_{YZ} and V_{ZZ}, both, the V_{XY} and V_{YZ} are of poor quality. By design, the noise level is two orders of magnitudes higher (e.g. Rummel et al., 2011, **Brockmann et al., 2021**), therefore they are not used for gravity field recovery. To highlight this characteristics, Fig. 3.1 shows the Power Spectral Density (PSD), computed from least squares residuals as realization of the measurement noise, for all six gravity gradient components. In addition to the significantly higher noise level for the V_{XY} and V_{YZ} component the strong correlations in the low frequencies are visible, especially for the usable gradients. For gravity field recovery, the second derivatives of (3.1) are transformed to the GRF, which leads to least squares OEQs linear in the unknown gravity field parameters c_{lm} and s_{lm}.

Due to the nature of the SGG data — being second derivatives of the potential — gradiometry can not accurately map the long wavelength of the gravity field, see the high noise level of the gradients for the small frequencies in Fig. 3.1. Therefore, the kinematic orbit positions derived from the tracking of the GPS satellites (Satellite-to-Satellite Tracking (SST)) can be used as additional observables to determine the long wavelengths. Several procedures exist, see e.g. Baur et al., 2014, which were developed for the CHAMP mission (see e.g. the compilation of approaches in Löcher, 2010). Within the time-wise approach the Energy Balance Approach was applied in releases one to four (Gerlach et al., 2003), which was replaced by the short arc integral equation approach (Mayer-Gürr et al., 2005) for releases five and six (Brockmann et al., 2014a, **Brockmann et al., 2021**). As this data is processed in the GOCE-HPF consortium by the colleagues from the Institute of Geodesy of the Graz University of Technology and enters the time-wise model as already preprocessed least squares NEQs in the SHs domain, we will not focus on the processing here. Instead the NEQs derived from the SST data are directly used in the combination with the SGG data.

The estimation of a gravity model from the observations collected in space is in general an ill-posed inverse problem (e.g. Ilk et al., 2002). This is exacerbated by the polar data gap resulting from the sun-synchronous orbit. Therefore, regularization strategies are required to derive a stable GOCE-only solution.

The key features of all the released time-wise models are that they are GOCE-only models reflecting the Earth's gravity field as seen by GOCE in a best possible way (Pail et al., 2010). Furthermore, the associated covariance matrix is supposed to realistically reflect the uncertainty of the models. To achieve these features, it is required to carefully model the stochastic characteristics of the used input observations. On the one hand, the stochastic model controls the spectral weighting when combining the complementary observation types, which are in the context of GOCE the SST and SGG observations, including the different gradient components V_{XX}, V_{XZ}, V_{YY} and V_{ZZ} as they have different sensitivity characteristics as well (Schuh, 1996; Pail et al., 2010; Rummel et al., 2011). This directly influences the quality of the gravity field itself. On the other hand, the stochastic model is propagated through the analysis procedure, and thus directly influences the quality of the final covariance matrix.

3.3.3 Key Features of the GOCO Models

In contrast to the GOCE-only model, the GOCO0*S models are satellite-only models. Key idea of the GOCO consortium is to bring together experts for the different gravity field missions, which produce well established mission-only models. The GOCO models are produced by colleagues from the Institute of Astronomical and Physical Geodesy at TU München (validation, terrestrial gravity), the Institute of Geodesy at TU Graz (GRACE, SLR, LEO, combination and computing), the Astronomical Institute at University of Bern (GRACE, SLR, LEO, GOCE) and the Institute of Geodesy and Geoinformation at University of Bonn (GOCE, combination and computing).

As the standard representations of the global models are SHs, the production of a combined model of unconstrained versions from the mission-only models is straight forward. After homogenization of the background models, reference epochs, defining constants and elimination of mission specific parameters the combination can be performed on the level of (unconstrained) NEQs (e.g. Meissl, 1982; Pail et al., 2010; Brockmann, 2014). Again, an optimal solution including the strengths of the individual missions and minimizing the weaknesses, requires that the covariance matrices of the mission-only models are as realistic as possible. This fact makes the GOCE time-wise models with its key target features an ideal input model to a combined satellite-only model.

Due to the sensitivity of the gradients to the medium to short wavelengths, GOCE can not properly resolve temporal variations of the gravity field, therefore the GOCE-only models are static mean fields with a reference epoch in the middle of the GOCE time series. This holds true for all gravity field contributions determined from the GPS tracking of LEO satellites. As in contrast to this, the observation principle of GRACE is designed to capture the temporal variations, this needs to be accounted when combining GRACE-only with the static contributors to avoid aliasing. This is realized by co-estimating a spatio-temporal model for the time-variable gravity field, combining the spatial SH with deterministic functions for linear trends and annual harmonics, similar to the approach discussed for the FE as shown in Sect. 2.3. Similarly, this holds true for SLR derived gravity fields.

In the GOCO consortium, the satellite-only version serves as background model for combined models with terrestrial and altimetry derived gravity data. Again, the unconstrained NEQs of the satellite-only model can be combined with NEQs assembled from terrestrial gravity and altimetry derived gravity data sets (**Fecher et al., 2017**).

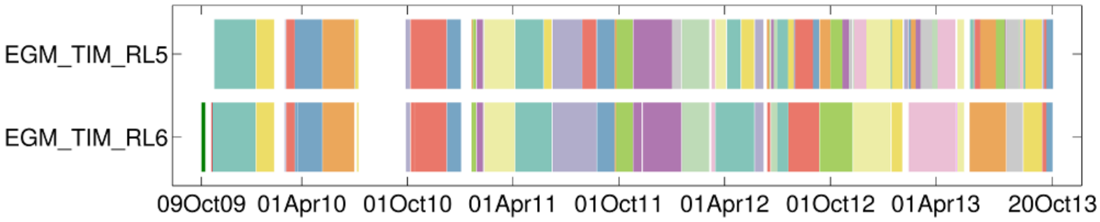

Figure 3.2: Segmentation of the GOCE gravity gradients into gap less segments with similar stochastic characteristics for the RL05 and RL06 processing. Figure is taken from Brockmann et al., 2019c.

3.4 Selected Results

3.4.1 Improvements of the Time-Wise Release Six Model

Major output of the work performed in the context of this thesis is the sixth release of the time-wise GOCE model, tagged as GO_CONS_EGM_TIM_RL06 (**Brockmann et al., 2019d; Brockmann et al., 2021**) or in short EGM_TIM_RL06 . Compared to the predecessor EGM_TIM_RL05 (cf. Brockmann et al., 2014a) the major improvements result from the improved level 1B input gradient data, the improved precise science orbits (Arnold et al., 2023) as well as the advanced processing, which significantly improved stochastic modeling of the gravity gradients. For most improvements it is hardly possible to attribute them to one of the updates, as the imperfectly calibrated data used in EGM_TIM_RL05 caused non-stationary characteristics, which severely affected the quality of the previously utilized stochastic model. Evaluation has shown that the mean global accuracy from RL05 to RL06 increased by 10 % to 25 %. Furthermore, systematic errors close to the magnetic poles (calibration errors of gradients, Siemes et al., 2019b) and the magnetic equator (orbits errors, Arnold et al., 2023) were reduced at centimeter level in terms of geoid.

Improved Stochastic Model of Gravity Gradient Observations

For the estimation of the stochastic model and for the decorrelation, the basic idea of the time-wise approach is to treat the individual gravity gradient components V_c for $c \in \{XX, XZ, YY, ZZ\}$ as a time series along the orbit. Assuming that the measurement noise of the different components are uncorrelated, i.e.

$$\mathbf{\Sigma}\left\{V_{c_1}, V_{c_2}\right\} = \mathbf{0}, \qquad c_1, c_2 \in \{XX, XZ, YY, ZZ\}, \quad c_1 \neq c_2, \tag{3.3}$$

least squares residuals $\mathbf{v}_c$, in a first iteration with respect to EGM_TIM_RL05, later from the adjustment, are used to iteratively refine the stochastic model $\mathbf{\Sigma}\{V_c\}$ per component.

As stochastic processes are used for covariance modeling (cf. Sect. 2.2), it is required that the time series are without data gaps. Therefore, the time series are segmented into gap less segments $V_{c,s}$ with $s \in \{1, \dots, S\}$. Furthermore, it is assumed that different segments are uncorrelated, i.e.

$$\mathbf{\Sigma}\left\{V_{c,s_1}, V_{c,s_2}\right\} = \mathbf{0}, \qquad s_1, s_2 \in \{1, \dots, S\}, \quad s_1 \neq s_2. \tag{3.4}$$

As for covariance estimation the assumption of stationarity is required to obtain redundancy, an additional subdivision of the segments is artificially introduced during the processing after i) major events and maneuvers related to the satellite from which a change of the noise characteristics can be expected, ii) after a change of the noise characteristics is identified, or iii) huge outliers or clusters of suspicious data were identified. Although different stochastic processes and different estimation procedures are applied in EGM_TIM_RL05 (Brockmann, 2014; Brockmann et al., 2014a) and EGM_TIM_RL06 processing (**Schubert et al., 2021b; Brockmann et al., 2021**), the same segmentation strategy was applied. Fig. 3.2 shows the final segmentation used in both releases, where it can be seen that thanks to the robustified process estimation strategy (cf. Sect. 2.2.1, **Schubert et al., 2021b; Brockmann et al., 2021**) and the improved L1B data quality fewer and thus longer segments were used in the RL06 processing, which increases the stability of the decorrelation filter estimates.

For all segments indicated in Fig. 3.2, ARMA filters were manually adjusted to outlier free subsets of the residual time series (Krasbutter et al., 2011; Krasbutter et al., 2014; Brockmann, 2014) in the RL05 processing. In contrast, the robustified estimation of AR processes is applied in RL06, which does not only yield the estimated decorrelation filters but additionally the locations of outliers and suspicious data based on the statistical tests (cf. Sect. 2.2.1, **Schubert et al., 2021b**). These identified data points are not used for gravity field recovery and excluded in the estimation.

The estimated processes can be well represented in the spectral domain. Fig. 3.3 shows the PSD of the processes used in RL05 processing (left column) and in RL06 processing (right column) for all components c (rows) and all segments s (color coded). Thus, corresponding plots in the same row, compare the estimated noise characteristics from RL05 and RL06 processing. Plots in the same column show the characteristics of the different gravity gradient components and therefore provide a hint about the stationarity of the noise. Comparing different colors in a single sub-plot shows the noise characteristics for different segments and thus periods of the mission.

Firstly, it is directly visible that the stationarity of the estimated gravity gradient noise significantly improved from RL05 to RL06. There are strong variations for RL05 showing an increased noise towards the end of the mission, where the satellite was operated at a lower orbit while the solar activity increased. In contrast to this, the PSDs estimates of RL06 are very consistent – especially in the measurement band between 5 mHz to 100 mHz, which shows the improved data quality, especially for the important low orbit data. The change of the characteristics is most obvious for the YY gradient, which was mostly affected by the imperfect calibration. The single segment visible in the V_{ZZ} plot is the first long segment, which was of poor quality as it recorded data before an update of the gradiometer control unit.

In addition to an increased stationarity, the noise level is in generally lower for the smaller frequencies, even reaching the measurement band (for all components and all mission periods). The noise estimates obtained in the RL06 processing shows close to white noise characteristics not only in the measurement band, but down to 2 mHz.

The visible improvements result from both, the improved input data and the updated stochastic modeling. The improved calibration directly reduces the noise level, especially for V_{YY}. Additionally, the robustified estimation of the process is less influenced by outliers and suspicious data, which do not leak into the estimated stochastic model. Therefore, the estimated processes better reflect the characteristics of the 'non-suspicious' majority of the data.

Detection of Suspicious data

As discussed in Sect. 2.2.1, suspicious data points and outliers are directly identified by the robustified AR process estimation approach. Of course, it is of interest to study whether the classification as suspicious data or outliers is meaningful. During processing, a large number of data classified as suspicious was detected in the V_{XX} and V_{XY} component. As an example Fig. 3.4 shows the detected outliers for the segment 2011/06/08 to 2011/08/23 consisting of 6.6×10^6 observations in the V_{XX} component. A quite large number of outliers was identified, especially by the variance test (cf. Fig. 3.4a), about 18.5 % were flagged using the originally planned sensitivity of the test.

Together with mission scientists from ESA, studies to identify the reasons for the clustered suspicious data were performed (**Brockmann et al., 2019b**). Despite some individual tracks identified as suspicious, the major part of the data classified as suspicious is located in the latitude band between 10 ° S and 60 ° S (**Brockmann et al., 2019b**).

It is known that the ion thruster compensating the drag generates an increased noise due to vibrations when firing at a level of 2000 mN to 2500 mN. Fig. 3.5a shows these actually delivered

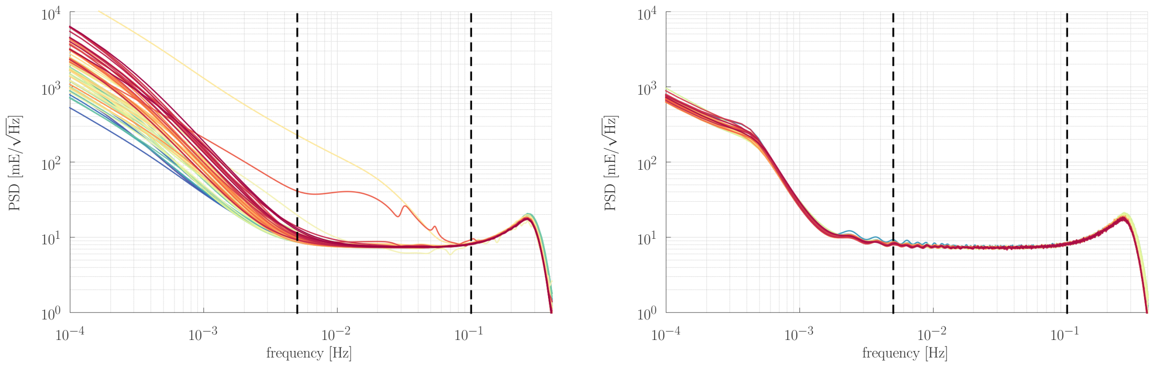

(a) V_{XX} RL05.

(b) V_{XX} RL06.

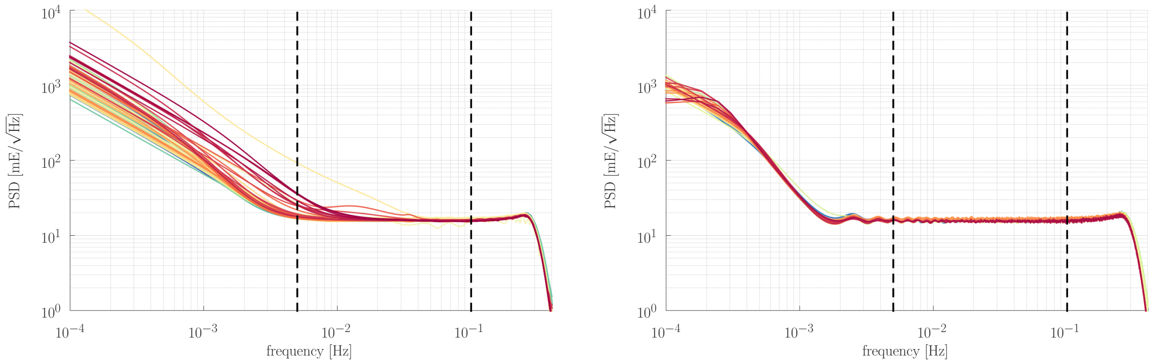

(c) V_{XZ} RL05.

(d) V_{XZ} RL06.

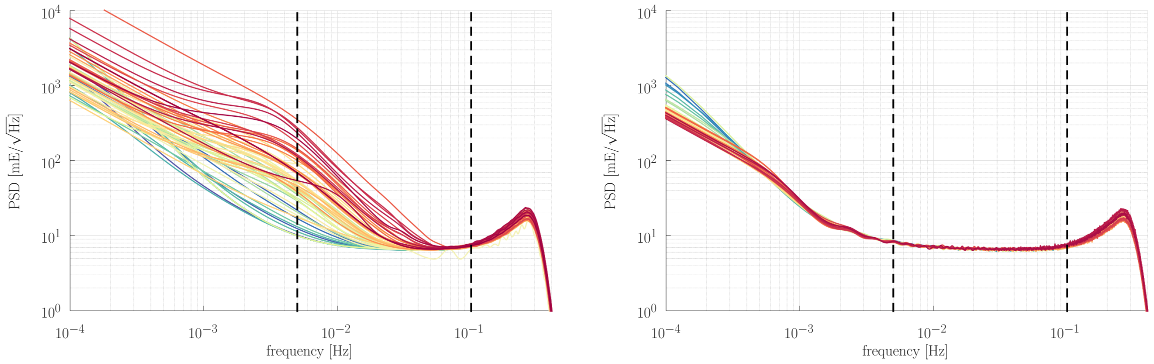

(e) V_{YY} RL05.

(f) V_{YY} RL06.

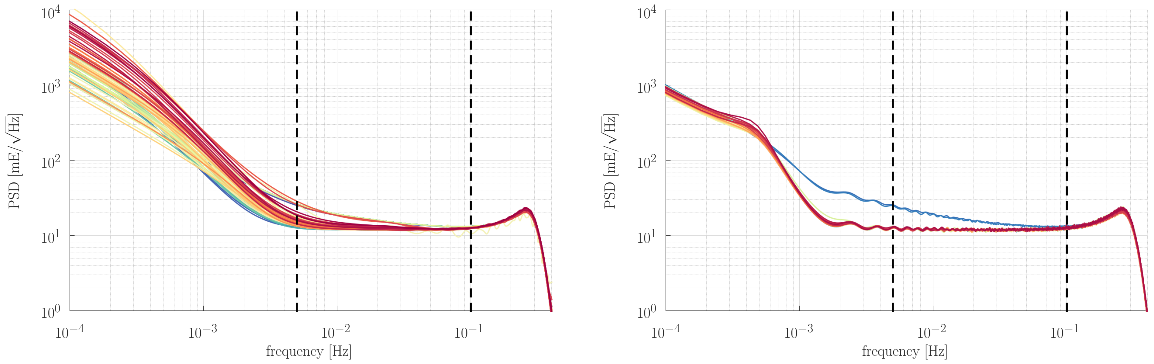

(g) V_{ZZ} RL05.

(h) V_{ZZ} RL06.

Figure 3.3: Comparison of the PSD of the decorrelation filter estimates for RL05 (left column) and RL06 (right column) for all used gravity gradient components. The blue to red color code corresponds to the segment numbers, where blue are segments early in the mission, red corresponds to the later ones. The dashed black lines indicate the measurement band. Note that due to the different segmentation, colors for RL05 and RL05 may correspond to different time periods. Figure is taken from **Brockmann et al., 2021**.

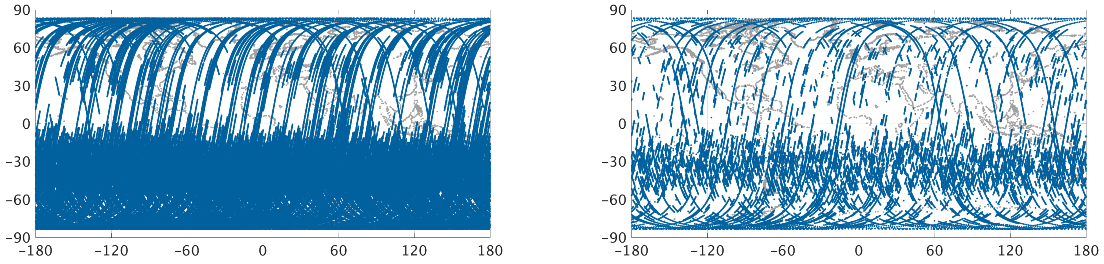

(a) Default test sensitivity of the variance test. (b) Reduced test sensitivity of the variance test.

Figure 3.4: Detected outliers and suspicious data in the V_{YY} gravity gradient for the segment 2011/06/08 to 2011/08/23 as a spatial plot. Figure is taken from **Brockmann et al., 2019b**.

thrust of the satellite, which is available from the house keeping data after a 0.05 Hz high-pass filtering in an argument of latitude representation as a time series for the segment mentioned above. The applied filtering pronounces those specific high thrust levels in the plot. Figures 3.5b and 3.5c show the detected suspicious data from Fig. 3.4 in the same argument of latitude representation. The correlation is obvious therefore it can be concluded, that the approach successfully identified suspicious data, with a different noise characteristic caused by the increased thruster noise level.

To utilize more data for gravity field recovery and to avoid artificial data gaps for the operational analysis, the sensitivity was decreased, resulting in 3.9 % of detected outliers in the V_{XX} component of the specific segment (cf. Fig. 3.4b).

Similarly, other effects were correlated to spatial patterns identified in the suspicious data. E.g. data when the satellite enters the eclipse shadow is identified as suspicious, thermal changes yield slightly changing data characteristics (**Brockmann et al., 2019b**). This confirms that the approach reasonably classifies data as suspicious which indeed has a different characteristic compared to the majority.

Internal Consistency of Gravity Gradient Solutions

Another option to asses the quality and consistency of the stochastic model is to compare the formal error estimates of the SH parameters to empirical estimates derived from the difference to a reference model. To obtain redundancy and to compare averages, degree (error) variances are well suited. But, as no reference model exists superior to the GOCE based estimate for all SH degrees, the idea is to compare segment- and component-wise solutions long enough that they are individually solvable to a final combined GOCE solution. As the final combined model is determined from significantly more data and all gravity gradient components, it is safe to assume that it is more accurate and can serve as a reference for consistency checks.

This is shown in Fig. 3.6, for one segment very early in the mission with low solar activity where the satellite was operated in a high altitude and thus in a smooth environment (11/2009–12/2009). A second segment towards the end of the mission (06/2013–07/2013) is added, where the orbit was lowered by 30 km and the solar activity was higher, so the satellite was operated in a rougher environment. Both segments have a length of roughly two months. These NEQs are individually solvable per gradient component and per segment without regularization. As reference model the finally combined EGM_TIM_RL05 solution is chosen. Degree error variances of the segment-wise and component-wise solutions are shown for both RL05 solution (in blue) and the corresponding RL06 (in orange) counterpart. Whereas the formal degree error variances are computed from the standard deviations of the SH coefficients (dashed lines) the empirical error estimates follow from the difference to the EGM_TIM_RL05 model (solid lines). To suppress the effect of the polar gap,

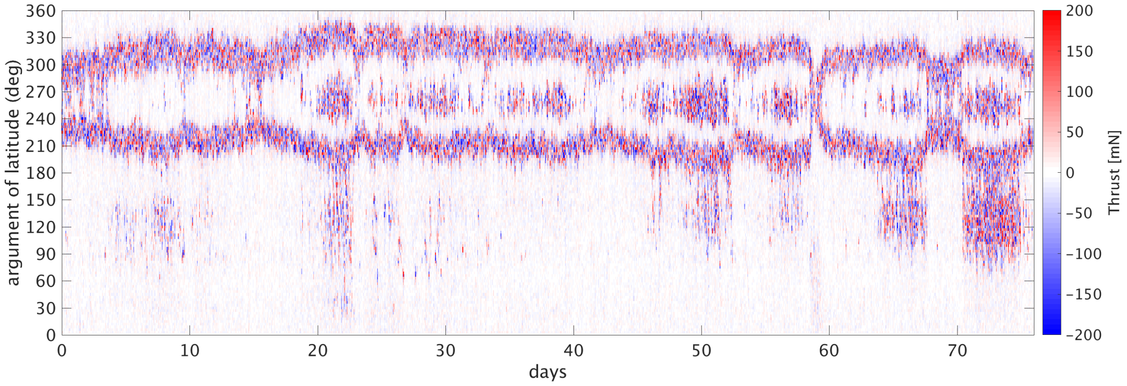

(a) Delivered thrust after 0.05 Hz high-pass filtering. Courtesy C. Siemes.

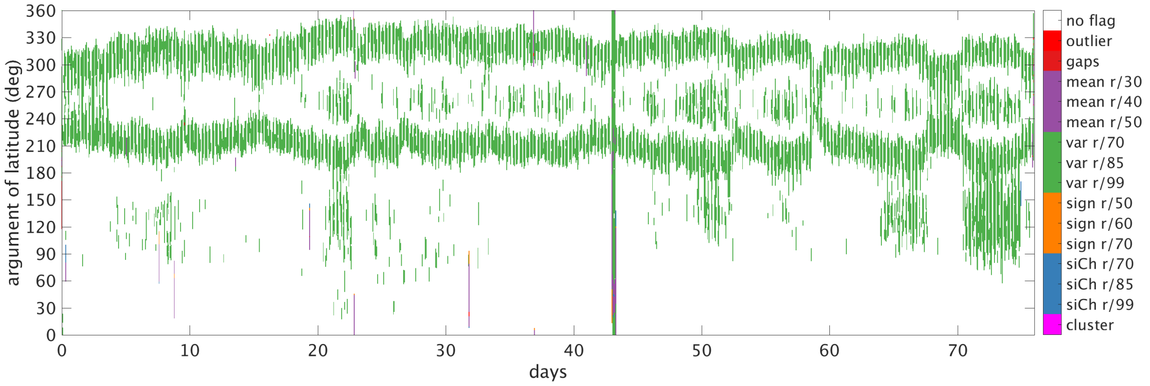

(b) Outliers detected with default test sensitivity of the variance test.

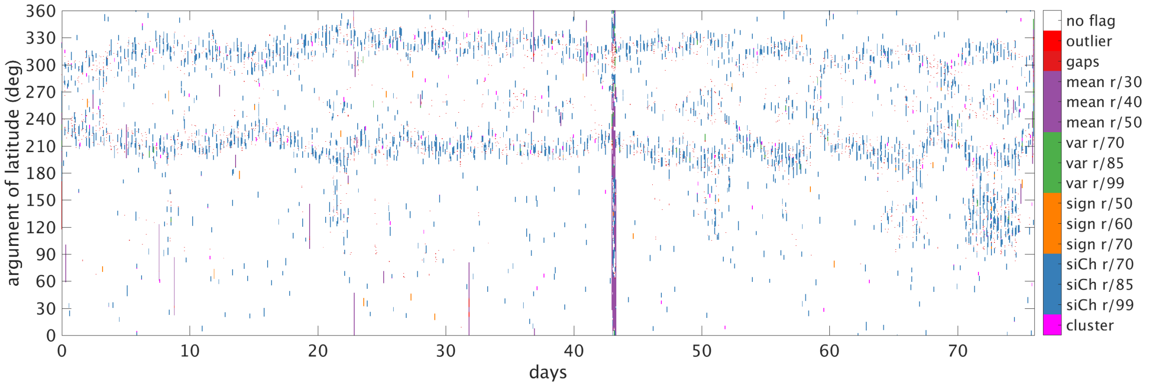

(c) Outliers detected with reduced test sensitivity of the variance test.

Figure 3.5: Thrust level and detected suspicious data in the V_{YY} gravity gradient for the segment 2011/06/08 to 2011/08/23 as an argument of latitude plot. Figure is taken from **Brockmann et al., 2019b**.

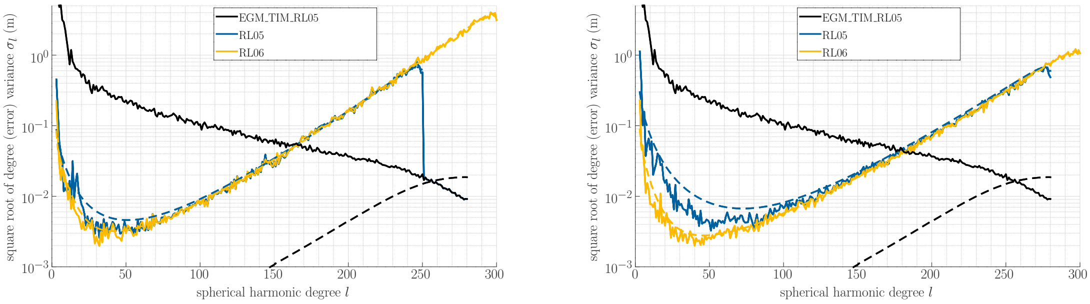

(a) V_{XX} solution for 11/2009–12/2009 segment. (b) V_{XX} solution for 06/2013–07/2013 segment.

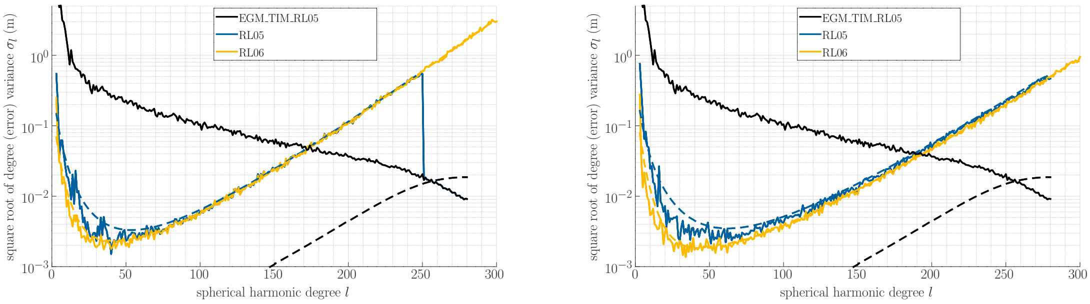

(c) V_{XZ} solution for 11/2009–12/2009 segment. (d) V_{XZ} solution for 06/2013–07/2013 segment.

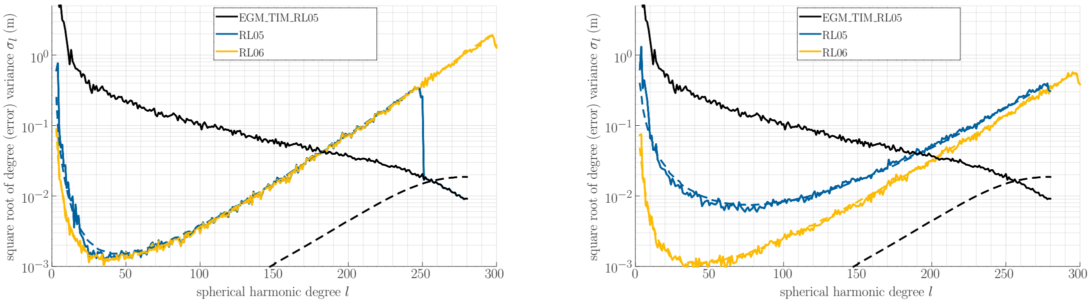

(e) V_{YY} solution for 11/2009–12/2009 segment. (f) V_{YY} solution for 06/2013–07/2013 segment.

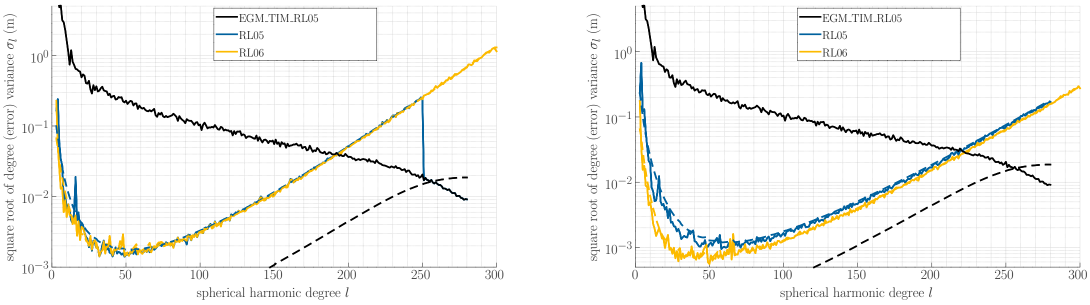

(g) V_{ZZ} solution for 11/2009–12/2009 segment. (h) V_{ZZ} solution for 06/2013–07/2013 segment.

Figure 3.6: Formal (solid lines) and empirical (dashed lines) degree (error) variances of single-component and single-segment solutions for two segments with different characteristics. The time-wise RL05 solution is chosen as reference (black lines), the solutions from RL05 (blue lines) and RL06 (orange lines) are compared. The left column shows a segment very early in the mission with low solar activity where the satellite was operated in a high altitude and thus in a smooth environment (11/2009–12/2009). The second column shows a segment solution towards the end of the mission (06/2013–07/2013), where the orbit was lowered by 30 km and the solar activity was higher. The rows show the results for the different gradient components. Figures are taken from **Brockmann et al., 2021**.

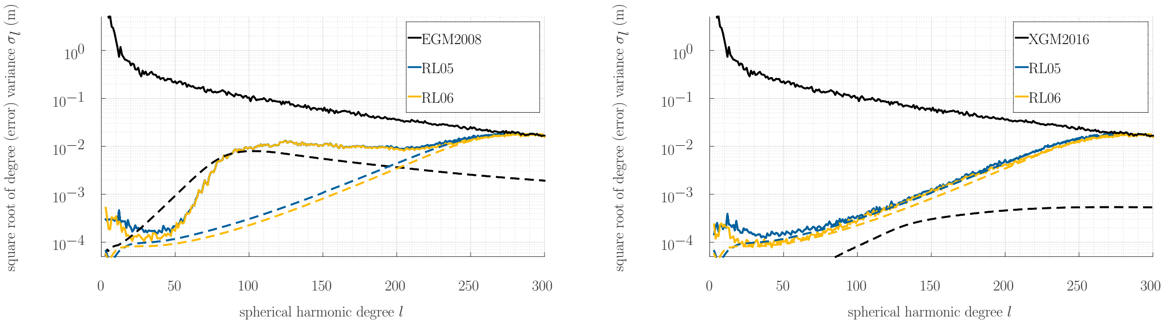

(a) V_{XX} solution for 11/2009–12/2009 segment. (b) V_{XX} solution for 06/2013–07/2013 segment.

Figure 3.7: Formal (solid lines) and empirical (dashed lines) degree (error) variances of RL05 and RL06. Global combination models are chosen as reference (black lines, left EGM2008, right XGM2016), the solutions from RL05 (blue lines) and RL06 (orange lines) are compared.

the heavily affected zonal coefficients are excluded in the computation of the degree error variances.

The left column in Fig. 3.6 shows that there is only a minor improvement in the individual solutions from RL05 to RL06, the blue and orange lines agree quite well. Small improvements are visible for V_{YY} for SH degrees 10 to 20. For V_{XX} and V_{XZ} it becomes visible that the formal error estimates improve. Especially for the SH degrees 10 to 100 the dashed orange line better agrees with the solid orange line (compared to their blue counterparts), therefore it can be concluded that the quality of the covariance matrix of the estimated parameters better reflects the true error characteristics. This becomes important for the combination of i) the different segments and ii) the different gradient components, as it controls the relative weighting. Therefore, it can be expected that the strengths and weaknesses of the individual gradient components are better accounted for in the combination towards the final EGM_TIM_RL06 model.

The right column confirms the improved quality of the formal errors (for V_{XX} and V_{XZ}), but additionally clearly highlights the improvements in the solutions of RL06: Most significantly for V_{YY}, but clearly visible for the other components as well, both formal and empirical errors are reduced for all SH degrees. This shows the improvements in the data and the analysis especially in the challenging environment towards the end of the mission. As the data collected in the lower orbit are very important for the combination due to the increased signal strength, it becomes visible in the combined gradient solutions as well (**Brockmann et al., 2021**).

Performance of RL06 Compared to RL05

Least squares NEQs are derived for the four gravity gradients components V_{XX}, V_{XZ}, V_{YY} and V_{ZZ} for all segments (cf. Fig. 3.2) using the estimated decorrelation filters (cf. Fig. 3.3) and excluding the detected outliers and suspicious data (e.g. cf. Fig. 3.4). The SST NEQs derived from the short arc integral equation approach by colleagues from TU Graz, a Kaula based regularization for the SH degrees above 180, and zero gravity pseudo observations in the polar gap are combined to the final NEQs. To optimally combine different segments of individual gravity gradients, SST and regularization matrices, variance component estimation is applied to estimate relative weights. The final EGM_TIM_RL06 model follows directly from the solution of the combined NEQ system. Further details are discussed in **Brockmann et al., 2021**.

Together with the RL05 model, the resulting RL06 solution is compared in terms of degree variances to state of the art combination models in Fig. 3.7. Here EGM2008 (Pavlis et al., 2012) as a pre GOCE era model and XGM2016 (Pail et al., 2018; Pail et al., 2017), which actually combines the older EGM_TIM_RL05 (Brockmann et al., 2014a), are chosen.

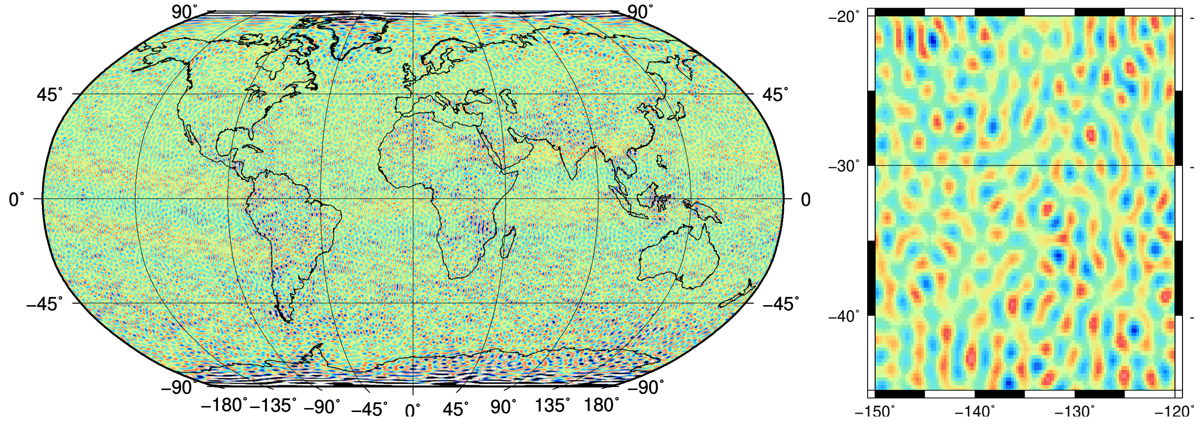

(a) RL05 global. (b) RL05 local.

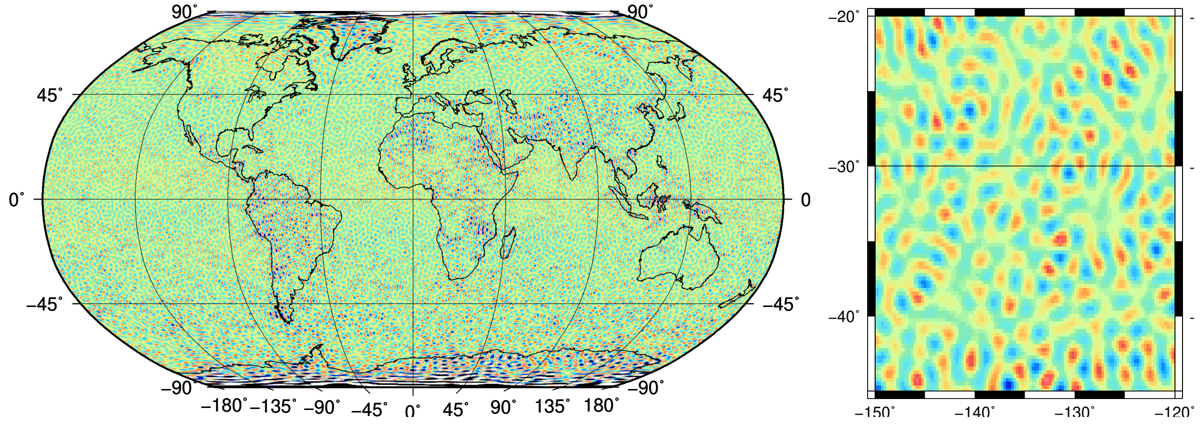

(c) RL06 global. (d) RL06 local.

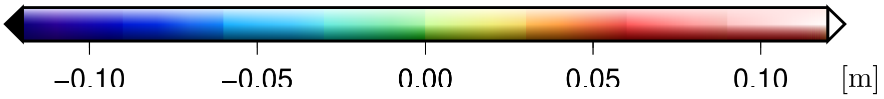

Figure 3.8: Geoid height differences of the RL05 and RL06 model truncated at spherical harmonic degree 200 with respect to the XGM2016 model. Figure is taken from **Brockmann et al., 2021**.

In Fig. 3.7a, EGM2008 is used as reference model which highlights the general benefit of GOCE. The 'bump' visible in the empirical degree error variances between degrees 50 to 200 results from the errors in EGM2008 model. In this region, the model is not a valid reference model — as from the pre GOCE era — the EGM2008 errors dominate the empirical error degree variance estimate. EGM2008 is mainly determined from incomplete and lower quality terrestrial data in that degree range. Below degree 50 EGM2008 is mainly determined by GRACE, so the improvement from RL05 to RL06 starts to become visible. For the degrees above 210, the quality of the terrestrial data starts to dominate GOCE. Independently, the formal error estimates show the improvements and the quality level of the GOCE-only solutions compared to EGM2008.

In Fig. 3.7b, EGM2008 is substituted by XGM2016 to serve as reference. The 'bump' is gone, as XGM2016 incorporates EGM_TIM_RL05 solution as GOCE contribution. Interestingly, although RL05 is used, RL06 is more consistent to the XGM2016 for the lower and higher degrees which shows the quality improvement of the RL06 solution and the positive effect of GRACE and the terrestrial data in XGM2016. For degrees 20 to 90 and 210 to 300 — where XGM2016 is supposed to be more accurate — formal and empirical error degree variances agree well, which demonstrates that the formal error is a realistic measure for the quality of EGM_TIM_RL06. For degree range 90 to 210 XGM2016 can not serve as reference model, as it is limited by the quality of the RL05 contribution.

Finally, RL05 and RL06 models are compared to the XGM2016 model in the spatial domain at the level of geoid heights. For that purpose, the SH series is evaluated for the geoid functional (cf. Eq. (4.4)) truncated at SH degree and order 200 and the difference to the XGM2016 geoid is formed. The results are shown in Fig. 3.8 globally and for a regional area in the South Pacific. Comparing the differences between RL05 from Fig. 3.8a and RL06 from Fig. 3.8c shows on the one hand that the RL06 differences are less noisy. Furthermore some systematic effects are removed, e.g. around the magnetic equator. These kinds of improvements are visible globally.

For a regional analysis, an area in the South Pacific with a smooth MDT is selected (see Fig. 3.8b and Fig. 3.8d). For this region, a high accuracy of XGM2016 is expected, as the included altimetry derived gravity is accurate in those regions. It can be seen that the differences for RL06 are smoother. This is numerically supported by the RMS which is 2.4 cm for RL05 and 2.1 cm for RL06. It is further confirmed by the improvement of the mean formal geoid height error for that region. Error propagation of the covariance matrices of the SH coefficients to the geoid height functional shows that the formal error reduces from 2.7 cm for RL05 to 2.1 cm for RL06.

To conclude, for the RL06 model it is shown that (**Brockmann et al., 2021**):

- The mean global accuracy was improved between 10 % to 25 % compared to RL05.
- The quality of the covariance matrix was increased, yielding a more realistic error description.
- Systematic errors at centimeter level were reduced.

Pessimistically, the accuracy of EGM_TIM_RL06 is 2 cm in terms of geoid and 0.5 mGal in terms of gravity anomalies at the target resolution of GOCE of 100 km. The solution is internationally well accepted and widely used. It is available at ICGEM (ICGEM, 2017), in (**Brockmann et al., 2019d**) and via the ESA GOCE Online Dissemination Service (ESA, 2020) together with its full error covariance matrix as the official ESA time-wise GOCE-only solution.

3.4.2 The GOCO06S Model

With the characteristic that the EGM_TIM_RL06 is a pure GOCE only model and provides a full covariance matrix, which realistically reflects the uncertainties of the model (cf. Sect. 3.4.1), an unconstrained version (i.e. without applying the regularization) is the perfect input of the GOCE data as a sufficient statistic to a combined satellite only model. The GOCO consortium targets to bring together various experts for the different strategies to recover the gravity field from the different missions. As a member of the consortium, significant contributions were made to all existing GOCO models since the first model GOCO01S was released (Pail et al., 2010). In this thesis, focus is on the most recent release, i.e. the GOCO06S global gravity field model (**Kvas et al., 2019b; Kvas et al., 2021**).

Properties of the GOCO Satellite-Only Models

Key idea of the GOCO satellite-only models is to perform the combination on the level of NEQs (e.g. Meissl, 1982, Sect. A.10.2), i.e. the unconstrained least squares NEQs of the individual missions – which exist as standalone models like EGM_TIM_RL06 for GOCE. As existing (unconstrained) least squares NEQs assembled from the observations of the individual missions are setup by the individual mission specific experts the NEQs are inconsistent in their original form. These inconsistencies comprise for instance,

- physical parameters/constants,
- background and/or correction models,
- the reference epoch and/or
- a priori parameters.

These inconsistencies are resolved to best possible extent in a preprocessing step.

Furthermore, the mission specific NEQs are assembled only for a reasonable maximal SH d/o resolvable from the mission and they might contain additional mission specific parameters. As these parameters are not of interest in the context of a combined global gravity field model, they are pre-eliminated from the NEQs. After elimination, the individual NEQ for group n contains the U_n parameters arranged in a parameter sequence $\mathbf{p}_n$. $\mathbf{p}_n$ is a subset of the parameter sequence $\mathbf{p}$ consisting of the U parameters to be estimated for the combined model. Defining the permutation operator $\boldsymbol{\Psi}_{\mathbf{p}_n \mapsto \mathbf{p}}$, reordering the sequence $\mathbf{p}_n$ consistently to $\mathbf{p}$, the NEQs might have to be extended by zero rows and/or columns for the missing parameters for the case $U_n < U$ (for details see Brockmann, 2014, **Brockmann and Schuh, 2016a**).

With that, the combined NEQs read

$$\sum_{n=0}^{N-1} \frac{1}{\sigma_n^2} \boldsymbol{\Psi}_{\mathbf{p}_n \mapsto \mathbf{p}} \left(\begin{bmatrix} \mathbf{N}_n & \mathbf{0}_{U_n \times U-U_n} \\ \mathbf{0}_{U-U_n \times U_n} & \mathbf{0}_{U-U_n \times U-U_n} \end{bmatrix} \right) \tilde{\mathbf{x}} = \sum_{n=0}^{N-1} \frac{1}{\sigma_n^2} \boldsymbol{\Psi}_{\mathbf{p}_n \mapsto \mathbf{p}} \left(\begin{bmatrix} \mathbf{n}_n \\ \mathbf{0}_{U-U_n \times 1} \end{bmatrix} \right), \qquad (3.5)$$

which can be solved for the unknown parameters of the combined gravity field model (SH coefficients and optionally some time dependent SH coefficients). The relative weighting is controlled by the weights $w_n := \frac{1}{\sigma_n^2}$, which can be estimated via VCE (Koch and Kusche, 2002). Typically the higher degree coefficients are regularized for the combination models as well – in (3.5), a regularization matrix is treated as an additional group. E.g. for a Kaula-based regularization for the higher degrees, $\mathbf{p}_n$ contains the higher degree coefficients only, $\mathbf{N}_n$ is a diagonal matrix with inverse degree variances following Kaula's rule on the diagonal and $\mathbf{n}_n$ is a zero right hand side vector.

Primarily, the combination models target the static global gravity field. Therefore, the parameter vector consists of static SH coefficients c_{lm} to s_{lm} up to the maximal d/o determined typically by the GOCE contribution. When combining SLR or GRACE/GRACE-FO derived gravity field models obtained from long time series, these are highly sensitive for temporal changes in the gravity field of the lower degrees. Therefore the reference epoch becomes important. To account for this — although the static model is in focus — the temporal gravity field is coestimated (cf. **Kvas et al., 2021**). In the GOCO series, this is inline with the approach for FE based spatial modeling in Sect. 2.3.4: for the lower degrees, the spatial SHs are combined with a separable temporal function, to model long term temporal varying SH coefficients (especially trends and seasonal amplitudes).

The GOCO06S Model

The satellite-only GOCO06S model is determined from the combination of

- GOCE in form of the unconstrained EGM_TIM_RL06 model,
- GRACE in form of the unconstrained ITSG-Grace2018s model (Kvas et al., 2019a),
- LEO models derived from kinematic orbits of nine satellites (Zehentner and Mayer-Gürr, 2016; Kvas et al., 2019a),
- SLR derived models from ten satellites (**Kvas et al., 2021**) and
- a regularization for the higher degrees and time-variable coefficients (**Kvas et al., 2021**).

Totally, more than 1 160 000 000 observations collected by 19 satellites for a period of 15 years are included. The static model is determined up to the SH d/o 300, which corresponds to the maximal resolution of the EGM_TIM_RL06.

To demonstrate that GOCE is the main contributor for the higher degrees of GOCO06S, Fig. 3.9 shows the degree (error) variances of both models EGM_TIM_RL06 and GOCO06S, using the XGM2016 as reference. Starting from SH degree 100 to 110 there is hardly a difference in the empirical differences between EGM_TIM_RL06 and GOCO06S, which confirms that GOCE is — as expected — dominating the combined solution. Similarly, this is shown for the GRACE solution for the lower degrees in **Kvas et al., 2021**. Furthermore, **Kvas et al., 2021** show a more detailed

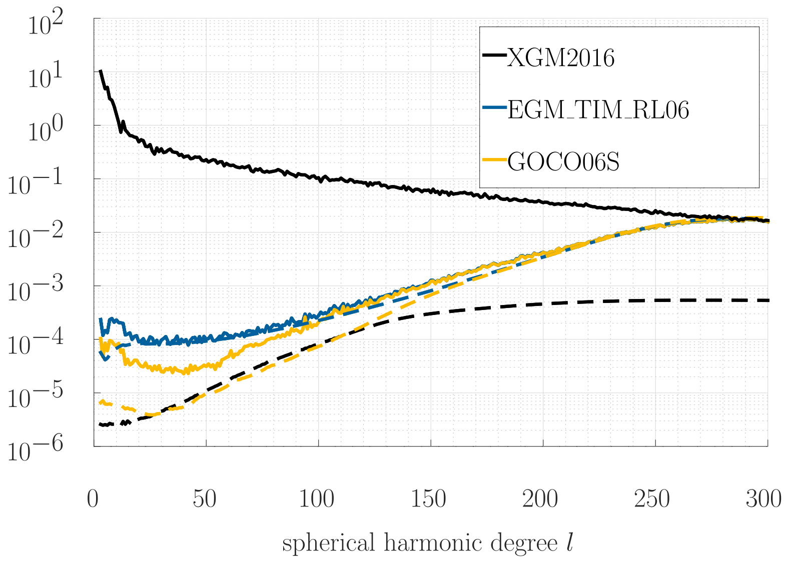

Figure 3.9: Formal (solid lines) and empirical (dashed lines) degree (error) variances of EGM_TIM_RL06 and GOCO06S. A global combination model is chosen as reference (black lines).

contribution study on the level of individual coefficients (for details on the contribution see e.g. Brockmann, 2014, Sect. 5.4).

As for GOCO06S, the handling of the time-variable modeling is mainly developed by the colleagues from TU Graz, details are not discussed here. Basically, the temporal variations provided are set up to d/o 200 and modeled by a trend and seasonal amplitudes. The estimation contains information from observations up to d/o 120 from GRACE and SLR. Within the modeling, instantaneous changes by major earthquakes are considered by co-estimating local step-functions. For a stable estimation, a tailored regularization including a land and ocean map is developed. For further details and a detailed validation of the model refer to **Kvas et al., 2021**.

GOCO06S is one of the internationally most accepted global satellite-only static gravity field models. It serves as a background model for many regional geoid models (e.g. Dilalos and Alexopoulos, 2023), global combination models (e.g. Zingerle et al., 2020), geodetic MDT estimates (e.g. Jousset, 2023) and is used in many other geodetic or geophysical applications (e.g. Li et al., 2023; Peter et al., 2022).

3.4.3 Extended and Updated Models

Combined Gravity Field Models

The satellite-only series (S-series) of the GOCO models do not include all available observations which can be linked to the Earths' gravity field. Primarily, these are terrestrial or airborne gravity measurements over land and gravity anomalies derived from altimetric SSH measurements over the ocean. The satellite-only models of the GOCO series combine individual satellite models, which use realistic covariance modeling. Therefore the covariance matrix of the combined model is expected to be realistic is well. This makes the unconstrained version of the GOCO satellite-only model again a perfect input for a global combination model. The least squares NEQ of the GOCO0*S model is a sufficient statistic of all its input observations, and can therefore be used without loss of information. This is done in **Fecher et al., 2017** to obtain GOCO05c, combining the unconstrained GOCO05S model with full NEQs assembled from altimetry derived gravity products (DTU13 GRA) and terrestrial gravity anomaly data on a $15' \times 15'$ grid. This results in a resolution of SH d/o 720, which makes the assembly and solution computational challenging (Brockmann, 2014; Brockmann et al., 2014b) as the handling of 2 TB matrices is required. Although for a combined model the resolution is not that high, the model was computed by assembling and solving full NEQs, which allows adding inhomogeneous empirically derived weights for the terrestrial data optimizing the relative weighting between the satellite contribution and the additional data. The GOCO05c is published by the GOCO consortium at **Pail et al., 2016** and documented in detail in **Fecher et al., 2017**.

Alternative Polar Gap Regularization

As a GOCE-only model, the EGM_TIM_RL06 model suffers from the polar gap (cf. Sect. 3.4.1). EGM_TIM_RL06 uses pseudo zero gravity field observations in the polar regions, to locally regularize the solution, which yields a poor performance of the model for orbit integration of polar satellites (e.g. Gruber et al., 2011). Therefore, **Zingerle et al., 2019** locally inserted data from the PolarGap campaign, the AntGG project and ArcGP compilation (Forsberg et al., 2007; Scheinert et al., 2016; European Space Agency, 2018) filtered down to the maximal resolution of EGM_TIM_RL06 to derive the polar extended gravity field model TIM_R6e (**Zingerle et al., 2019**). This yields a global GOCE-based model, which agrees to EGM_TIM_RL06 outside the polar regions to large extent, while containing significantly more signal in the polar regions, improving the quality of the model for many applications close to the polar gaps (e.g. orbit integration).

Chapter 4

Parametric Models for the Mean Dynamic Topography

This chapter is based on the work performed in the context of the PARASURV[1] project. Therefore, parts of this chapter are taken in an updated form the proposal, resulting publications, conference contributions and the final project report.

4.1 State of the Art

The difference between the SSH above a reference ellipsoid and the geoid is the dynamic ocean topography (DOT). It reflects many characteristics of the ocean circulation (e.g. Wunsch and Gaposchkin, 1980; Fu, 2014). Although the DOT is subject to temporal variations, the focus is often – as here – on its steady-state part, called the MDT. Its accurate knowledge is important for oceanographers (e.g. Wunsch and Stammer, 1998), as it reveals valuable information about the ocean's circulation and geostrophic surface currents, and geodesists (Rummel, 2001), as it allows for a unification of independent local height systems. The geodetic estimation of the MDT is typically based on the separation of averaged altimetric SSH measurements into the MDT and the geoid. For the separation process, additional independent information about the geoid, the MDT or ideally both is required. When omitting any kind of oceanographic input data (ocean salinity, temperature, pressure observations), instead relying only on satellite derived geoid and SSH data, the resulting MDT estimate is called *geodetic* (e.g. Albertella et al., 2008; Vianna and Menezes, 2010; Woodworth et al., 2015). Being independent of oceanographic data, the MDT is well suited for an assimilation into ocean models (e.g. Janjić et al., 2012; Becker et al., 2012). A remaining scientific issue is the spectral inconsistency of the involved data sets (e.g. Albertella et al., 2008).

Since the 1970s — and since 1993 continuously and globally — the SSH is captured by satellite altimetry with an increasing accuracy. Already Kaula et al., 1970 pointed out that capturing the sea surface with satellites is the only feasible method to observe the entire ocean with high spatial and temporal resolution. The requirements for using altimetric measurements and independent geoid information to determine the MDT as the difference of the (mean) sea surface and the geoid from these measurements were already studied by Greenwood et al., 1969. Since then, several approaches were developed and applied to determine a (geodetic) DOT or MDT from altimetric measurements and geoid information at global or regional scale. Most of them start with the actually computed difference of a gridded MSS (h_{MSS}) data set and a gridded geoid product (N)

$$h_{\mathrm{MDT}} = h_{\mathrm{MSS}} - N. \tag{4.1}$$

Preprocessed MSS products (see Chap. 5) are used instead of the original along-track altimetric SSH measurements. The MSS products are provided as over-sampled fine grids (e.g. $1' \times 1'$) and

---

[1] PArametric determination of the dynamic ocean topography from geoid, altimetric sea surface heights and SAR derived RAdial SURface Velocities (PARASURV). PI J. M. Brockmann. DFG BR 5470/1-1 (2018-2021)

contain averaged SSH of multi mission altimetry collected over decades. See Chap. 5 for further details. The geoid information is typically based on a synthesis of a spherical harmonic model. Consequently, it is band limited and has an accuracy level of 1 cm to 3 cm at a spatial resolution of about 100 km; see Chap. 3 for further details.

Different kinds of filters are applied to homogenize the data sets and account for their spectral inconsistencies. Often, a simple Gaussian low-pass filter is applied to the difference (cf. (4.1)) in the spatial domain (e.g. Bingham et al., 2008; Andersen and Knudsen, 2009; Knudsen et al., 2011; Siegismund, 2013; Farrell et al., 2012) to derive a gridded MDT. Stochastic information on the accuracy of the geoid and the MSS are generally not accounted for. Other filters instead of a Gaussian are chosen for instance in Jayne (2006), Vianna and Menezes (2010), Rio et al. (2011), and Mulet et al. (2021b), either locally adopting the filter or using a collocation like strategy. While the widely used Gaussian smoother is an isotropic filter, Bingham (2010), Bingham et al. (2011), Čunderlík et al. (2013), and Sánchez-Reales et al. (2016) introduce more complex anisotropic filtering methods originally developed for edge extraction in digital images. They are based on the diffusion equations, trying to filter along gradients of the signal, and at the same time avoiding filtering across the gradient. As an alternative to spatial filtering, spectral approaches were introduced (e.g. Tapley et al., 2003; Bingham et al., 2008; Albertella et al., 2012; Gilardoni et al., 2015; Siegismund, 2020). The common basic idea is to expand the altimetric MSS to spherical harmonics up to same d/o of the used gravity field model. They differ mostly in the approaches how the missing MSS information over the continents is synthetically filled. Afterwards, the differences are computed in the same spectral domain to derive an MDT. The methods mentioned so far operate on a spatially predefined grid and use gridded and temporally averaged altimetric data instead of the original along-track SSH measurement profiles. Bosch and Savcenko (2010) avoid using gridded products, but use the altimetric measurements along the original tracks. They combine the spatial and spectral strategies to filter the gravity field model in the spectral domain and the altimetric SSHs along the satellite ground track in the spatial domain. Thus, not an MDT but a DOT along the satellite track is derived (e.g. per cycle).

Information about the MDT can also be derived from other data sources, like in-situ hydrographic measurements or surface velocity observations (e.g. Maximenko et al., 2009). This information can be used to refine the spatial resolution of geodetic MDT models. Maximenko et al. (2009) used near-surface drifter and wind data in combination with a geodetic MDT estimate to derive an improved MDT. Rio and Hernandez (2004), Rio et al. (2007), Rio et al. (2011), Rio et al. (2014), and Mulet et al. (2021b) determined their MDT from a gravity field model, an MSS, drifting buoy velocities and hydrographic profile measurements. As the data sets are analyzed on grids, the finally derived MDT models are determined by weighted averages. These combinations provide smooth, high resolution and high quality MDT models. But, the used additional data i) has an imperfect spatial and temporal distribution (Roemmich et al., 2003; Lumpkin and Pazos, 2007) and ii) is often used to force ocean models or are even assimilated into these (e.g. Stewart, 2008). Due to the latter, an MDT including the hydrographic profiles should not be assimilated into an ocean model, as such data would enter the model twice.

An observation type which is so far not used for MDT determination are SAR derived RSV (e.g. Gonzalez et al., 1981; Chapron et al., 2005; Shutler et al., 2016). To derive the RSV, two approaches can be distinguished (cf. Romeiser et al., 2010). Firstly the along-track interferometry and secondly the evaluation of the so called Doppler Centroid Anomaly (DCA). The latter is from a theoretical point of view applicable to all SAR satellites, also to historical data. Therefore, the focus is on the DCA method (Chapron et al., 2005; Romeiser et al., 2010). Due to relative motion between the surface and the satellite, a Doppler shift occurs (cf. Madsen, 1989). Reducing the shift resulting from the satellites movement and the Earth's rotation, the remaining part is the DCA. Over the ocean it is related to the movement of the ocean surface, which is caused mainly by the ocean currents and the wind (Hansen et al., 2011). Reducing the wind and sea state contributions (Mouche et al., 2012; Moiseev et al., 2020b) and the ageostrophic part (e.g. Ekman currents, cf.

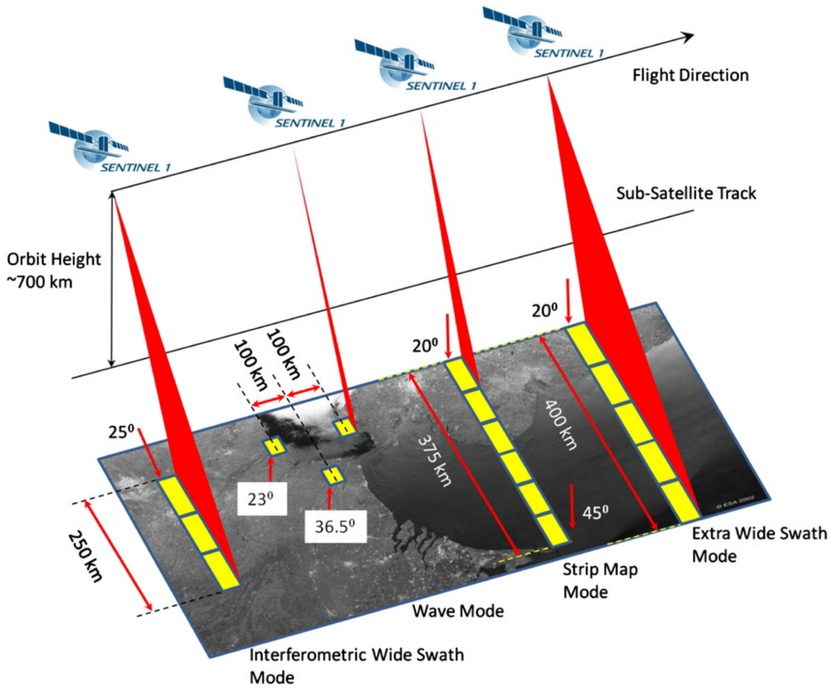

Figure 4.1: Sentinel-1 acquisition modes. Figure taken from Sentinel-1-Team, 2013.

Rio et al. (2011)), the radial part of the geostrophic current is obtained (i.e. the projection in radial direction towards the satellite). As shown by Johannessen et al. (2008), Johannessen et al. (2014), Moiseev et al. (2020a), and Moiseev et al. (2022) realistic surface currents can be derived from multiple SAR images, e.g. for the Greater Agulhas Current from ENVISAT or data from the Sentinel-1 mission.

This observation type and the DCA method are of special interest, as a level 2 ocean data product (DCA and the derived RSV) exists for the Sentinel-1 mission of the European Commissions' Copernicus program (CLS, 2016; Engen and Johnsen, 2010; Moiseev et al., 2020b; Moiseev et al., 2022). RSV are provided for two of the Sentinel-1 acquisition modes (cf. Fig. 4.1). The first is the wave (WV) mode, which is the default mode for the open ocean, for which RSV is derived with a 100 km sampling in a kind of zigzag pattern along the orbit. In selected, mainly coastal regions of interest, data from the high resolution interferometric wide swath (IW) mode are available. There RSV observations are available in 3 sub swaths with total coverage of 200 km to 250 km with one value per 1 km pixel.

4.2 Objectives and Contributions

Following the discussion from above, altimetric SSH as well as satellite based observations which can be linked to the geoid are the most important input datasets for geodetic MDT estimation. As the SSH contains amongst the temporal SLA the sum of both – MDT plus geoid – this is a typical signal separation problem. To solve this, either the geoid has to be known or complementary observations, which are sensitive to the geoid (or the MDT), must be available. The available geoid information over the ocean – which is independent from satellite altimetry – results from the dedicated gravity field missions (see Chap. 3 for the details), with a limited spatial resolution and a limited accuracy. The spatial resolution is significantly lower compared to the along-track altimetry resulting in spectrally inconsistent datasets. Adding assumptions on the resolution and smoothness of the MDT results in a solvable problem with the potential to improve the geoid model with the SSH measurements in a joint analysis.

In order

(i) to use the original along track SSH measurements as a stochastic data set,
(ii) to flexibly set up and extend the observation equations for altimetric SSH,
(iii) to integrate the geoid information as a stochastic data set,
(iv) to coestimate a geoid improved by the SSH measurements,
(v) to optionally integrate observations of surface currents (e.g. drifters or RSV) to support the separation, and
(vi) to derive uncertainty measures of the MDT and geoid estimates

a parametric approach is proposed (cf. Sect. 4.3).

Starting with **Becker et al., 2014b** and **Becker et al., 2014a** and extended in **Brockmann et al., 2023** and **Neyers and Brockmann, 2024** a procedure to solve the signal separation task to estimate a parametric MDT model from along-track altimetric SSH measurements, satellite-based geoid information and optionally surface current information is *designed*, *implemented* and *established*. Most of the recent work has been realized in the context of the PARASURV project funded by DFG.

Basic idea of the parametric approach is to jointly estimate both – the geoid as well as the MDT from complementary observations treating these as realizations of random variables. For that reason, a deterministic function g_{MDT}, which models the MDT must be established. Whereas spherical harmonics are well established for the geoid (cf. Sect. 1.2 and (4.4)), there exists no closed expression for the MDT derived from physical laws. In this case, the unknown function g_{MDT} has to be approximated. As discussed in Section 2.3, FESs are used and adopted for the representation of the MDT with different smoothness characteristics and requirements for the spatial resolution. Whereas C^0-smooth FEs are widely used due to their relatively simple structure, C^1-smooth elements are a good choice for the MDT as the steady-state ocean currents are proportional to the spatial gradient of the MDT. Consequently, special emphasis is on elements which guarantee a C^1-smooth function g_{MDT}. A generic implementation is realized within the PARASURV project such that all FEs implemented (cf. Sect. 2.3) are usable for the parameterization of the MDT.

As both target reference surfaces — the MDT as well as the geoid — are parametric continuous functions, the parameters for both can be estimated in an adjustment procedure from the available observations sensitive to at least one of the two surfaces. Using the least squares principle, the combination of different observation types is straight forward. On the one hand, geoid information can be easily added in the SH domain (e.g. the gravity field models as derived in Chap. 3) as sufficient statistics of the original observations without loss of information.

Any kind of observations, sensitive either to the MDT, the geoid or both can be included as soon as the observation equations are derived. For instance, due to the parametric representation of the MDT, it becomes possible to introduce (preprocessed) surface current observations in geostrophic approximation as in-situ measurements, as the derivative of the MDT is continuously defined. This enables to study the use of the SAR derived RSV for MDT determination. Theoretically, as RSV can be derived from any SAR satellite – a global dense coverage might become available in future. Although not the complete surface current signal is observed — only the one-dimensional projection in line-of-sight (LOS) direction, observation equations can be derived for the parametric approach using C^1-smooth FE. This poses a major challenge for the established grid-based MDT approaches discussed above.

Using the stochastic view on the adjustment task allows for a proper modeling of the uncertainties of the observations, applying one of the covariance modeling approaches as discussed in Sect. 2.2. This allows for – from a theoretical point of view – an optimal combination of the observations. The parameterization enables to use the original observations, which are for instance the original 1 Hz sampled SSH observations along the track of the altimeter satellite. This gives the opportunity to coestimate temporal SLA signals, or in the future other geophysical signals of interest like ocean tides.

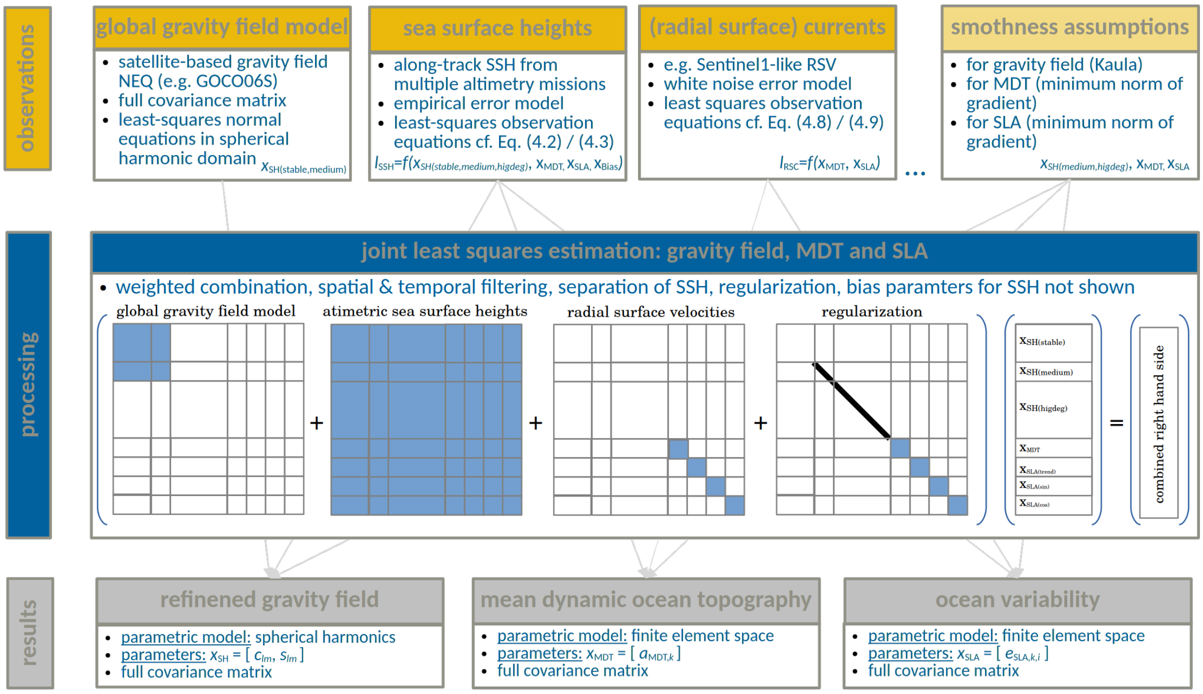

Figure 4.2: Schematic overview of the proposed procedure, summarizing the used observations, their sensitivity to the estimated parameter groups, a sketch of the combined least-squares normal equations system, as well es the estimated parameters (slightly modified from **Neyers and Brockmann, 2024**).

Due to the high sampling rate, a long observation period and the large number of unknown parameters (mainly due to the SH for the geoid), a tailored implementation is realized in an HPC environment to solve the adjustment problem (cf. Sect. 2.4). Although working regional, the estimated global SHs used to model the geoid are regionally updated. It can be shown that the estimated regional geoid update is meaningful (**Brockmann et al., 2023; Neyers et al., 2022c**).

4.3 Summary of the Parametric Approach

The proposed parametric approach is summarized by the schematic sketch in Fig. 4.2. It shows the used observations, their sensitivity to the estimated parameters, the structure of the joint least-squares estimation strategy and the resulting estimated parameters.

4.3.1 SSH Observation Equations

Key input for the estimation of a geodetic MDT are the altimetric SSH observations as taken by the numerous altimeter missions. Using the relation (1.3), the i-th SSH observation $\mathcal{L}_i$ collected by the satellite mission j at the location (λ_i, ϕ_i) in ellipsoidal coordinates taken at time t_i can be symbolically written as (cf. **Brockmann et al., 2023**)

$$\mathcal{L}_i = N(\lambda_i, \phi_i) + g_{\text{MDT}}(\lambda_i, \phi_i) + f_{\text{SLA}}(\lambda_i, \phi_i, t_i) + o_j + \mathcal{E}_i. \tag{4.2}$$

Here, $\mathcal{E}_i$ represents the random measurement error and o_j a mission specific bias. This assumes the observations have been successfully and perfectly corrected for environmental conditions (c), like instrument and sea state bias, atmospheric, tidal and inverted barometer corrections (for details see Aviso, 2020). Residual signals of these effects are implicitly assumed to be random and thus modeled by $\mathcal{E}_i$, for which $E\{\mathcal{E}\} = 0$ is assumed.

The observation equation (4.2) can be even simplified, assuming that due to repeated measurements at the same location f_{SLA} vanishes for the observation period, yielding

$$\mathcal{L}_i = N(\lambda_i, \phi_i) + g_{\mathrm{MDT}}(\lambda_i, \phi_i) + o_j + \mathcal{E}_i \tag{4.3}$$

as observation equations. Eq. (4.3) assumes that the least-squares adjustment implicitly takes care of the temporal averaging. This is a quite realistic assumption for SSH measurements from ERMs, which re-visit the same orbit every 10 days to 30 days, depending on the actual mission, it might be problematic when GMs are used, which have either no repeat, or a repeat cycle above one year. Consequently, in cases the SLA is neither reduced in advance nor coestimated, aliasing might occur, depending on the implicit spatio-temporal filtering.

4.3.2 Modeling the Geoid

Although not optimal when working regional, i.e. just targeting regional MDT estimates, spherical harmonics are used for the gravity field and the geoid (**Becker et al., 2014b; Becker et al., 2014a; Neyers and Brockmann, 2024**). This has the advantage that the satellite-based gravity field models can be directly used as stochastic data sets and ill-posed transformations to grids/local basis functions can be avoided (see e.g. Klees et al., 2018; Klees et al., 2019).

Therefore, the complementary geoid information can be directly used in the adjustment in the spherical harmonic domain. Unconstrained normal equations, as for instance assembled for the gravity field missions in Chap. 3, can be directly included in the adjustment using the addition theorem for normal equations (e.g. Meissl, 1982, A.10.2).

Due to the along-track sampling of the altimetric SSH of about 7 km to 8 km, the use of GMs with an across-track spacing down to 7 km to 8 km and the assumption that the MDT signal is smooth, the marine geoid can be resolved to very high d/o. To avoid aliasing of geoid signals to the MDT, the maximum degree of SH expansion must be higher than the resolution of the exiting satellite only information which are available to degree 300 (cf. Sect. 3). Accounting for the fact that the accuracy of the satellite-based geoid information is limited and has the required cm-level around degree 200, i.e. about 100 km (**Brockmann et al., 2021**), the geoid is modeled in the most recent studies up to d/o 600 (**Brockmann et al., 2023; Neyers and Brockmann, 2024**). This corresponds to more than 360 000 unknown spherical harmonic parameters c_{lm} and s_{lm}. The SH coefficients can be clustered into three groups:

SH stable:	These are the low degree coefficients, which are accurately determined by the global satellite-based model. Roughly, it includes the coefficients from degree 2 to 200. It is expected that these are not significantly updated in the combined estimation by including the additional SSH observations.
SH medium:	These are the coefficients which are included in the satellite based model, but are not accurately determined. In the scenario mentioned above, these are coefficients for SH degrees 201 to 300. It is expected that in the combined estimation they benefit from both, the global model information as well as the SSH observation.
SH higdeg:	These are the high degree coefficients, formulated in SSH observation equations, but not included in the global model. In the examples, these are the coefficients from degree 301 to 600. Despite some correlations, they are determined from SSH data (and regularization) only.

Geoid signals above d/o 600 remain unmodeled in (4.2) and (4.3). Therefore it is either required to reduce these omitted signals from the SSH observations in advance using global high resolution gravity field models defined above d/o 600, or to model these signals as part of the stochastic model. Assuming a proper choice for the function $g_{\mathrm{MDT}}(\cdot)$ with a tailored spatial resolution and spatial filtering characteristics, the random variable $\mathcal{E}_i$ can be used to model the high resolution geoid signal as part of the error model. This requires to account for the characteristics of the unmodeled geoid signal in the covariance matrix of the observations $\mathbf{\Sigma}_{\mathcal{L},\mathcal{L}}$ as an ommission error (for further details see **Schuh et al., 2015**).

Starting with the SH representation of the disturbing potential (cf. (3.2) together with (3.1)), the geoid can be approximated in the SH domain (e.g. Hofmann-Wellenhof and Moritz, 2005) and represented as a function in ellipsoidal coordinates ($h = 0,\ \lambda,\ \phi$)

$$N(\lambda, \phi) = T(r\,(0, \lambda, \phi)\,,\ \lambda,\ \varphi\,(0, \lambda, \phi))\,/\gamma(\phi), \tag{4.4}$$

where $\gamma(\cdot)$ is the normal gravity and ($r,\ \lambda,\ \varphi$) the representation of the location in spherical coordinates. With that, the geoid can be easily substituted in (4.2) or (4.3), which leads to a linear function in the unknown parameters c_{lm} and s_{lm}, arranged in a parameter vector $\mathbf{x}_{\text{SH}}$ (see Fig. 4.2). To complete the least-squares observation equations, a FES to model the MDT according to (2.31), and optionally for the SLA according to (2.35) are required.

4.3.3 Finite Element Spaces for the MDT and the SLA

As already discussed and shown in Sect. 2.3.3, the Argyris element is well suited for the approximation of the MDT. As within more recent studies, observations of surface currents which are linked to the gradient of the MDT are considered, C^1-smoothness is required (cf. Sect. 4.3.4). With the FE selected, the spatial resolution – or the filtering effect – fully depends on the selected mesh. Although it is challenging to provide a measure for the spatial resolution of the FESs, it can be approximated by

$$r = \frac{\Delta e}{n_{\text{DOF}}} \tag{4.5}$$

where Δe is the average length of edges of the triangulation, and n_{DOF} are the DOF. For the Argyris element, defined by the two-dimensional polynomial of degree 5, all slices across the triangle are one-dimensional polynomials of degree 5 with six DOF. Due to the C^1-smoothness, the DOF are reduced by 2, thus $n_{\text{DOF}} = 4$. Within various studies, it was found that a triangulation with an edge length of about 250 km yields good results. E.g. the signal from the MDT_CNES_CLS18 can be approximated with an RMS of 4 mm (cf. Tab. 2.2a). The spatial resolution of about 62.5 km is in the order where the geostrophic approximation holds, which is depending on the study and region between 50 km to 100 km (Vergara et al., 2023; Yu et al., 2021; Qiu et al., 2018).

Thus, after the choice of the element and the generation of a triangulation (cf. Sect. 2.3.2) the function g_{MDT} representing the MDT follows from (2.31) and yields, substituted to either (4.2) or (4.3), linear observation equations in the unknown parameters $a_{\text{MDT},i}$, arranged in the parameter vector $\mathbf{x}_{\text{MDT}}$ in Fig. 4.2.

For the case the SLA is coestimated, a spatio-temporal model assuming separable functions for the spatial and temporal domain according to Sect. 2.3.4 is used. For the spatial function, exactly the same FE and the same mesh as used for the MDT are selected. Inserting (2.35) in the linear OEQs from (4.2) the additional unknown parameters $e_{\text{SLA},i,j}$ (grouped in the parameter vector $\mathbf{x}_{\text{SLA}}$ in Fig. 4.2) have to be estimated. More details about the specific scenarios analyzed, especially for the temporal model component, are discussed in Sect. 4.4.1.

4.3.4 Observation Equations for Current Data

Within the parametric framework, it is straightforward to link the geostrophic currents to the MDT in an analytical way (for details see **Neyers and Brockmann, 2024**). The vector valued function for the geostrophic currents $\mathbf{u}(\lambda, \phi)$ with the north-south velocity component u and the east-west velocity component v follows from the continuous representation of the MDT via (e.g. Stewart, 2008, eq. (10.10))

$$\mathbf{u}(\lambda, \phi) = \begin{bmatrix} u(\lambda, \phi) \\ v(\lambda, \phi) \end{bmatrix} = \frac{g}{f_c}\mathbf{R}\nabla g_{\mathrm{MDT}}(\lambda, \phi) \tag{4.6}$$

where g is gravity and f_c the Coriolis frequency. $\mathbf{R}$ is the rotation matrix which rotates by 90° clockwise, i.e. the currents are orthogonal to the gradient $\nabla g_{\mathrm{MDT}}(\lambda, \phi)$. Whereas (4.6) can be directly used as least-squares observation equation for drifter derived geostrophic surface current observations, a projection to the radar LOS unit vector $\mathbf{r}_i$ is required for RSV observations, i.e.

$$\mathcal{L}_i = \left\langle \frac{g}{f_c}\mathbf{R}\nabla g_{\mathrm{MDT}}(\lambda_i, \phi_i), \mathbf{r}_i \right\rangle + \mathcal{E}_i. \tag{4.7}$$

Furthermore, the SLA can be accounted for in (4.6) or (4.7) as well, assuming that the instantaneous current/velocity measurement is affected by SLA as well, which is then for RSVs

$$\mathcal{L}_i = \left\langle \frac{g}{f_c}\mathbf{R}\nabla \left(g_{\mathrm{MDT}} + f_{\mathrm{SLA}}\right)(\lambda_i, \phi_i, t_i), \mathbf{r}_i \right\rangle + \mathcal{E}_i. \tag{4.8}$$

Depending on the analysis, either (4.7) or (4.8) is used as linear-observation equations, relating the RSV measurements to the MDT parameters $a_{\mathrm{MDT},i}$. These observation equations assume that i) the observations are reduced to the geostrophic part, or ii) the ageostrophic signal cancels by the averaging procedure or iii) is absorbed by the spatio-temporal model for the SLA.

4.3.5 Using the Global Geoid Observations

As the geoid is modeled in the SH domain, preprocessed normal equations of global gravity field models can be directly used instead of raw observations in the adjustment. They are not available for the entire SH domain, but only for the degrees attributed to 'SH stable' and (by definition) for the coefficients attributed to 'SH medium'. Using unconstrained satellite-only normal equations, e.g. derived from GRACE or GOCE or combined models like GOCO (cf. Sect. 3), guarantees that the included geoid information is independent from the altimetric SSH.

4.3.6 Joint Estimation Procedure

Combined Least-Squares Estimation

As the SSH and RSV observations are independent, least-squares normal equations can be computed for the different observations groups, i.e. SSH and RSV, separately and only for the subset of the parameter space they are sensitive for. For each group g, the normal equation matrix $\mathbf{N}_g$ and the right hand side vector $\mathbf{n}_g$ follow from (2.7) and result in (2.11), using one of the stochastic model representations discussed in Sect. 2.2. For instance, in **Brockmann and Schuh, 2016b; Brockmann et al., 2016** the use of covariance functions derived from estimated AR processes is studied for the SSH. As the influence on the estimated parameters is shown to be small, especially in simulation studies, a white noise model is applied to reduce the numerical complexity and to save computational resources (**Brockmann et al., 2023; Neyers and Brockmann, 2024**). As the global gravity field information is already available in form of normal equations, the combination can be directly done based on the addition theorem of normal equations (see Meissl, 1982, A.10.2). The structure of the resulting normal equation due to the different sensitivity of the observations is depicted in the second row of Fig. 4.2 ('processing'). Reordering strategies are required to combine the normal equations in a consistent way (see **Brockmann and Schuh, 2016a**). This is a challenging task, especially in an HPC environment, where the large matrices are stored distributed along many processes.

This combination strategy easily allows the inclusion of additional data sets, sensitive to the gravity field, the MDT or both (e.g. drifter derived surface currents). A relative weighting scheme is introduced by iteratively determining weights using VCE (Koch and Kusche, 2002).

The normal equations resulting from the combination of the observation based groups are ill-posed, especially as the SH have global support, while only regional SSH observations are used. Furthermore, the rank deficiency due to the linear dependence of MDT, SLA and geoid in the SSH observation equations, is only resolved in case the global geoid information has a sufficient spatial resolution. This is supported by smoothness conditions introduced to the parameter by means of regularization.

Regularization

Without discussing this in too much detail here, it is important to state that regularization is required to i) obtain solvable normal equations and to ii) obtain smooth estimates for the MDT (and SLA). The Kaula rule is used to determine degree dependent weights of a diagonal regularization matrix for the SH coefficients SH medium and SH higdeg. The coefficients are regularized towards zero, using a small weight to make all coefficients estimable.

The separation of the SSH only works for the long wavelengths, for which the geoid is accurately determinable from the global satellite based geoid information. To support the separation, the assumption of a smooth MDT is added. The least-squares objective function is extended for the minimization of the squared L^2-norm of the gradient of the MDT, $\|\nabla g_{\mathrm{MDT}}\|$, which yields a regularization matrix similar to the stiffness matrix known from the classical FEM via analytical or quadrature-based integration. For this, numerical quadrature using the control points and weights from Taylor et al., 2005 are used. The regularization, in case SLAs are estimated as well, is setup in the same way. Corresponding regularization matrices are sketched as a joint regularization matrix in Fig. 4.2.

Solving the weighted combined normal equations yields the least-squares parameter estimates for the gravity field ($\mathbf{x}_{\mathrm{SH}}$), the MDT ($\mathbf{x}_{\mathrm{MDT}}$) as well as the ocean variability ($\mathbf{x}_{\mathrm{SLA}}$), in case it is coestimated (cf. third row in Fig. 4.2, 'results'). The full covariance matrix of the parameters can be derived as well. Using the estimated parameters, geoid, MDT, SLA, and surface currents can be directly derived on arbitrary grids by evaluating the corresponding continuous functions using the estimated parameters (cf. e.g. (4.4), (2.31), (2.35) or (4.6)).

4.4 Selected Results

4.4.1 Coestimating SLAs

The presented approach is applied in **Brockmann et al., 2023** to estimate the geoid and MDT from SSH observations and the unconstrained GOCO06s model as geoid information. The real data study introduces the coestimation of the SLA, using global basis functions for the temporal model, consisting of a trend and an annual oscillation (cf. (2.33), but excluding the constant mean function 1). Both, (4.3) and (4.2) are used as observation equations for the SSH. Via a comparison of the resulting geoid and MDT estimates, the benefits of the coestimation are studied. Furthermore, the estimated SLA signal is verified via a comparison to a published SLA product.

To quantify the effect of coestimating the SSH 10 years of altimetric SSH observations (01/2010 until 12/2019) from ERMs (Jason-1, Jason-2 and Jason-3) and GMs (Cryosat1, GM phases from the Jasons') are combined with the unconstrained GOCO06s model. Regularization for the gravity field and the MDT (and when coestimated for the SLA) is applied.

Fig. 4.3 shows the results for a regional MDT estimate in the Agulhas region (with and without coestimation of SLA) as a difference to the MDT_CNES_CLS18 model[2] (Mulet et al., 2021b) as

---

[2] A correction due to difference in the reference epoch is accounted for.

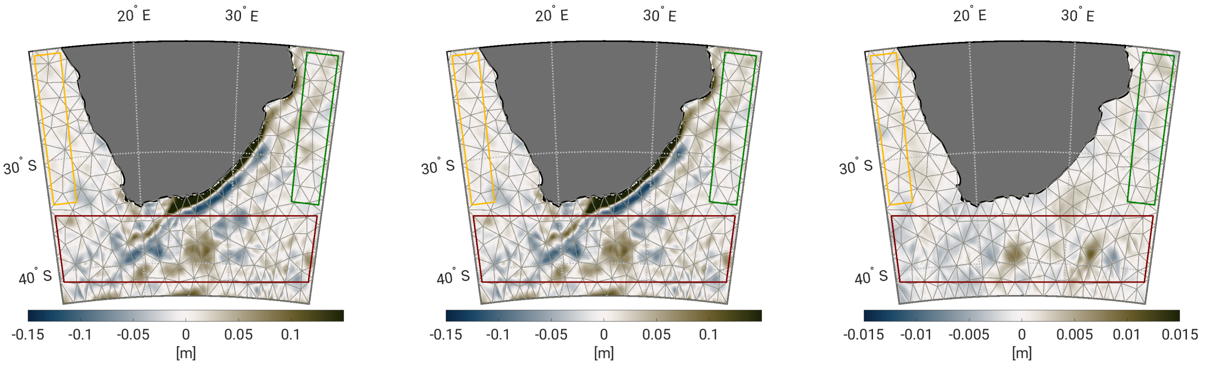

(a) No SLA − Reference.

(b) SLA − Reference.

(c) SLA − no SLA.

Figure 4.3: Difference of the estimated models to the reference model MDT_CNES_CLS18 (a: without coestimation of SLA, b: with coestimation of SLA) and between both estimated MDTs (c). Figure taken from **Brockmann et al., 2023**.

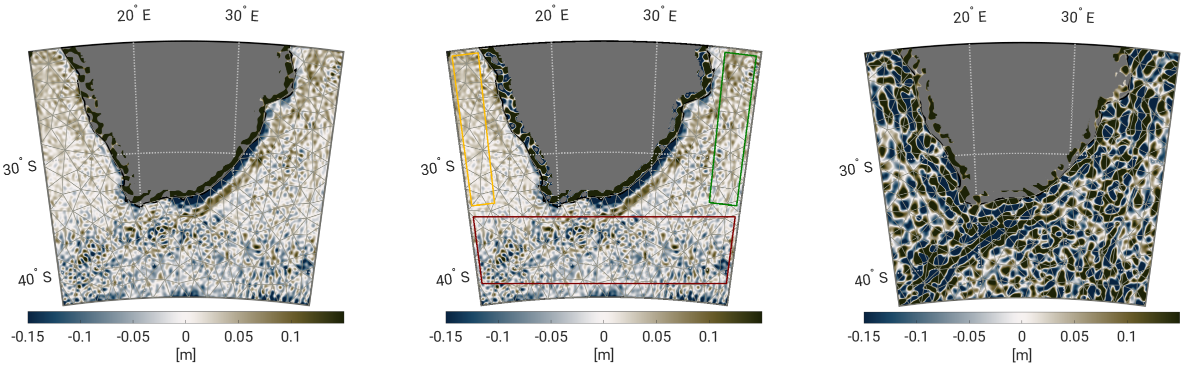

(a) No SLA − XGM(l=600).

(b) SLA − XGM(l=600).

(c) GOCO06s(l=250) − XGM(l=600).

Figure 4.4: Difference of the estimated geoid compared to the XGM2019 model at degree 600 (a: scenario without coestimation of SLA, b: scenario with coestimation of SLA) and between the used geoid model GOCO06s at degree 250. Figure taken from **Brockmann et al., 2023**.

well as the difference between the two estimates. For the comparison, the FE based models are evaluated on the grid as defined by MDT_CNES_CLS18, evaluating (2.31) with the estimated MDT parameters. As confirmed by Fig. 4.3c, the differences between both solutions (Fig. 4.3a vs. Fig. 4.3b) are only minor (RMS below 2 mm, maximal/minimal difference below ±1 cm). This means that the coestimation of the SLA hardly influences the MDT and the spatiotemporal filtering effect of the chosen FES is sufficient to avoid aliasing.

The same is observed when comparing the estimated geoid (cf. Fig. 4.4). Both differences to the XGM2019 model evaluated up to degree 600, used as reference, look very similar. No significant difference is visible when comparing Fig. 4.4a and Fig. 4.4b. Again, it has to be concluded that the coestimation does not improve the estimated geoid. But, comparing the used geoid signal from GOCO06s at degree 250 to the XGM2019 at degree 600 (cf. Fig. 4.4c), it can be seen that the difference is significantly reduced for the estimated geoid (cf. Fig. 4.4a or Fig. 4.4b). It can be concluded that the estimated geoid is improved between degree 300 and 600 by meaningful geoid signal, which is successfully extracted from the SSH observations.

There are regions where the separation does not succeed: A large difference is visible in the

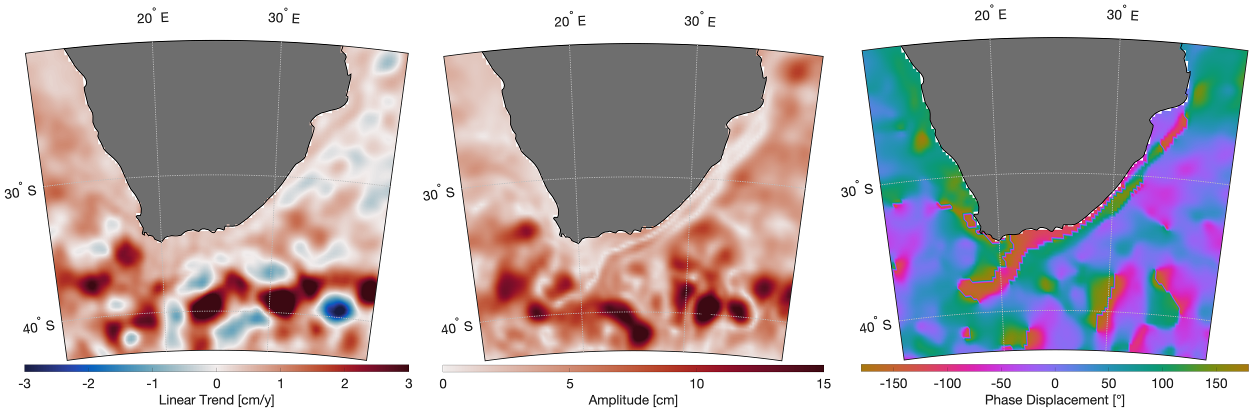

(a) Trend DUACS. (b) Amplitude DUACS. (c) Phase DUACS.

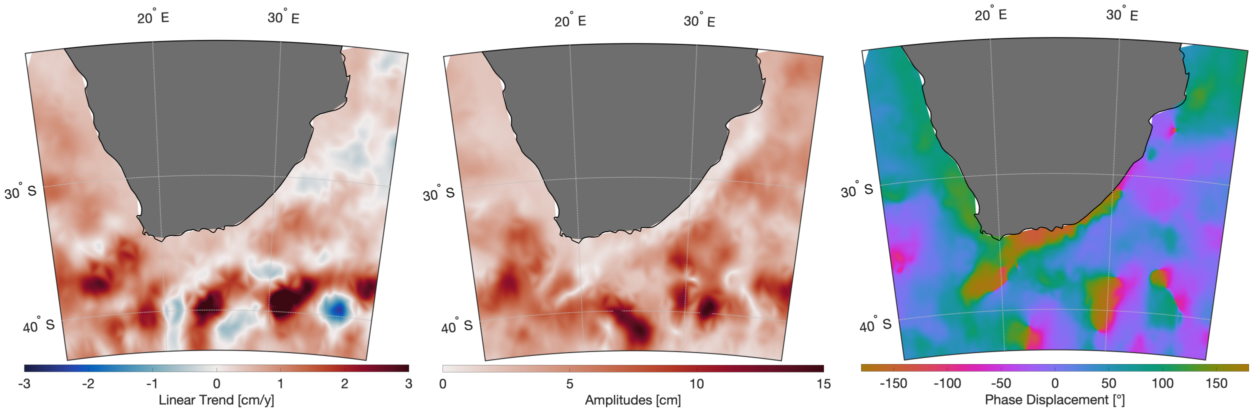

(d) Trend coestimated. (e) Amplitude coestimated. (f) Phase coestimated.

Figure 4.5: Spatial map of the estimated SLA trends (first column), annual amplitudes (second column) and phases (third column) estimated from the gridded DUACS SLA product (first row) and derived from the coestimated SLA (second row). Figures are taken from **Brockmann et al., 2023**.

MDT difference in the coastal area (cf. Fig. 4.3a), which shows up with the inverse sign in the geoid difference (cf. Fig. 4.4a). Due to the applied MDT regularization, i.e. minimizing the norm of the gradient, the strong coastal gradient (part of the Agulhas current) is not captured in the MDT estimate but wrongly attributed as geoid signal. Those kind of errors are supposed to be reduced including observations sensitive to the MDT only, such as RSV or surfaces currents (see Sect. 4.4.2 and 4.4.3).

Although neither beneficial for MDT nor for the geoid estimate, Fig. 4.5 shows the estimated SLA signal characteristics compared to an existing gridded SLA data set (daily DUACS Level 4 gridded SLA DT2018, Taburet et al., 2019). Amplitude, phase and trend can be directly computed from the estimated SLA coefficients (via an interpolation with the spatial FE basis functions), the quantities (annual amplitude and trend) for the reference data set are estimated individually per grid cell in a linear adjustment. Fig. 4.5 clearly shows the similarity for trend, amplitude and phase, which demonstrates that the coestimation works and estimates the expected signals.

To understand the reason why the coestimation does not improve the MDT and geoid results, Fig. 4.6 shows the time series of the SLA reference product for two single locations. Whereas Fig. 4.6a shows a location with a low ocean variability, Fig. 4.6b shows a location in the Agulhas current system with a strong temporal variability of the ocean. Shown are both, the daily values from the gridded reference product, and the coestimated time-series evaluated from the estimated parameters for the same location, cf. (2.37). In the region of low-variability (variation is $\pm 0.05\,\mathrm{m}$, orange) the time-series is dominated by the annual signal and the trend. In this region, the used

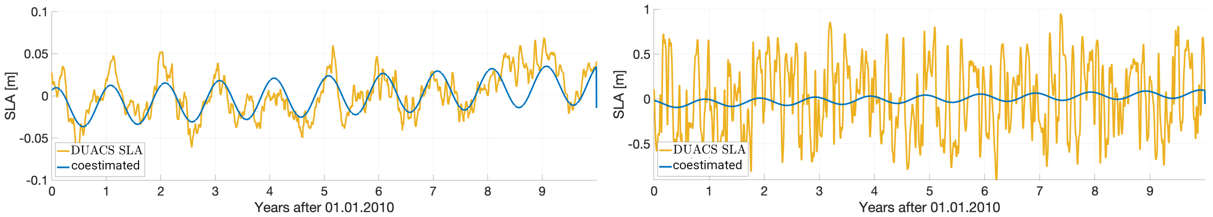

(a) Location with low ocean variability (13.375 ° E, 20.875 ° S).

(b) Location with strong ocean variability (17.325 ° E, 39.125 ° S).

Figure 4.6: SLA time series from the DUACS product (orange) for two grid points compared to the functions coestimated (blue). Figures are taken from **Brockmann et al., 2023**.

model function captures the signal quite well (blue). But, in the regions of strong variations, the signal is ten times higher (±0.5 m, orange) and shows significantly higher frequency characteristics. These strong variations are not captured by the chosen simple temporal model function. Simply speaking, the modeled trend and annual variations are not the dominant signals, consequently the coestimated function is a poor approximation of the real ocean variability. In order to see positive effects for the estimation of the MDT and geoid, it is expected that more flexible temporal basis functions are required. For further details see **Brockmann et al., 2023** and Chap. 5 and **Borlinghaus et al., 2023a** for advanced modeling strategies.

4.4.2 Use of Simulated WV Mode RSV Data

Neyers et al., 2022b and **Neyers et al., 2022a** study the potential of Sentinel-1 WV mode RSV data to support the separation of SSH to geoid and MDT to avoid separation errors as seen in Sect. 4.4.1 (cf. **Brockmann et al., 2023**). WV mode delivers a kind of 'point wise' RSV measurements in an alternating far-sight/near-sight pattern with 100 km distance between observations (CLS, 2016). For Sentinel-1, it is supposed to be available in the open ocean, therefore the North Atlantic including the Gulf stream is chosen as a study area (see Fig. 4.7a). Whereas it was originally planned in the PARASURV project to use the real data product as available from the official Sentinel-1 Ocean (OCN) product as distributed by Copernicus, it turned out that due to calibration issues the real data are not usable (Hajduch et al., 2021; Hajduch et al., 2022; Moiseev et al., 2022).

Therefore, synthetic RSV data in WV mode are generated from the gradients of a global MDT model (**Neyers et al., 2022b; Neyers et al., 2022a**). The MDT_CNES_CLS18 is approximated by a high-resolution continuous FES and the estimated parameters are used to forward compute the WV mode RSV from (4.7) for a one year real Sentinel-1 observation geometry (cf. Fig. 4.7a). A reasonably optimistic noise of $0.1\,\mathrm{m\,s^{-1}}$ and $0.25\,\mathrm{m\,s^{-1}}$ is assumed.

The simulated RSV data are used in a geodetic MDT estimation from real SSH data and GOCO06s as geoid information (cf. Sect. 4.3). It is shown in the studies, that in regions where RSV data is available – especially from ascending and descending tracks (cf. Fig. 4.7a) – the RSV data significantly supports the separation. This can be seen comparing the smoothness of the MDT estimates, which use/do not use the RSV data. Whereas Fig. 4.7b shows the solution from SSH and geoid only (the MDT is hardly regularized), the visible ripples indicate an imperfect signal separation, resulting from an imperfect implicit smoothing of the FES. In contrast to that, the solution shown in Fig. 4.7c uses additionally the (synthetic) RSV data. It shows a significantly smoother and better MDT estimate in regions where data is available. This can be supported analyzing the formal accuracy estimates of the MDT (**Neyers et al., 2022b; Neyers et al., 2022a**). These results already indicate, although the information is one dimensional (LOS projection) and sparsely sampled over the ocean, that it is a promising data set for MDT determination. As these studies

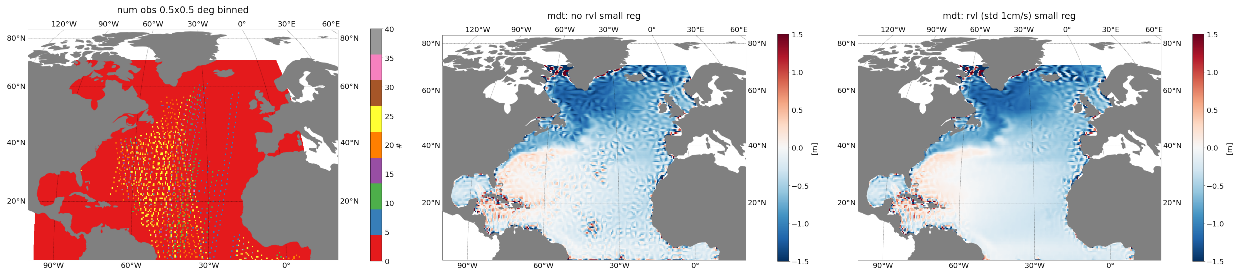

(a) Distribution of Sentinel-1 RSV WV data for one year.

(b) MDT solution from SSH and geoid.

(c) MDT solution from SSH, geoid and RSV.

Figure 4.7: Effect of using (simulated) Sentinel-1 WV RSV data for geodetic MDT estimation in the North Atlantic. Figures are taken from **Neyers et al., 2022b**.

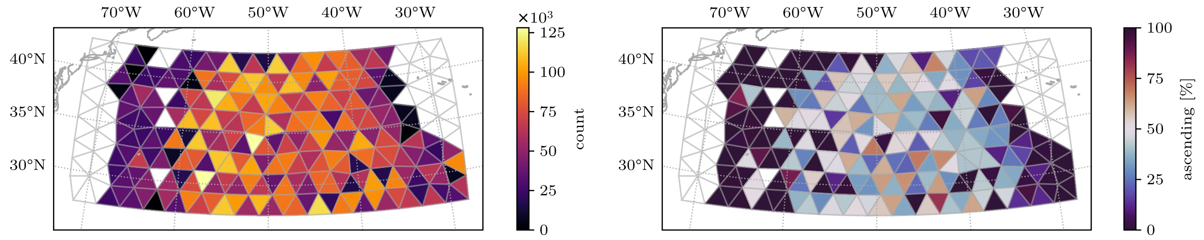

(a) Number of RSV observations falling into each triangle of the MDT model.

(b) Relative amount of observations from ascending orbit, 50 % means equal distribution.

Figure 4.8: Distribution of Sentinel-1A WV-mode grid cells as simulated for this study (years 2010–2019). Aggregated by triangles of the FES mesh. Figures are taken from **Neyers and Brockmann, 2024**.

are simulation based, the conclusions are somehow idealized, as the RSV data only contain signal simulated from a consistent and smooth MDT model.

To create somehow more realistic simulated observations, temporal Total Surface Currents (TSC) data sets (cf. Consiglio, 2020), interpolated in space and time to the Sentinel-1 measurement locations, are used for a ten year RSV simulation, which is basically the projection of the TSC to the LOS. This introduces disturbing signals from ocean dynamics (**Neyers and Brockmann, 2024; Neyers et al., 2022c**). Fig. 4.8 shows the data distribution per triangle of the used triangulation for the Sentinel-1 like simulated WV mode observations for the study area – a subregion of the North Atlantic including parts of the Gulf stream.

For this scenario, three solutions are computed to show the effect of the (simulated) RSV observations (cf. Fig. 4.9) on the estimated MDT. Shown are differences of the estimated MDTs to the DTUUH22 MDT model, a high resolution MDT refined by surface drifters (Knudsen et al., 2022). The FE based estimates are evaluated on the grid defined by DTUUH22. Whereas the first solution combines SSH, geoid and applies regularization of the MDT (cf. Fig. 4.9a) and serves as baseline, the second solution uses the (simulated) RSV observations to replace the regularization (cf. Fig. 4.9b). Finally, the third solution uses RSV and adds regularization to account for the fact that RSV observations are not available in the entire DOI (cf. Fig. 4.9c).

Compared to the baseline scenario, where the gradient of the MDT is minimized by adding smoothness conditions as regularization, it is shown that the WV mode RSV data help to smooth the MDT (cf. Fig. 4.9b). Whereas in regions with data from ascending and descending orbits a very similar smoothing is visible and the results improve (e.g. separation artifacts are removed), regularization is still required in regions where no RSV data or just from a single orbit is available (e.g. western and eastern boundary). Adding the regularization on top, results in the third scenario analyzed, which is most consistent to DTUUH22 (cf. Fig. 4.9c). With the limitation that the studies are simulation based, it is demonstrated that the data are beneficial – although just in LOS direction – for geodetic MDT estimation.

4.4.3 Use of Real IW Mode RSV Data

Whereas the sparsely sampled WV mode is the default mode for the open ocean, Sentinel-1 provides RSV derived from the IW mode in selected interesting coastal regions (CLS, 2016). Although the official products suffer from the calibration issues as well (Hajduch et al., 2021; Hajduch et al., 2022; Moiseev et al., 2022), a one year Sentinel-1 RSV data set, including sea state corrections is available for Southwest Indian Ocean around the Aghulas current (cf. Fig. 4.10, NERSC, 2022) thanks to the re-calibration effort by Moiseev et al., 2020a; Moiseev et al., 2022.

Similar to the study for the (simulated) WV mode data (cf. Sect. 4.4.2), the proposed approach and the implementation is applied to the NERSC, 2022 data set to study the use of real RSV data. The data is used as is, no additional corrections have been applied. Although there are mostly ascending flyovers, many regions sparsely sampled in time (cf. Fig. 4.10) and there are still several remaining artifacts in the data, the usability of the data for MDT and geoid refinement is studied (**Brockmann et al., 2022; Neyers et al., 2022c**).

Again, for the MDT solution from SSH and geoid, additional smoothness constraints for the MDT are required to derive a realistically smooth MDT model. It is shown in the related studies, similar to Sect. 4.4.1, that especially in the coastal region (Fig. 4.11a, center) the strong gradient is not resolved. Instead the signal is wrongly attributed to the geoid (Fig. 4.11b, center) which highlights that the smoothness constraint minimizing the gradient is not sufficient (**Brockmann et al., 2022; Neyers et al., 2022c; Brockmann et al., 2023**). In contrast, once a subset of the IW mode RSV data is used in the estimation approach, the coastal gradient is captured in the MDT model, although some of the systematic artifacts from the data are captured as well. On the level of geostrophic currents it can be shown that the east component (related to the north-south gradient of the MDT) is significantly better than the north component, as the ascending observations are mostly sensitive to the east component of the current. To demonstrate that the geoid improves as well, differences to the combined XGM2019 (Zingerle et al., 2020) are shown in Fig. 4.11b for the GOCO06S model used as geoid information (at degree 200), for the solution computed without RSV data at its maximum degree 600 and finally for the solution with RSV data. As the differences are significantly reduced, it is concluded that the spherical harmonics capture real geoid signal in the DOI.

It was shown that the RSV contains valuable information to support the separation process and has the potential to improve both, the MDT as well as the regional geoid. Due to the limited spatial and temporal availability, still systematic differences are introduced to the solutions. But conceptually the usability could be shown. The availability of more data would allow to improve the data handling and usage, e.g. to remove systematics and reduce the ageostrophic components from the data.

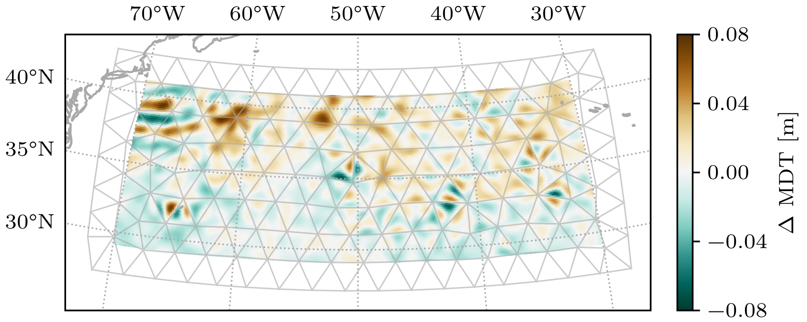

(a) MDT from SSH, GOCO06s and regularization.

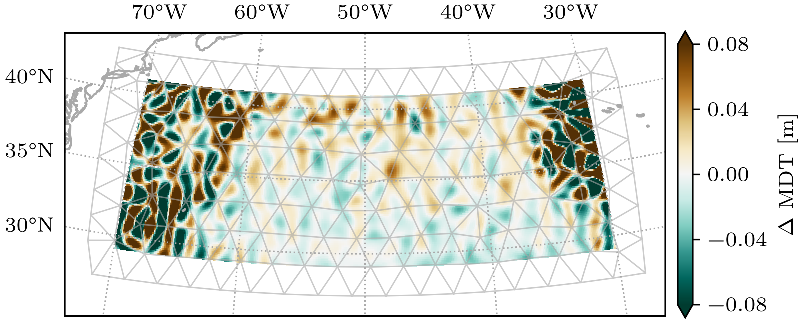

(b) MDT from SSH, GOCO06s and RSV.

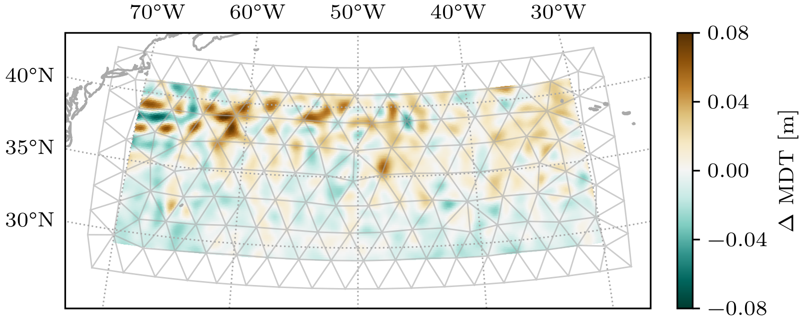

(c) MDT from SSH, GOCO06s, RSV and regularization.

Figure 4.9: Differences of the MDT estimates to the DTUUH22 model in the study area (subset of the North Atlantic ocean) in different scenario configurations. Figures are taken from **Neyers and Brockmann, 2024**.

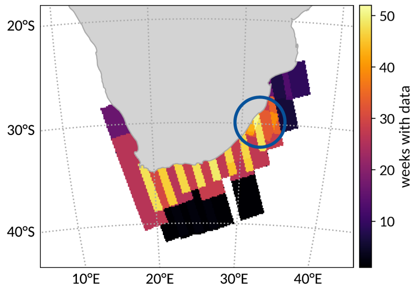

Figure 4.10: Available IW mode data from NERSC, 2022 for the study region around the Aghulas current.

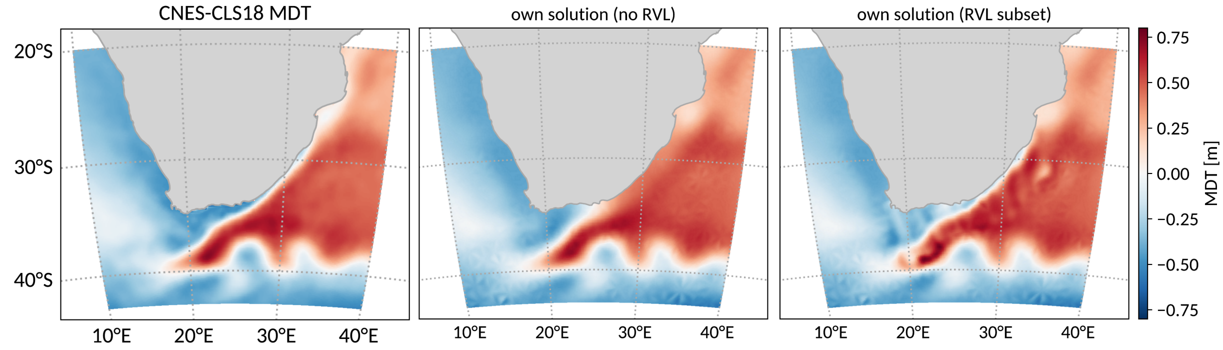

(a) MDT solutions for the study region: MDT_CNES_CLS18 as reference, MDT estimate without RSV, and MDT estimate including IW mode RSV.

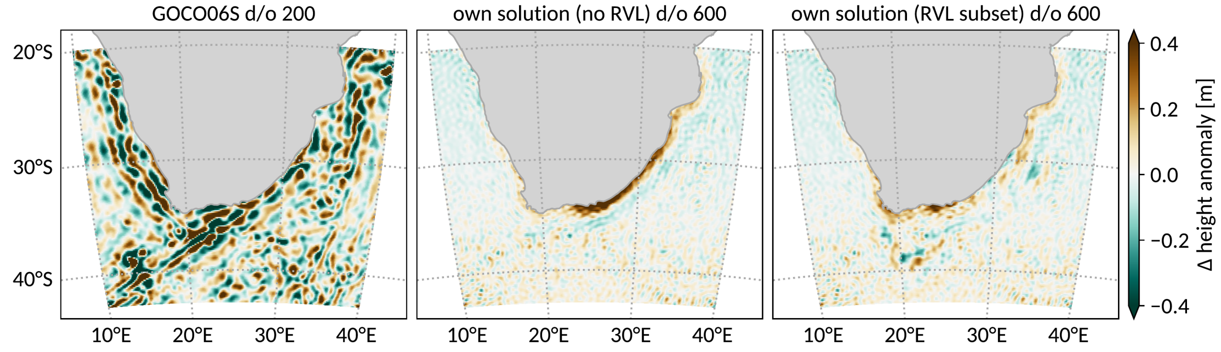

(b) Geoid solutions in the study region as difference to XGM2019 at degree and order 600: GOCO06s at degree 200, geoid estimate without RSV, and geoid estimate including IW mode RSV.

Figure 4.11: MDT and geoid solutions for the study region in the South Indian Ocean. Figures are taken from **Neyers et al., 2022c**.

Chapter 5

Spatio-Temporal Model for the Estimation of the Means Sea Surface

This chapter is based on the work performed in the context of the CST-MSS[1] project. Started in the context of the PARASURV project, the promising results derived in the master thesis by Borlinghaus, 2021, resulted in the project proposal. The CST-MSS project provided initial funding to extend the master thesis to a proof of concept study which served as the preliminary work for the full DFG PhD project proposal COFEBAR[2]. Unfortunately, it was – despite two out of three very positive reviews – not funded, maybe since the proof of concept studies **Borlinghaus et al., 2023a** and **Borlinghaus et al., 2023b** were not timely published. Parts of this chapter are taken in an updated from both proposals, resulting publications, conference contributions and the CST-MSS project report.

5.1 Introduction and State of the Art

As discussed in Sect. 1.1, the MSS is defined as the temporal average of the instantaneous sea surface over a well defined long-term period. As an important reference surface for ocean related studies, e.g. ocean circulation studies (e.g. Mulet et al., 2021a), marine geoid determination (e.g. Andersen et al., 2010) or sea level studies (e.g. Uebbing et al., 2019), the accurate knowledge of the MSS at a high spatial resolution is required (e.g. Abulaitijiang et al., 2021). By definition, mathematically the MSS can be seen after rearranging (1.1) as the difference of the actual SSH and the SLA, i.e. the SSH corrected for its temporal variations.

As already discussed, the SSH can be determined from radar measurements of satellites equipped with an altimeter. The altimetric SSH measurements

$$h_{\text{SSH}} = h_{\text{orb}} - h_{\text{alt}} - c + o + e, \tag{5.1}$$

result from the difference in the altitude of the satellite (h_{alt}) resulting from a precise orbit determination (e.g. Fernández et al., 2024) and the raw altimeter range h_{orb}, which results from the two-way transit time of the emitted radar pulse. This difference has to be corrected due to environmental conditions (c), for instance the sea state bias, atmospheric, tidal and inverted barometer corrections and for a mission specific bias (o) (for further details see Aviso, 2020). Furthermore, the difference includes both random measurement and systematic errors e. Luckily, data providers

---

[1] Development of Continuous Spatio-Temporal Finite Element Based Models for Sea Surface Approximation (CST-MSS). PI J. M. Brockmann. Funded by TRA1 Modelling, University of Bonn as part of the Excellence Strategy of the federal and state governments (2021-2022)

[2] COntinuous spatio-temporal Finite Element Based Approximation models Representing the sea surface (COFEBAR). DFG not funded. Due to the generally positive feedback an update and resubmission is planned.

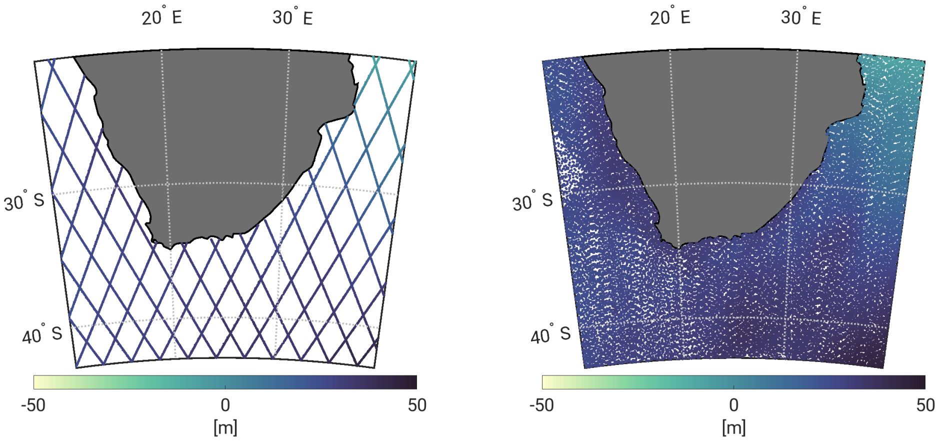

(a) For Jason-1., 10 d repeat cycle, cross-track spacing of 315 km.

(b) For CryoSat-2, 369 d repeat cycle, cross-track spacing of 8 km.

Figure 5.1: Scatter plots of SSH observations taken by the Jason-1 and the CryoSat-2 mission in a one year period for a study region in the South Indian Ocean.

deliver L2 data with corrections for c and o, sometimes even already applied. Therefore, L2 measurements of the instantaneous SSH are available along the ground tracks of the radar altimetry satellites, typically with a 1 Hz sampling (e.g. Aviso, 2020).

Given the altimetric along-track SSH observations, the computation of an MSS seems simple and straightforward: after a temporal averaging over the analysis period, a gridding procedure derives the MSS product for the study region. Unfortunately, already the temporal averaging is challenging (Agha Karimi et al., 2020; Andersen et al., 2021), as it strongly depends on the spatial and temporal sampling of the altimetry missions.

On the one hand, there are the so called ERMs, which have a repeat cycle of 10 d to 35 d, which means that the satellites revisit the same location every 10 d to 35 d. As a consequence of this relatively fine temporal sampling, the cross track distance is 80 km to 300 km which is large compared to the along track sampling of 7 km to 8 km. Figure 5.1a shows a scatter plot of the measured SSH for a one year period of the ERM Jason-1 with a 10 d repeat. It immediately becomes clear that these observations can not resolve the MSS with the required resolution of 5 km to 10 km (Andersen et al., 2021).

On the other hand, to resolve the fine scales, observations from the so called GMs are required. These missions, or dedicated phases of a missions, are operated in an orbit, which has either a long repeat cycle above a year, e.g. 369 d to 406 d or even no repeat period at all. This poor temporal sampling results a significantly higher spatial sampling comparable to the along-tack resolution of 7 km to 8 km. This dense sampling can be seen for the GM CryoSat-2 with a repeat cycle of 369 d in Fig. 5.1b.

From this spatial and temporal sampling characteristics it directly becomes clear that i) for the determination of the fine scale MSS — which is mainly geoid signal — the GMs are essential and ii) the temporal ocean variability (SLA) can only be captured by the ERMs. It may be obvious that temporal averaging to get rid of the ocean variability for the data collected by ERMs is straightforward, temporal averaging of complete cycles, linked to a reference track, directly removes the periodic short-term signals and yields the mean profile of the MSS along the reference track (e.g. Schaeffer et al., 2012; Andersen and Knudsen, 2009). Unfortunately, due to the sampling and the aliasing problem, a direct averaging is impossible for the data collected by GMs.

Therefore, the established approaches for MSS estimation are multi-step approaches, which treat both types of missions as well as the averaging and gridding steps separately. Whereas the ocean variability is removed from the SSHs collected by ERMs as discussed above, SSH collected by GMs are corrected for the SLAs taken from existing products (e.g. from daily or monthly SLA maps, see Traon et al., 1998; Ducet et al., 2000) or derived from the spectral analysis of ERMs data (for further details see e.g. Andersen and Knudsen, 2009; Schaeffer et al., 2012; Jin et al., 2016; Agha Karimi et al., 2020; Andersen et al., 2023).

Both data sets, the temporally averaged SSH from the ERMs and the temporally corrected SSH observations of the GMs are merged in the gridding step. Depending of the approach, different gridding procedures are applied, e.g. discrete binning, weighted spatial interpolation or a collocation-like gridding. Again, see the specific approaches from Andersen and Knudsen, 2009; Schaeffer et al., 2012; Jin et al., 2016; Agha Karimi et al., 2020; Andersen et al., 2023 for further details about the applied gridding procedures. The final MSS products are provided as oversampled grids — e.g. $1'\times1'$ — depending on the study either globally or regionally. Sometimes, gridded accuracy information based on the prediction errors is available for each grid cell.

5.2 Objectives and Contributions

Following the discussion from Sect. 5.1, it became clear that the existing and established MSS products result from multi-step procedures. These rely on prior information to sufficiently account for the ocean variability in the SSH observations taken by the GM. Furthermore, the published MSS products are only provided on predefined grids and lack a realistic uncertainty description.

The idea to tackle these deficits was initially addressed in the master thesis Borlinghaus, 2021 and further studied in the initial funding project CST-MSS. The main idea is to develop a one step procedure to estimate a model of the MSS in a joint adjustment of SSH observations taken by both — ERMs and GMs. Therefore, the integral SSH measurements have to be separated into the static MSS and its temporal variations — the SLA. This requires a continuous model for both, the MSS and SLA in the spatial and temporal domain, to precisely account for the measurement location and its epoch. For the joint estimation, both MSS and SLA are represented by a deterministic spatial and a deterministic spatio-temporal function, respectively. With that, (1.1) can be used to represent the SSH as the sum of both functions, which can directly serve as a basis for least squares OEQs. This requires to find a suitable representation of g_{MSS} and f_{SLA}, as continuous deterministic functions written as linear combinations of different suitable basis functions.

Motivated by the studies in the context of the PARASURV project (cf. Chap. 4), FESs defined on triangulations (cf. Sect. 2.3.1) are studied for a flexible regional approximation of g_{MSS}. Furthermore, these are extended to spatio-temporal functions to approximate the unknown function f_{SLA} (cf. Sect. 2.3.4). Various FEs (**Borlinghaus et al., 2022a**) and FESs are studied to identify individual spatial resolutions tailored to the expected spatial signals of both — MSS and SLA (**Borlinghaus et al., 2023a; Borlinghaus et al., 2023b**). Additionally, the FES used for the spatial modeling of the SLAs has to be tailored to the (across-track) sampling of the utilized ERMs to obtain a stable estimate (**Borlinghaus et al., 2022a**).

As already discussed in Sect. 2.3.4, the spatial FESs are extended to spatio-temporal models assuming separable functions. Therefore, a flexible choice of (one dimensional) basis functions for the temporal domain becomes possible. Two choices, using easily interpretable global basis functions and B-Splines with well-defined filtering characteristics are compared in **Borlinghaus et al., 2023a**. To further stabilize the results — e.g. in coastal areas with only a few observations per triangular mesh cell — tailored regularization strategies are developed to derive smooth estimates (**Brockmann et al., 2023**).

The approach and implementation is studied in detail in **Borlinghaus et al., 2023a** in a small scale proof-of-concept real data experiment. A regional MSS together with the spatio-temporal model for the SLA is estimated from ten years of altimetry data from all ERMs and GMs available in the specific study period. To assess the quality of the MSS, the estimate is compared to established MSS products. Similarly, the estimated SLA model component is validated in a comparison to

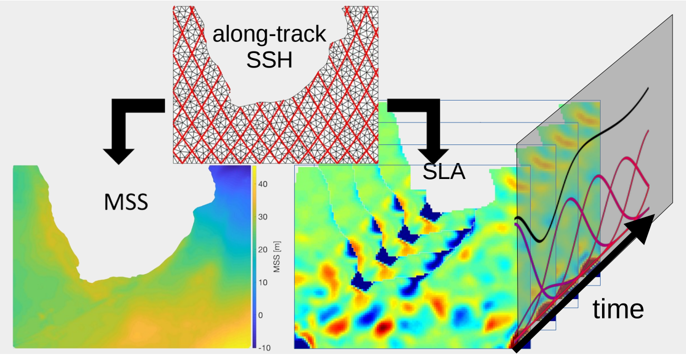

Figure 5.2: Sketch of the MSS estimation approach.

existing and established SLA products. This is used to study the performance of different FESs and different temporal basis functions.

The proposed approach has — at least theoretically — multiple advantages compared to the established approaches, i.e:

(i) Due to the representation by a continious function, the MSS can be computed for any location in the DOI.
(ii) Similarly, due to the representation by a continuous spatio-temporal function, the SLA can be evaluated at any location in the DOI for any epoch.
(iii) Being in the one step least squares framework, stochastic modeling and rigorous variance propagation is possible. Therefore covariances matrices for all MSS and SLA grids can be computed.
(iv) In the least squares framework, additional observation groups can be easily added, e.g. other missions or completely different measurements such as tide gauge records.
(v) The functional model can be extended, e.g. co-estimating or separating additional signals, e.g. replacing the MSS by the sum of geoid and MDT (cf. Chap. 4).
(vi) The required resolution, i.e. spatial or temporal filtering, can be adjusted depending on the requirements.

5.3 Summary of the Modeling Approach

Based on the theoretical considerations prepared in Chap. 2 and the experience with the SSH observations from Chap. 4, the proposed approach is straightforward. The observed SSH is separated into the static MSS and the temporal SLA (cf. sketch in Fig. 5.2). Mathematically, the separation works as soon as a zero temporal mean is guaranteed by the choice of the temporal basis functions. With that, the problem can be formulated as a linear least squares adjustment.

5.3.1 Least Squares Observation Equations

Basic idea is to setup the linear least squares OEQs for the SSH observations taken by both — GMs and ERMs (following **Borlinghaus et al., 2023a**). As the model functions are continuous in space and time, the OEQs for both are the same. Therefore following (1.1), the k-th geophysically corrected SSH observation $\mathcal{L}_k$ taken at location (λ_k, ϕ_k) at epoch t_k by mission m is written as

$$\mathcal{L}_k = g_{\text{MSS}}\left(\lambda_k, \phi_k\right) + f_{\text{SLA}}\left(\lambda_k, \phi_k, t\right) + o_m + \mathcal{E}_k. \tag{5.2}$$

Here, o_m is again an unknown parameter to estimate an intermission bias correction. The random variable $\mathcal{E}_k$ is supposed to model random measurement errors, imperfect corrections c and model errors. The unknown parameters which are supposed to be estimated are still hidden in the function definitions of g_{MSS} and f_{SLA}. As again the true functions $\bar{g}_{\mathrm{MSS}}$ and $\bar{f}_{\mathrm{SLA}}$ are unknown, they are approximated by FEs. The static component modeling the MSS is represented by (2.31), and the spatio-temporal model function for the SLAs by (2.35). Inserting both definitions for the spatial and spatio-temporal functions yields the model function used as OEQ for SSH

$$\mathcal{L}_k = \sum_{i}^{I_{\mathrm{MSS}}} a_{\mathrm{MSS},i} b_{\mathrm{MSS},i}\left(\lambda_k, \phi_k\right) + \sum_{i=1}^{I_{\mathrm{SLA}}} \sum_{j=1}^{J_{\mathrm{SLA}}} e_{\mathrm{SLA},i,j} d_{\mathrm{SLA},j}(t_k) b_{\mathrm{SLA},i}\left(\lambda_k, \phi_k\right) + o_m + \mathcal{E}_k \tag{5.3}$$

in the

$$U = I_{\mathrm{MSS}} + I_{\mathrm{SLA}} J_{\mathrm{SLA}} + M \tag{5.4}$$

unknown parameters

$$\mathbf{x} := \left[\cdots a_{\mathrm{MSS},i} \cdots \quad \cdots e_{\mathrm{SLA},i,j} \cdots \quad \cdots o_m \cdots\right]^{\top} \tag{5.5}$$

to be estimated by a least squares adjustment. M is the total number of missions jointly analyzed. $b_{\mathrm{MSS},i}$ are the FE based basis functions used to spatially model the MSS. As the FES to model the spatial characteristics of the SLAs has to be different (**Borlinghaus et al., 2022a; Borlinghaus et al., 2023a**), the used basis functions are different, i.e. $b_{\mathrm{SLA},i}$. $d_{\mathrm{SLA},j}$ are the basis functions identified to properly model the temporal change of the SLA, i.e. the SLA time series for a single location.

5.3.2 Spatial Finite Element Spaces for MSS and SLA Modeling

In **Borlinghaus et al., 2023a** it is shown that it is required to optimize the spatial resolution of the FESs used for modeling the spatial MSS and SLA signal separately. The along-track sampling of all missions and the cross-track sampling of the GMs allows the resolution of features in the order of 6 km for the static MSS (see e.g. Andersen et al., 2021). Using the Argyris element, as done in Chap. 4 for MDT modeling, this requires a triangulation with an edge length of about 25 km (cf. (4.5)). Using multiple ERMs operated in parallel, e.g. with shifted orbits, it is expected that a spatial resolution in the range of 40 km to 50 km can be resolved for the SLAs. Confirmed empirically, a triangulation with an edge length of about 160 km to 200 km (cf. (4.5)) is well suited to obtain a stable estimate of the SLAs.

Therefore, different meshes are required for both model components, as shown as an example in Fig. 5.3. The DOI Ω_s must be approximated by two overlapping meshes. The meshes are generated as discussed in Sect. 2.3.2. Additional effort is required to ensure that all areas inside the DOI are covered by both meshes. The study in **Borlinghaus et al., 2023a** confirms that using the coarse mesh for both model components yields a stable SLA estimate but significantly degrades the MSS estimate. The high resolution MSS signal is not correctly captured by the chosen function. On the contrary, it is shown that when using the fine triangulation for both model components, both are degraded. The SLA is over-parameterized and captures noise — the correct separation of the SSH in the components cf. (5.2) fails. Although, a specific regularization of the SLA component can compensate for the oversampling, significantly more parameters would have to be estimated. Therefore, the use of the two overlapping triangulations is preferred and numerically less challenging.

5.3.3 Basis Functions for Temporal Model

To model the temporal characteristics, an obvious choice for SLAs is a linear trend superimposed by some (multi-)seasonal harmonics (e.g. Agha Karimi et al., 2020). In this case, following Sect. 2.3.4, (2.32) can be explicitly written as

$$h^{g}_{\mathrm{SLA}}(t) = c_{\mathrm{SLA},1}(t - t_0) + c_{\mathrm{SLA},1} \sin\left(\omega_1 (t - t_0)\right) + c_{\mathrm{SLA},2} \cos\left(\omega_1 (t - t_0)\right) \tag{5.6}$$

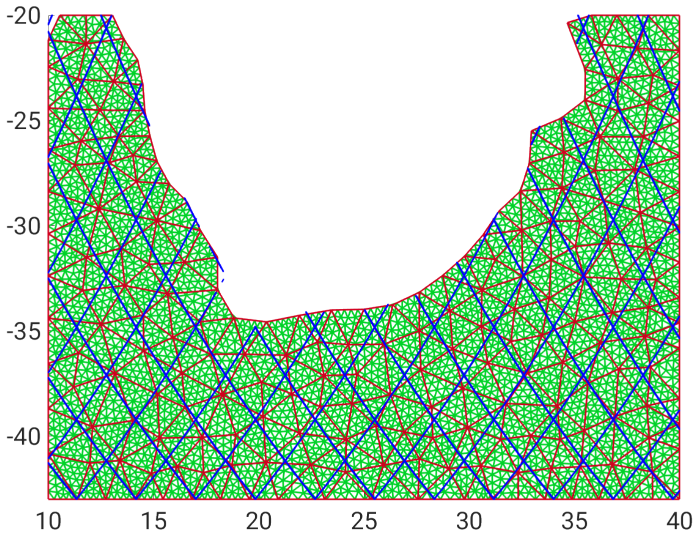

Figure 5.3: Example meshes for MSS estimation. The DOI is partioned into two overlapping meshes. The green mesh is tailored to the resolution requirements of the MSS (in this example 40 km target edge length), the red mesh is tailored to the spatial resolution for the SLA requirements (in the shown example 200 km target edge length). The blue lines show the ground tracks of the ERM of the Jason-family with 10 d repeat orbit.

to model the SLA time series of a fixed location, introducing a reference epoch t_0 and the seasonal frequency ω_1. This yields a first set of potential global basis functions $d_{\mathrm{SLA},j}(t)$ to be inserted in (5.3)

$$\mathrm{T}^g_{SLA} := \{t - t_0, \cos(\omega_1(t - t_0)), \sin(\omega_1(t - t_0))\}. \tag{5.7}$$

Compared to (2.33), 1 is excluded and the reference epoch is introduced. This has the advantage that firstly $h_{\mathrm{SLA}}(t)$ has zero mean, as

$$\int_{-\infty}^{\infty} h^g_{\mathrm{SLA}}(t)dt = 0. \tag{5.8}$$

Therefore, it is impossible for $h^g_{\mathrm{SLA}}(t)$ to compensate a mean, i.e. static MSS signal. Secondly, the reference epoch of the MSS is well defined. Of course, (5.6) can be easily extended by additional, e.g. inter annual frequencies. This temporal model is applied in Sect. 4.4.1 in the context of MDT estimation as well (see **Brockmann et al., 2023; Borlinghaus et al., 2023a**).

The disadvantage of (5.6) is that it is a rigid function. The frequencies are predefined a priori and the estimated amplitudes are static. It is not well suited for the approximation of highly dynamic signals with changing characteristics. An alternative is the use of basis functions with local support, which can be composed to highly flexible model functions with many DOFs. For SLA modeling, uniform B-splines with constant node spacing $\Delta\kappa$ are studied (cf. Sect. 2.3.4). In that case, the temporal function reads

$$h^l_{\mathrm{SLA}}(t) = \sum_{j=1}^{J_{\mathrm{SLA}}} c_{\mathrm{SLA},j} B^p_j(t - t_0), \tag{5.9}$$

with $B^p_j(t - t_0)$ the j-th B-Spline of order p defined in the j-th node (e.g. Fahrmeir et al., 2021, Chap. 8). In the MSS studies (**Borlinghaus et al., 2023b; Borlinghaus et al., 2023a**) uniform B-Splines of order $p = 3$ are used. With that, the set of basis functions is

$$\mathrm{T}^l_{\mathrm{SLA}} := \left\{\cdots B^p_j(t - t_0) \cdots\right\}. \tag{5.10}$$

The use of B-Splines allows a flexible approximation of various signals. A disadvantage is the large number of DOFs, which yields a large number of unknowns. Assuming a monthly node spacing (as in **Borlinghaus et al., 2023a**) for a ten year data period yields J_{SLA} =120, i.e. 40 times more parameters compared to (5.7). Although the number seems small, remember that this is multiplied by I_{SLA} (cf. (5.4)) to determine the total number of parameters to be estimated in spatio-temporal model. Furthermore, in contrast to the parameters in (5.6), they do not have a directly physical meaning.

Restrictions constraining the B-splines at the start and end of the time series might be required. Finally, (5.9) does not have a zero mean, therefore, an additional restriction is derived and has to be applied in a constrained least squares estimation, such that no static MSS signal enters the SLA model component. From the requirement

$$\int_{\Omega_t} h^l_{\text{SLA}}(t)dt \overset{!}{=} 0 \tag{5.11}$$

Borlinghaus et al., 2023a derives the linear constraint

$$\sum_{j=1}^{J_{\text{SLA}}} c_{\text{SLA},j} = 0 \tag{5.12}$$

which can be easily applied in parameter estimation.

5.3.4 Regularization

The separation works under the assumption that the spatial signal of the SLA is smooth. Smoothness is realized in (5.3) via the implicit filtering of the coarse spatial mesh of the FES used for SLA modeling. To further stabilize the solution, e.g. in case of spatial and/or temporal data gaps or at the boundaries of the DOI like coastlines, additional smoothness can be applied by regularization.

Whereas in **Borlinghaus et al., 2023a** a Tikhonov-like regularization is used to minimize a weighted squared sum of the coefficients $\sum_{i=1}^{I_{\text{SLA}}} \sum_{j=1}^{J_{\text{SLA}}} w_{i,j} e^2_{\text{SLA},i,j}$ together with the least squares residuals, alternatives minimizing the norm of the gradient were applied in **Brockmann et al., 2023** (cf. Sect. 4.3.6). Due to the continuous representation, the norm of the gradient can be minimized, i.e. for the MSS $\|f_{\text{SLA}}(\lambda,\, \phi)\|_{L^2(\Omega_s)}$ and similarly for the SLA $\|f_{\text{SLA}}(\lambda,\, \phi)\|_{L^2(\Omega_s,\Omega_t)}$. Applying numerical quadrature for the integration results in a (non-diagonal) regularization matrix for the static MSS. For the temporal SLA, a block-diagonal matrix consisting of J_{SLA} blocks of a similar matrix follows.

5.3.5 Characteristics of the Estimation Problem

With the linear OEQs from (5.3), design matrices and NEQs can be computed cf. (2.7) individually per mission or even mission phase. Accounting for the regularization matrices $\mathbf{N}_r$, the combined NEQs follow again from the addition theorem of normal equations

$$\left(\sum_{m=1}^{M} \frac{1}{\sigma_m^2} \mathbf{N}_m + \sum_{r} \frac{1}{\sigma_r^2} \mathbf{N}_r \right) \tilde{\mathbf{x}} = \sum_{m=1}^{M} \frac{1}{\sigma_m^2} \mathbf{n}_m. \tag{5.13}$$

In case (5.7) is used as the temporal basis functions, (5.13) can be directly solved for the unknown parameters (5.5). In case of (5.10) for the temporal basis, (5.13) is solved accounting for the linear zero mean and B-spline start and end restrictions (e.g. Koch, 1999, Sect. 3.2.7). The relative weighting, with weights $w_{m,r} := \frac{1}{\sigma^2_{m,r}}$, can again be iteratively estimated by VCE (Koch and Kusche, 2002). In the initial studies, SSH observations are assumed to be uncorrelated with the same and constant variance, resulting in $\boldsymbol{\Sigma}\left\{\mathcal{L}_m\right\} = \sigma_m^2 \mathbf{I}$. Of course, the iterative estimation of a stochastic model representation as discussed in Sect. 2.2 is applicable in this context as well.

The assembly and solution of (5.13) is computationally challenging. Due to the high spatial resolution required for the MSS the number of parameters I_{MSS} is large. Compared to this, the number of parameters I_{SLA} for the spatial modeling of the SLA is small, as it decreases squared in the ratio of the spatial resolution. But, especially in case of the temporal B-Spline modeling, which requires many parameters J_{SLA}, the total amount of SLA related parameters $I_{\mathrm{SLA}} \cdot J_{\mathrm{SLA}}$ immediately starts to dominate the total numbers of parameters (cf. (5.4)). Obviously, the total number strongly depends on the study region, defining the DOI. Explicit numbers are discussed for the studied scenarios for the numerical real data experiment in Sect. 5.4.

The total number of parameters is quickly in the order of 10^5, it has to be noted that the NEQs cf. (5.13) are still sparse. The diagonal block corresponding to the MSS parameters has the sparsity pattern resulting from the spatial approximation by FE (cf. Fig. 2.9). The diagonal block corresponding to the SLA parameters contains a repeated sparsity pattern of the spatial FEs. The spatio-temporal design matrix

$$\mathbf{A}_{\mathrm{SLA}} = \mathbf{D}_{\mathrm{SLA}} \bullet \mathbf{B}_{\mathrm{SLA}} \tag{5.14}$$

as it results from the face-splitting product of the temporal design matrix containing the (i.e. in worst case fully populated) temporal basis functions $\mathbf{D}_{\mathrm{SLA}}$ and the design matrix $\mathbf{B}_{\mathrm{SLA}}$. This is sparse, as it contains the spatial FE basis functions with local support. Therefore, the sparsity pattern of $\mathbf{A}_{\mathrm{SLA}}$ corresponds to the sparsity pattern of $\mathbf{B}_{\mathrm{SLA}}$ repeated J_{SLA} times in the worst case. Therefore, the block diagonal of $\mathbf{A}_{\mathrm{SLA}}^{\top}\mathbf{A}_{\mathrm{SLA}}$ has the sparsity pattern resulting from the FESs. The sparsity pattern of the off(block)diagonal part strongly depends on the structure of $\mathbf{D}_{\mathrm{SLA}}$. The off(block)diagonal part of the combined NEQs (5.13) is sparse as well, as it only contains entries for parameters belonging to overlapping triangles (of the SLA and MSS triangulations). Applying reordering strategies as indicated in Sect. 2.4, makes the large dimensional systems easily solvable.

With the estimated parameters, both models g_{MSS} and f_{SLA} can be evaluated individually. Furthermore, $f_{\mathrm{SLA}}(\lambda, \phi, t)$ can be evaluated

(i) as the spatio-temporal model, i.e. the continious function

$$f_{\mathrm{SLA}}(\lambda, \phi, t) \qquad f_{\mathrm{SLA}}: \mathbb{R}^3 \to \mathbb{R}, \tag{5.15}$$

(ii) as a spatial snapshot of the SLAs for a specific time $t_c \in \Omega_t$, i.e.

$$f^s_{\mathrm{SLA}}(\lambda, \phi) := f_{\mathrm{SLA}}(\lambda, \phi, t)\big|_{t=t_c} \qquad f^s_{\mathrm{SLA}}: \mathbb{R}^2 \to \mathbb{R}, \text{ and} \tag{5.16}$$

(iii) as a time series for an arbitrary location $(\lambda_c, \phi_c) \in \Omega_s$, i.e.

$$f^t_{\mathrm{SLA}}(t) := f_{\mathrm{SLA}}(\lambda, \phi, t)\big|_{\lambda=\lambda_c,\, \phi=\phi_c} \qquad f^t_{\mathrm{SLA}}: \mathbb{R} \to \mathbb{R}. \tag{5.17}$$

5.4 Selected Results of the Proof of Concept Study

5.4.1 Summary of the Studied Scenarios

In the initial study from **Borlinghaus et al., 2022a**, the basis for the configuration of the spatial FEs were studied. It was identified, similar to the results shown in Sect. 2.3.3, that the Argyris element again yields a better approximation of the spatial MSS and SLA signals, using even less parameters compared to the HCT element. Furthermore, it is shown that the spatial resolution for MSS modeling requires an edge length of 30 km to 50 km using the Argyris element. It is concluded that a coarser mesh is required to obtain stable SLA estimates avoiding an over-parameterization. These results were considered in the proof of concept study from **Borlinghaus et al., 2023a** which serves as a basis for the results summarized here.

To study the performance of the proposed estimation approach, the MSS is estimated in a real data experiment in different scenarios in a regional study area in the south-west Indian Ocean

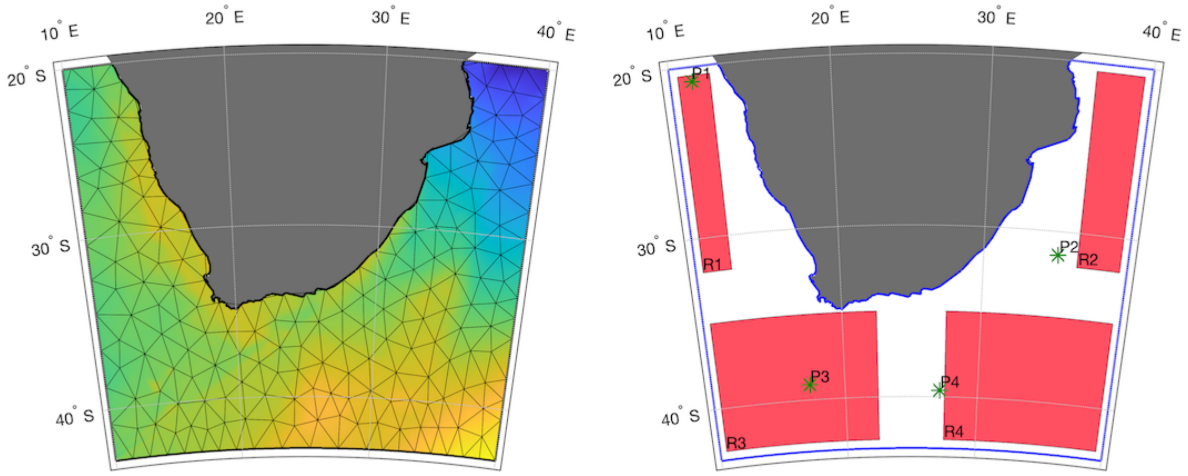

(a) MSS signal from the CNES_CLS15 MSS model and the used 175 km mesh used to model the spatial SLA signal.

(b) Sub regions and individual points used for the validation of the estimates and the computation of the statistics.

Figure 5.4: Study region in the South Indian Ocean used for the MSS estimation real data experiment. Figure is taken from **Borlinghaus et al., 2023a**.

(cf. Fig. 5.4). Again, ten years of 1 Hz sampled SSH observations (more then 8×10^6) from all altimetry missions existing in the Aviso[3] data base for the period 01/2010 until 12/2019 (I.e. ERMs: Jason-1/2/3, Envisat, SARAL, HY-2A, Sentinel-3A/B GMs: CryoSat-2, Jason-1/2/3 GM, SARAL drifting phase, HY-2A GM) were used to estimate the MSS and SLA in different configurations applying the approach introduced in Sect. 5.3 (**Borlinghaus et al., 2023a**).

Amongst others, three major scenarios were analyzed, which are summarized in Tab. 5.1. They mainly differ in the modeling choices for the spatio-temporal SLA, i.e.

Scenario S This is the 'static' scenario – the SLA is not co-estimated. Instead, it is assumed that the temporal signal cancels by the implicit spatio-temporal filtering of the FES while estimating the MSS parameters.

Scenario G The SLA is co-estimated using the linear trend and seasonal harmonics as temporal basis functions, i.e. (5.6) is applied in (5.3) as temporal model. This assumes that sea-level rise as well as the seasonal variations are the dominating signals in the observed SLAs.

Scenario B Instead of global basis functions, scenario B uses B-Splines of order three with a constant node spacing of 1/12 yr, thus the temporal resolution is significantly higher compared to Scenario G. Due to the choice of local basis functions, the number of unknown parameters is significantly higher (cf. Tab. 5.1).

For the spatio-temporal scenarios the reference epoch is explictly set to January 1, 2015, i.e. in the middle of the analyzed observation interval. For scenario S, it is in the middle of the interval, but not that well defined, e.g. in case of an unbalanced temporal observation distribution.

5.4.2 Assessment of the MSS Estimates

For all three scenarios (cf. Tab. 5.1) the MSS is estimated as a continuous function in the entire DOI. Just evaluating $g_{\mathrm{MSS}}(\lambda, \phi)$ yields the MSS for location (λ, ϕ) inserting the estimated parameters $\tilde{a}_{\mathrm{MSS},i}$ of the respective scenario. These estimates for the MSS can directly be compared with other MSS models after an adjustment of the reference epoch (cf. Pujol et al., 2016). Fig. 5.5 shows the

---

[3] The altimeter products were produced and distributed by Aviso+ (`https://www.aviso.altimetry.fr/`), as part of the Ssalto ground processing segment.

Table 5.1: Major scenarios analyzed for MSS estimation.

scenario	mesh edge length		number of parameters				temporal model
	MSS	SLA	I_{MSS}	I_{SLA}	J_{SLA}	U	
S	25 km	—	68 376	0	0	68 384	none
G	25 km	175 km	68 376	1833	3	73 883	trend, annual harmonics
B	25 km	175 km	68 376	1833	123	293 843	B-Spline, $\Delta\kappa = \frac{1}{12}$ yr

difference of the three different MSS estimates to the gridded CNES_CLS15 MSS model (Schaeffler et al., 2016; Pujol et al., 2018). To obtain the differences, the three estimated MSS models are evaluated on the grid defined by CNES_CLS15.

Looking into the differences of the simplest scenario S, it can been seen that already a reasonable MSS is estimated. Fig. 5.5a together with Tab. 5.2 shows an RMS of 3.3 cm, therefore both models agree already quite well. The adjustment procedure together with the filtering characteristics of the FES already take care of the averaging of a large part of the temporal SLA signal. It can be seen that the differences are spatially inhomogeneous, they are significantly larger in the latitude band around 38 ° S. In this region the Agulhas current leads to strong ocean dynamics, resulting in highly variable SLAs. These highly dynamic regions are represented by the sub regions R_3 and R_4 (cf. Fig. 5.4b). Tab. 5.4b shows the highest RMS in this sub regions of 3.9 cm to 4.3 cm. Differences are smallest at the west coast of the South African continent. This area is represented by sub region R_1, in this region a low ocean variability is expected. Consequently, the RMS for R_1 is smallest, it is just 1.3 cm. Sub region R_2 at the Eastern coast is somewhere between, slightly higher ocean variablity is expected, which is visible in the increased RMS of 2.6 cm.

Switching now to scenario G, i.e. coestimating the simple spatio-temporal model for the SLAs shows similar characteristics in Fig. 5.5b, but with a visually decreased noise level. This is confirmed by the RMS values from Tab. 5.2, the value is reduced by 12 % to 2.9 cm. The reduction for all sub regions is similar. This shows that the coestimated spatio-temporal model already compensates SLA signal, which reduces leakage in the implicit temporal averaging for the MSS model component. Therefore, errors are reduced and consistency to the reference MSS is increased. Still, Fig. 5.5b shows many high frequencies in the difference signal.

These high frequency differences are significantly reduced when switching to scenario B with the advanced B-Spline modeling of the temporal signal (cf. Fig. 5.5c). The RMS is reduced to 2.0 cm and even further for all sub regions. This reduction is even larger compared to the first model refinement. Therefore, it has to be concluded that the leakage is further reduced. Obviously, the MSS from scenario B performs best. Still, regions of higher ocean variability show largest differences in Fig. 5.5c). This means on the one hand, that the modeling of the SLA is not yet perfect, the temporal resolution can still be increased (see Sect. 5.4.4). On the other hand, the differences are influenced i) by errors contained in the CNES_CLS15 model and ii) the fact that both models are computed from different data from a different observation period. The applied adjustment of the reference epoch (cf. Pujol et al., 2016) is not free of errors as it applies altimetry derived filtered SLA maps. Of course, regions of strong ocean variablity are influenced most.

Anyway, for a first proof of concept study the agreement of 2 cm is good — the agreement between the CNES_CLS15 MSS and an alternative established MSS product, i.e. DTU18 MSS, is 2.8 cm in the study region. Therefore, the estimated model is well inside the expected consistency interval (**Borlinghaus et al., 2023a**).

5.4.3 Assessment of the SLA Estimates

To validate the spatio-temporal model components, the estimated SLA component can be compared to existing and established SLA products. Here, the established gridded SLA data set (daily

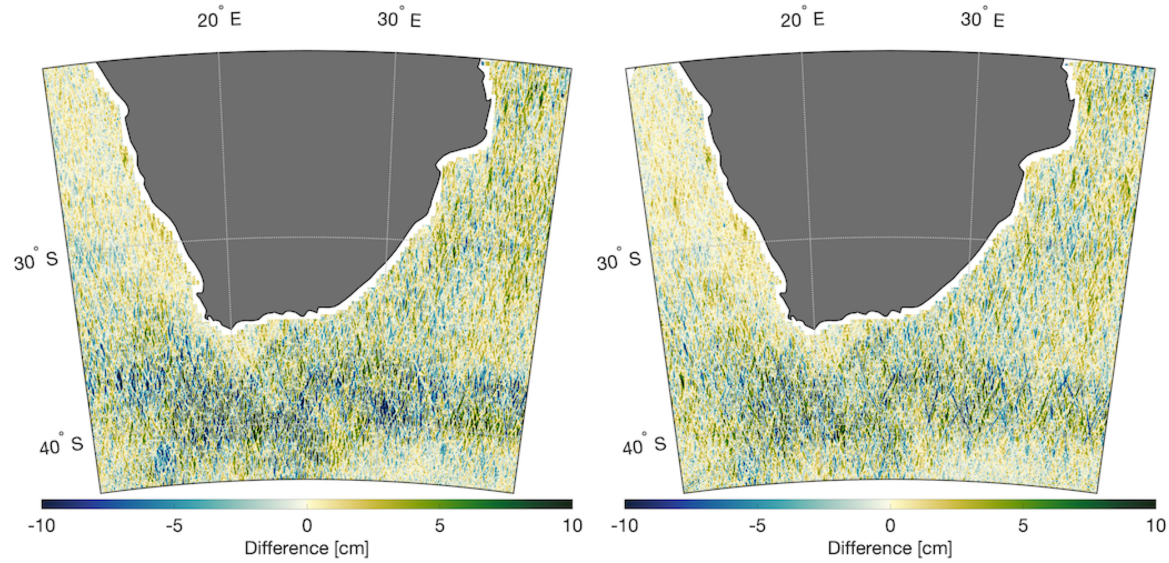

(a) For scenario S.

(b) For scenario G.

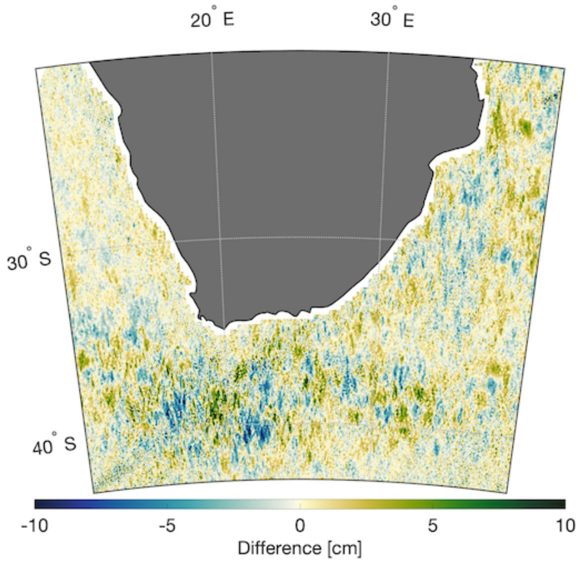

(c) For scenario B.

Figure 5.5: Difference of the MSS estimates to the CNES_CLS15 MSS used as reference. Figure is taken from **Borlinghaus et al., 2023a**.

Table 5.2: RMS values for the differences from Fig. 5.5 in the entire domain and for the four sub regions defined by Fig. 5.4b. Table is a shortened version from **Borlinghaus et al., 2023a**.

Scenario	Median	RMS	RMS R_1	RMS R_2	RMS R_3	RMS R_4
S	0.6 cm	3.3 cm	1.3 cm	2.6 cm	4.3 cm	3.9 cm
G	0.3 cm	2.9 cm	1.1 cm	2.4 cm	3.8 cm	3.2 cm
B	0.5 cm	2.0 cm	0.8 cm	1.7 cm	2.7 cm	1.9 cm

DUACS Level 4 gridded SLA DT2018, Taburet et al., 2019) which was already used in Sect. 4.4.1 is applied as reference.

Obviously, only scenarios G and B are validated. To highlight the advantages of the parameterization of the linear trend and the annual harmonics in scenario G, **Borlinghaus et al., 2023a** performed exactly the same comparison of amplitudes and trends as done for the co-estimated SLA in Sect. 4.4.1 in the context of MDT estimation. As the results from Fig. 4.5 are very similar to the results from scenario G, they are not repeated here, instead refer to **Borlinghaus et al., 2023a** for an additional discussion in the context of MSS estimation.

To not compare spatial snapshots for single days, comparison at time series level for selected locations is performed in **Borlinghaus et al., 2023a**. Therefore, Fig. 5.6 shows the time series of four selected locations from the daily SLA product in orange. For both scenarios, i.e. G and B which coestimate the SLA, the time series is evaluated using (5.17) for all four locations and plotted in blue (G) and green (B). Additionally, a time series from an additional scenario studied in **Borlinghaus et al., 2023a** is included (additional sub seasonal frequencies are added compared to scenario G) as a red line. The idea for the choice of the four locations is that these are representative for the regions. I.e. location P_i is in or close to region R_i. Therefore, the same characteristics as discussed above are expected. Indeed, the characteristics can be seen in Fig. 5.6 directly from the orange lines (note the different limits and scaling of the y-axis).

P_1 is located in the region of low ocean variability. The reference SLA time series clearly shows a seasonal period with an amplitude of 0.05 m. Therefore, the model from scenario G is already a good approximation, although the B-Splines from scenario B better approximate the variations. For the other locations P_2 to P_4, it is obvious that the seasonal signal is not dominating, higher frequency variations in the order of ± 0.5 m are visible. Therefore it is obvious that the seasonal model from scenario G is a poor approximation of all three time series, the B-Spline better fits the reference data. But, it must be noted that the temporal resolution is not yet perfect — the filtering characteristics are clearly visible. A higher temporal resolution is desired (cf. Sect. 5.4.4). These findings are generally inline with the findings from **Brockmann et al., 2023** summarized in Sect. 4.4.1.

Together with the further analysis shown in **Borlinghaus et al., 2023a**, it is obvious that the coestimation of the SLA works and that meaningful SLA signal is captured. The flexible B-Spline model is better suited and improves the MSS estimation and yields a filtered continuous spatio-temporal SLA product.

5.4.4 Further Developments and Refinements

Since **Borlinghaus et al., 2023a** was published, further studies were done. Whereas the meshes used so far were homogeneous, **Borlinghaus et al., 2023b** studied the adaptive refinement of the mesh as already summarized in Sect. 2.3.2. Basic idea is to use least squares residuals of the adjustment, to detect spatial regions with suspicious residuals which are candidates for a mesh refinement. These strategies can be used to optimize both meshes — for the MSS as well as the SLA. This does not only yield a better approximation, but can be used in addition to significantly reduce the number of parameters. In regions with a smooth spatial signal, coarser meshes are possible.

Furthermore, analyzing a smaller DOI to reduce the computational complexity, it was shown that when regularization is applied, the spacing of the B-Splines can be significantly reduced to obtain a higher temporal resolution. Fig. 5.7 shows a time series as in Fig. 5.6, but for a scenario with a B-Spline node spacing reduced by a factor of three, i.e. $\Delta\kappa = 10$ d. It is directly visible that the estimated model (blue line) nicely matches the DUACS SLA product used for comparison (orange line). Additionally, very close SSH observations reduced by the MSS component, are shown (red asterisks). It can be visually concluded that a higher temporal resolution is possible and should be targeted for future studies, as an over-parameterization is not visible. Instead state of the art products are well reproduced and the observations are approximated well.

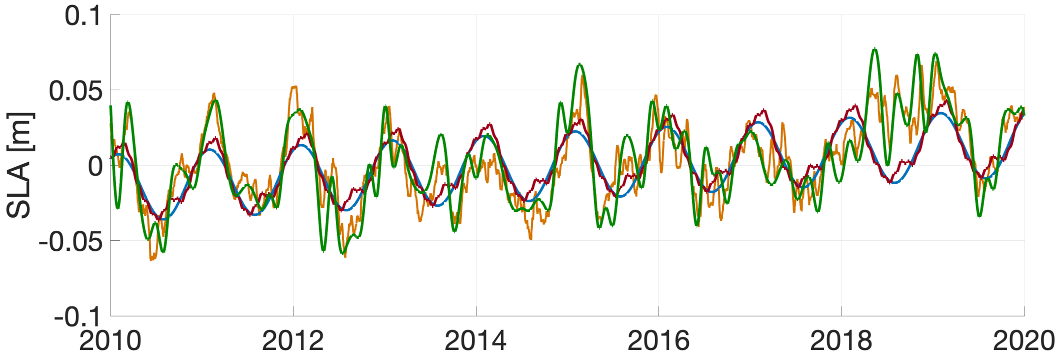

(a) Time series for location P_1.

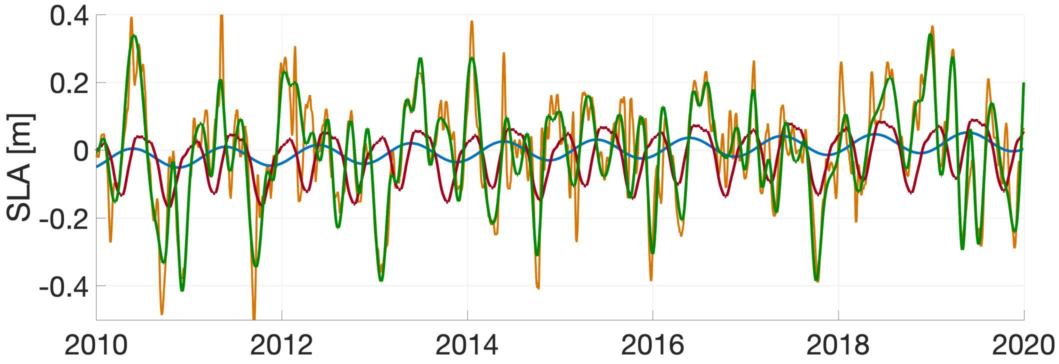

(b) Time series for location P_2.

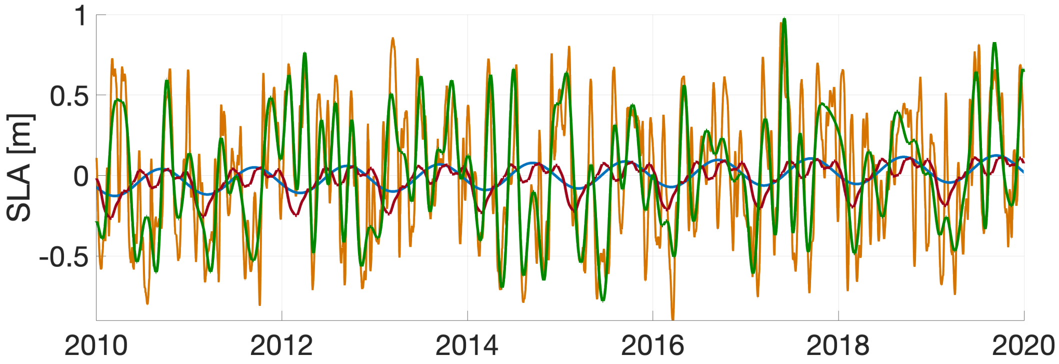

(c) Time series for location P_3.

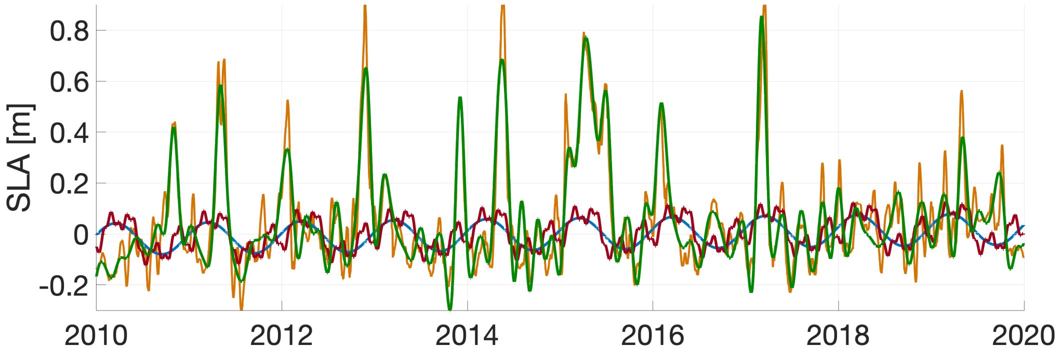

(d) Time series for location P_4.

Figure 5.6: SLA time series for four selected locations in the study region (cf. Fig. 5.4b). The orange lines show the reference SLA from the daily DUACS Level 4 gridded SLA DT2018 data set. The blue lines shows the estimated SLA from scenario G and the green lines from scenario B. The red line is from another scenario, where harmonics of multiple frequencies are estimated. The figure is taken from **Borlinghaus et al., 2023a**.

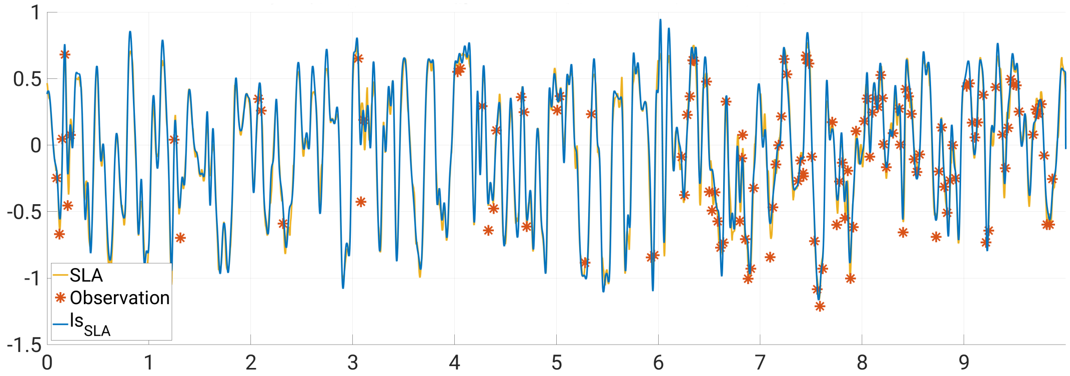

Figure 5.7: SLA time series for a selected location (between P_3 and P_4 cf. Fig. 5.4b) from a scenario with higher spatial resolution. The orange lines show the reference SLA from the daily DUACS Level 4 gridded SLA DT2018 data set. The blue lines shows the estimated SLA from a scenario with a higher spatial resolution (i.e. reduced $\Delta\kappa = 10\,\mathrm{d}$). Additionally, very close SSH observations (reduced by the MSS) are shown as red asterisks. Figure credit: Moritz Borlinghaus.

Chapter 6

Summary, Conclusions and Outlook

6.1 Summary and Conclusions of the Contributions

The monitoring of spatio-temporal changes in the dynamic system Earth is an important task in geodesy. To make these changes visible and detectable, accurate reference surfaces are required to represent the variations with respect to the long term mean. These reference surfaces have to be determined from — in this case — satellite based geodetic measurements, which typically contain other disturbing signals and correlated measurement noise. In this thesis, the reference surfaces are represented by continuous parametric mathematical functions, which allows for the formulation of the determination of the reference surface as a well known parameter estimation problem. However, the corresponding solution becomes computational challenging, in case a rigorous one step procedure is followed, as for instance

(i) a huge set of observations is jointly analyzed,
(ii) many parameters are required to accurately describe the reference surface,
(iii) the observations are highly correlated, which has to be carefully modeled,
(iv) heterogeneous and complementary types of observations have to be combined, and
(v) signals superimpose each other, so they have to be separated.

How to deal with these aspects is summarized in this thesis for the determination of three important and interconnected reference surfaces, the geoid, the MDT and the MSS. The employed approaches have in common that they are developed as one-step least squares procedures, designed to handle multiple complementary observation data sets, while accounting for their individual stochastic characteristics. All reference surfaces are parameterized as continuous functions, which enables the inclusion of all kinds of in-situ observations expressed as functionals of the reference surfaces. The above results in a solution of a numerically and computationally challenging large dimensional adjustment problem.

Theoretical contributions, relevant for more than one of the three applications are discussed jointly in Chap. 2. This covers both aspects required in the least squares adjustment process (cf. Sect. 2.1), the stochastic (cf. Sect. 2.2) and the functional model (cf. Sect. 2.3). Whereas the first includes efficient strategies for data-adaptive covariance modeling and decorrelation strategies, the latter tackles the approximation of unknown spatial and spatio-temporal functions by continuous C^1-smooth FESs, in case no physically motivated function to approximate the reference surface is available. Additionally, computational, numerical and HPC aspects are discussed (cf. Sect. 2.4).
It is shown in Sect. 2.2 that AR processes are a flexible tool to iteratively estimate a data adaptive representation of the stochastic model. Strategies to robustify the estimation of such a stochastic model do not only result in stable estimates of the process, but additionally detect suspicious data and outliers in a consistent way. Stationarity assumptions are typically required to obtain redundancy for the estimation of the stochastic characteristics. These assumptions can be weakened, considering time-variable stochastic processes. Relations between the corresponding decorrelation

filters and the associated covariance functions allow switching between the representations to make use of efficient algorithms for decorrelation, such as exploiting sparsity.
Section 2.3 introduces the use of FE basis functions for spatial approximation tasks to obtain C^1-smooth surfaces described by continuous functions. Two different sets of C^1-smooth elements are compared, the HCT and the Argyris elements. It is shown that the latter is preferable for the approximation tasks considered in this thesis. Both FESs are defined on triangulations, which are well suited to approximate irregular DOIs, such as the ocean bounded by coastlines. Strategies, requirements and tools for the generation of the required meshes are provided. Following the idea of separable functions, the spatial FE-based functions are extended towards spatio-temporal functions, allowing to represent time variable surfaces. It is implemented in a way that arbitrary one dimensional functions can be used for the temporal model. In this thesis, polynomials and harmonics are compared with B-Spline basis functions with finite support. From the real-data applications, it can be concluded that the flexible B-Spline basis functions are well suited for approximation tasks of highly time-variable surfaces.
In Section 2.4, concepts are shown, how the advanced computational and numerical challenges can be tackled, when applying the modeling approaches discussed above. It can be concluded that the FE based spatial and spatio-temporal model is a highly flexible representation for surfaces and shows a very good performance in spatial and spatio-temporal approximation tasks and are a good alternative to the grid based approaches. Both approaches offer advantages due to their continuous definition in space and time. Consequently it is easy to combine heterogeneous observation types, include sparse and incomplete observations and perform rigorous variance propagation.

The first reference surface considered in the applications is the geoid in Chap. 3. The geoid is not directly estimated, but instead observations taken by satellites are used to model the Earth's gravity field as an SH series.
Specifically, observations by the satellite mission GOCE — i.e. gravity gradients and GPS derived satellite positions — are analyzed to estimate the official ESA EGM_TIM_RL06 global gravity field model (cf. Sect. 3.4.1). Reprocessed gravity gradient data together with the updated estimation of the stochastic model, resulted in an improved global gravity field with a realistic covariance matrix. The published model is one of the internationally most accepted GOCE-only models. Compared to its predecessor, it is found that the accuracy improved globally between 10 % to 25 %. Additionally, large systematic errors were reduced and the associated covariance matrix is more realistic as demonstrated in comparisons to external data sets.
With its characteristics as a GOCE-only model with a high quality covariance matrix, the time-wise models are perfect inputs to combined satellite-only models. For instance EGM_TIM_RL06 is combined together with models derived from GRACE, SLR and LEOs to obtain the combined satellite only model GOCO06S (cf. Sect. 3.4.2). GOCO06S is one of the internationally most used satellite-only models, known for its quality and the realistic covariance matrix.
What remains true for the time-wise GOCE models, holds true for GOCO satellite-only models as well. With their characteristics, the GOCO models are well suited as a basis for the combination with terrestrial gravity data and altimetry derived gravity over the oceans. This is done for instance with GOCO05S to obtain the combined GOCO05C model (cf. 3.4.3).

The second reference surface considered is the MDT, which is discussed in detail in Chap. 4. A geodetic estimation approach is proposed and studied, jointly estimating the MDT, the gravity field and, optionally, SLAs to account for the temporal ocean variability. Main input are along-tack altimetric SSH observations, which are separated into MDT and geoid (and SLA) within a least squares parameter estimation approach. This requires to represent the MDT as parametric function, which is realized using the FEs introduced in Sect. 2.3. Similarly, the SLA are parameterized as a spatio-temporal function, cf. Sect. 2.3.4. The separation works, in case complementary gravity field information enters the adjustment and smoothness assumptions of the MDT are added as regularization. Here, GOCO06S from Sect. 3.4.2 serves as input. In Section 4.3, the parametric approach is presented. It can be concluded that the approach has several advantages compared to the state-of-the-art grid based approaches. It is shown that — as in the framework of least squares adjustment — covariance information of the observations can be easily included and propagated to the MDT estimates (cf. Sect. 4.3).

The OEQs for the SSH observations can be extended, e.g. to coestimate a parametric model for the SLA. This improves the processing of observations from GMs, for which the ocean variability does not necessarily average out. The main motivation for using the parametric model is to enable the inclusion of more advanced and complementary observations types. It is shown in different studies (cf. Sects. 4.4.2 and 4.4.3) that the chosen C^1-smooth models allow for the inclusion of SAR-derived RSV, which can be linked to the LOS projected gradient of the MDT. OEQs are developed and the numerical studies demonstrate the benefit of this observable. Similarly, ocean surface drifters can be included.

The final reference surface targeted in Chap. 5 is the MSS. Similarly as for the MDT, a parametric approach is developed, to represent the MSS by a continuous function. The parameters are estimated from altimetric along-tack instantaneous SSH observations in a least squares framework. By definition, the MSS is — as the name says — defined by the long-term mean of the sea surface. Therefore, it is required that the estimation approach successfully separates the instantaneous SSH measurements into the temporal ocean variability (the SLAs) and its steady-state part (the MSS). For this, the SLA has to be parameterized as well, but now as a spatio-temporal continuous function for which the parameters have to be coestimated in order to absorb the temporal ocean variability. Again, as the functions, which describe the spatial signal of the MSS and SLA, are unknown, both functions are approximated by C^1-smooth FESs as introduced in Sect. 2.3. The FES — i.e. primarily the triangulation — for the MSS is tailored to the resolvable spatial resolution allowing to jointly analyze observations from ERMs and GMs. In contrast, the FES for the SLAs is tailored to the cross-tack spacing of the ERMs, as only these can resolve the temporal variability. Using the assumption of separable basis functions, the spatial FEs are merged with different temporal basis functions to realize the continuous spatio-temporal model (cf. Sect. 2.3.4). With that, both model components, MSS as well as SLA can be estimated in a linear least squares adjustment using the OEQs, constraints and regularization concepts summarized in Sect. 5.3. Compared to the other approaches, various advantages can be concluded. First of all, along-tack observations from ERM and GM can be handled exactly the same way. Secondly as the temporal model is explicitly coestimated, the reference epoch for the MSS is well defined, e.g. in case of temporally unbalanced distribution of observations. Furthermore, the stochastic characteristics of the observations can be easily modeled, e.g. applying the concepts from Sect. 2.2.

The developed approach is validated in several scenarios in a regional numerical real data study. Using different configurations for the FES of the MSS, the SLA as well as different temporal models, the performance of the approach is tuned and both MSS (cf. Sect. 5.4.2) and SLA (cf. Sect. 5.4.3) are successfully estimated. The scenario utilizing the Argyris element with a 25 km mesh for the MSS, a 175 km mesh for the SLA, and a temporal B-Spline model with a node spacing down to 10 d yields the estimates with best quality. The RMS with respect to an established MSS product is about 2 cm in the study region, which is well within the consistency level of other established MSS products.

6.2 Outlook and Future Perspectives

This thesis summarizes the work related to the parametric estimation of reference surfaces in the least squares framework, while accounting for the stochastic characteristics of the analyzed data sets. Due to the characteristics of the studied reference surfaces, a huge number of parameters have to be estimated. Together with the fact that the correlations in the observations can be modeled the computational challenges significantly increase. Despite the numerical and computational challenges, the chosen problem formulation in the least squares framework enables potential future work related to the following exemplary subjects:

(i) It is easy to include additional observation types sensitive to at least one of the signals parameterized in the OEQs. For example tide gauge measurements can be used to connect the MSS or MDT to tide gauge stations. Surface drifter observations can be linked to the slope of the MDT. Although their spatial and temporal sampling is extremely sparse, it is straightforward to add this observation type in the continuous parametric approach.

(ii) It is straightforward to extend the OEQs for additional signals to be estimated. For instance, the OEQs used for SSHs assumed that the tides were corrected free of errors as part of the geophysical corrections. As the frequencies of the tides are known, a spatio-temporal model component for specific temporal frequencies can be added to coestimate empirical corrections for the applied ocean tide model.

(iii) Mainly for computational reasons in the proof-of-concept studies, the MDT was only estimated regionally, although the gravity is already parameterized globally. Significantly more SSH observations and additional FE parameters will further increase the computational needs. Extensions towards the global domain require further developments.

(iv) Similarly, the MSS studies was applied in MatLab® based prototype environment so far, fully exploiting the sparsity characteristics of the involved matrices. Considering larger study regions requires a tailored HPC implementation, which is able to fully exploit the sparsity. In the context of correlated measurements, further research is required to derive an efficient implementation in an HPC environment.

(v) With the Surface Water and Ocean Topography (SWOT) mission, a totally new altimetry mission realizing SAR interferometry is in orbit since 12/2022. The mission defines new benchmarks with respect to the obtainable temporal and spatial resolution. On the one hand, this requires advanced quality of the reference surfaces, but on the other hand, also allows for a significant increase in resolution.

(vi) The spatio-temporal model developed for SLA modeling can be transferred to other spatio-temporal approximation tasks, e.g. for deformation monitoring with InSAR (see **Borlinghaus et al., 2022b; Schuh et al., 2023**) or modeling of the water level of inland water bodies.

With this thesis a large set of tools and modeling concepts has become available, which will be further developed and applied to alternative data sets in the future.

Now, as member of the new space geodesy group, these modeling approaches will be transferred to the spatial and temporal analysis of observations taken by the different space geodetic techniques, namely Global Navigation Satellite Systems (GNSS), SLR, Doppler Orbitography and Radiopositioning Integrated by Satellite (DORIS) and Very Long Baseline Interferometry (VLBI). For the realization of reference frames, the observations of the different space geodetic techniques have to be consistently combined, which results in similar computational and numerical challenges. Combining the different space geodetic techniques via common parameters, realized via common clocks, common troposphere parameters, significantly increases the parameter space that has to be explicitly estimated. Therefore, the methodological aspects, the numerical and computational insights and the developed modeling strategies will be transferred to these new applications.

List of Figures

List of Tables

List of Acronyms

AR AutoRegressive.
ARMA AutoRegressive Moving Average.

BLAS Basic Linear Algebra Subprograms.
BLUE Best Linear Unbiased Estimator.

CHAMP CHAllenging Minisatellite Payload.
COFEBAR COntinuous spatio-temporal Finite Element Based Approximation models Representing the sea surface.
CST-MSS Development of Continuous Spatio-Temporal Finite Element Based Models for Sea Surface Approximation.

d/o spherical harmonic degree and order.
DCA Doppler Centroid Anomaly.
DETECT CRC 1502 DETECT: Regional Climate Change: Disentangling the Role of Land Use and Water Management.
DFG Deutsche Forschungsgemeinschaft/German Research Foundation.
DOF degrees of freedom.
DOI domain of interest.
DOT dynamic ocean topography.

EIGEN European Improved Gravity model of the Earth by New techniques.
ERM Exact Repeat Mission.
ESA European Space Agency.

FE Finite Element.
FEM Finite Element Method.
FES Finite Element Space.

G/O2000 Rigorous computation of high resolution spherical harmonic gravity models on massively parallel computer systems.
GM Geodetic Mission.
GNSS Global Navigation Satellite Systems.
GOCE Gravity Field and Steady-State Ocean Circulation Explorer.
GOCE-HPF GOCE High Level Processing Facility.
GOCE-TIM GOCE time-wise.
GOCO Gravity Observation COmbination.
GPS Global Positioning System.
GPU Graphical Processing Unit.
GRACE Gravity Recovery and Climate Experiment.
GRACE-FO GRACE Follow-On.
GRF Gradiometer Reference Frame.

HBN15 Adaptive Optimization of Global Gravity Field Modeling and the Ocean's Dynamic Topography.
HCT Hsieh–Clough–Tocher.
HPC High Performance Computing.

ICGEM International Centre for Global Earth Models.
IW interferometric wide swath.

JSC Jülich Supercomputing Centre.
JUWELS Jülich Wizard for European Leadership Science.

LAPACK Linear Algebra PACKage.
LEO Low Earth Orbiter.
LOS line-of-sight.
LSC Least Squares Collocation.

MAPSTER MAssive Parallel Approximation of Static and Time-VariablE Reference Surfaces with C^1-smooth Finite Element Model Functions.
MDT Mean Dynamic ocean Topography.
mpFRAGMENT Massive Parallel FRAmework for the Adjustment of Geodetic MEasureMENTs.
MPI Message Passing Interface.
MSS Mean Sea Surface.

NEQ normal equation.
NIC John von Neumann Institute for Computing.

OEQ observation equation.
OpenMP Open Multi-Processing.
OT Ocean Tides.

PARASURV PArametric determination of the dynamic ocean topography from geoid, altimetric sea surface heights and SAR derived RAdial SURface Velocities.
PSD Power Spectral Density.

RMS Root Mean Square error.
RSV Radial Surface Velocity.

SAR Synthetic Aperture Radar.
ScaLAPACK Scalable Linear Algebra PACKage.
SGG Satellite Gravitational Gradiometry.
SH Spherical Harmonic.
SLA Sea Level Anomaly.
SLATE Software for Linear Algebra Targeting Exascale.
SLR Satellite Laser Ranging.
SSH Sea Surface Height.
SST Satellite-to-Satellite Tracking.
STAMPED Statistical Testing and stochastic processes for the Analysis of Modeled and observed Earth system Data.
SWOT Surface Water and Ocean Topography.

TRA1 Modelling Transdisciplinary Research Area 1: Mathematics, Modelling and Simulation of Complex Systems.
TSC Total Surface Currents.
TVAR AR process of time varying coefficients.

TWS	Total Water Storage.
VCE	variance component estimation.
VLBI	Very Long Baseline Interferometry.
WV	wave.

Bibliography

Abulaitijiang, A., O. B. Andersen, R. Barzaghi, and P. Knudsen (2021). "Coastal Marine Gravity Modelling from Satellite Altimetry – Case Study in the Mediterranean." In: *Journal of Geodetic Science* 11.1, pp. 29–37. DOI: `10.1515/jogs-2020-0200`.

Agha Karimi, A., O. Baltazar Andersen, and X. Deng (2020). "Mean Sea Surface and Mean Dynamic Topography Determination from Cryosat-2 Data around Australia." In: *Advances in Space Research*. DOI: `10.1016/j.asr.2020.01.009`.

Ahlberg, J. H., E. N. Nilson, and J. L. Walsh (1967). *The Theory of Splines and Their Applications.* 1 . Mathematics in Science and Engineering v. 38. New York: Academic Press.

Albertella, A., R. Savcenko, T. Janjić, R. Rummel, W. Bosch, and J. Schröter (2012). "High Resolution Dynamic Ocean Topography in the Southern Ocean from GOCE." In: *Geophysical Journal International* 190.2, pp. 922–930. DOI: `10.1111/j.1365-246X.2012.05531.x`.

Albertella, A., R. Savcenko, W. Bosch, and R. Rummel (2008). *Dynamic Ocean Topography: The Geodetic Approach.* Tech. rep. 27. München: Institut für Astronomische und Physikalische Geodäsie, Technische Universität München.

Andersen, O. B. and P. Knudsen (2009). "DNSC08 Mean Sea Surface and Mean Dynamic Topography Models." In: *Journal of Geophysical Research: Oceans* 114.C11. DOI: `10.1029/2008JC005179`.

Andersen, O. B., P. Knudsen, and P. A. M. Berry (2010). "The DNSC08GRA Global Marine Gravity Field from Double Retracked Satellite Altimetry." In: *Journal of Geodesy* 84.3, pp. 191–199. DOI: `10.1007/s00190-009-0355-9`.

Andersen, O. B., P. Knudsen, and L. Stenseng (2015). "The DTU13 MSS (Mean Sea Surface) and MDT (Mean Dynamic Topography) from 20 Years of Satellite Altimetry." In: *IGFS 2014*. International Association of Geodesy Symposia. Springer, Cham, pp. 111–121. DOI: `10.1007/1345_2015_182`.

Andersen, O. B., S. K. Rose, A. Abulaitijiang, S. Zhang, and S. Fleury (2023). "The DTU21 Global Mean Sea Surface and First Evaluation." In: *Earth System Science Data* 15.9, pp. 4065–4075. DOI: `10.5194/essd-15-4065-2023`.

Andersen, O. B., S. Zhang, D. T. Sandwell, G. Dibarboure, W. H. F. Smith, and A. Abulaitijiang (2021). "The Unique Role of the Jason Geodetic Missions for High Resolution Gravity Field and Mean Sea Surface Modelling." In: *Remote Sensing* 13.4, p. 646. DOI: `10.3390/rs13040646`.

Argyris, J. H., I. Fried, and D. W. Scharpf (1968). "The TUBA Family of Plate Elements for the Matrix Displacement Method." In: *The Aeronautical Journal* 72.692, pp. 701–709. DOI: `10.1017/S000192400008489X`.

Arnold, D., T. Grombein, L. Schreiter, V. Sterken, and A. Jäggi (2023). "Reprocessed Precise Science Orbits and Gravity Field Recovery for the Entire GOCE Mission." In: *Journal of Geodesy* 97.7, p. 67. DOI: `10.1007/s00190-023-01752-y`.

Aviso (2020). *Along-Track Level-2+ (L2P) SLA Product Handbook.* Product Handbook SALP-MU-P-EA-23150-CLS. CNES/CLS.

Barthelmes, F. (2013). *Definition of Functionals of the Geopotential and Their Calculation from Spherical Harmonic Models.* Technical Report STR09/02. Potsdam, Germany: Deutsches GeoForschungsZentrum (GFZ). DOI: `10.2312/GFZ.b103-0902-26`.

Baur, O. (2013). “Greenland Mass Variation from Time-Variable Gravity in the Absence of GRACE.” In: *Geophysical Research Letters* 40.16, pp. 4289–4293. DOI: `10.1002/grl.50881`.

Baur, O., H. Bock, E. Höck, A. Jäggi, S. Krauss, T. Mayer-Gürr, T. Reubelt, C. Siemes, and N. Zehentner (2014). “Comparison of GOCE-GPS Gravity Fields Derived by Different Approaches.” In: *Journal of Geodesy* 88.10, pp. 959–973. DOI: `10.1007/s00190-014-0736-6`.

Becker, S., G. Freiwald, M. Losch, and W.-D. Schuh (2012). “Rigorous Fusion of Gravity Field, Altimetry and Stationary Ocean Models.” In: *Journal of Geodynamics*. Mass Transport and Mass Distribution in the System Earth 59–60, pp. 99–110. DOI: `10.1016/j.jog.2011.07.006`.

Beutler, G., A. Jäggi, L. Mervart, and U. Meyer (2010). “The Celestial Mechanics Approach: Application to Data of the GRACE Mission.” In: *Journal of Geodesy* 84.11, pp. 661–681. DOI: `10.1007/s00190-010-0402-6`.

Bingham, R. J. (2010). “Nonlinear Anisotropic Diffusive Filtering Applied to the Ocean’s Mean Dynamic Topography.” In: *Remote Sensing Letters* 1.4, pp. 205–212. DOI: `10.1080/01431161003743165`.

Bingham, R. J., P. Knudsen, O. Andersen, and R. Pail (2011). “An Initial Estimate of the North Atlantic Steady-State Geostrophic Circulation from GOCE.” In: *Geophysical Research Letters* 38.1, p. L01606. DOI: `10.1029/2010GL045633`.

Bingham, R. J., K. Haines, and C. W. Hughes (2008). “Calculating the Ocean’s Mean Dynamic Topography from a Mean Sea Surface and a Geoid.” In: *Journal of Atmospheric and Oceanic Technology* 25.10, pp. 1808–1822. DOI: `10.1175/2008JTECHO568.1`.

Blackford, L. S., J. Choi, A. Cleary, E. D’Azevedo, J. Demmel, I. Dhillon, J. Dongarra, S. Hammarling, G. Henry, A. Petitet, K. Stanley, D. Walker, and R. C. Whaley (1997). *ScaLAPACK Users Guide*. 2nd. Philadelphia: SIAM, Society for Industrial and Applied Mathematics.

Borlinghaus, M. (2021). “Schätzung eines kontinuierlichen raum-zeitlichen Modells der Mittleren Meereshöhe aus Altimeterbeobachtungen.” M.Sc. Thesis. Bonn, Germany: Universität Bonn.

Bosch, W. and R. Savcenko (2010). “On Estimating the Dynamic Ocean Topography – A Profile Approach.” In: *Gravity, Geoid and Earth Observation*. International Association of Geodesy Symposia. Springer, Berlin, Heidelberg, pp. 263–269. DOI: `10.1007/978-3-642-10634-7_34`.

Boxhammer, C. and W.-D. Schuh (2006). “GOCE Gravity Field Modeling: Computational Aspects - Free Kite Numbering Scheme.” In: *Observation of the Earth System from Space*. Ed. by J. Flury, R. Rummel, C. Reigber, M. Rothacher, G. Boedecker, and U. Schreiber. Berlin - Heidelberg: Springer Berlin Heidelberg, pp. 209–224.

Brockmann, J. M. (2014). “On High Performance Computing in Geodesy – Applications in Global Gravity Field Determination.” PhD thesis. Bonn, Germany: Institute of Geodesy and Geoinformation, University of Bonn.

Brockmann, J. M., N. Zehentner, E. Höck, R. Pail, I. Loth, T. Mayer-Gürr, and W.-D. Schuh (2014a). “EGM_TIM_RL05: An Independent Geoid with Centimeter Accuracy Purely Based on the GOCE Mission.” In: *Geophysical Research Letters* 41.22, pp. 8089–8099. DOI: `10.1002/2014GL061904`.

Brockmann, J. M., L. Roese-Koerner, and W.-D. Schuh (2014b). “A Concept for the Estimation of High-Degree Gravity Field Models in a High Performance Computing Environment.” In: *Studia Geophysica et Geodaetica* 58.4, pp. 571–594. DOI: `10.1007/s11200-013-1246-3`.

— (2014c). “Use of High Performance Computing for the Rigorous Estimation of Very High Degree Spherical Harmonic Gravity Field Models.” In: *Gravity, Geoid and Height Systems*. Ed. by U. Marti. International Association of Geodesy Symposia 141. Springer International Publishing, pp. 27–33. DOI: `10.1007/978-3-319-10837-7_4`.

Brockmann, J. M., T. Schubert, T. Mayer-Guerr, and W.-D. Schuh (2019c). *An Improved Global Gravity Field Model from the GOCE Mission: The Time-Wise Release 6 Model*. Talk at the EGU General Assembly. Vienna, Austria.

Brockwell, P. J. and R. A. Davis (2016). *Introduction to Time Series and Forecasting*. Springer Texts in Statistics. Cham: Springer International Publishing. DOI: `10.1007/978-3-319-29854-2`.

Bruinsma, S. L., C. Förste, O. Abrikosov, J.-M. Lemoine, J.-C. Marty, S. Mulet, M.-H. Rio, and S. Bonvalot (2014). “ESA’s Satellite-Only Gravity Field Model via the Direct Approach Based on All GOCE Data.” In: *Geophysical Research Letters* 41.21, 2014GL062045. DOI: `10.1002/2014GL062045`.

Bruinsma, S. L., C. Förste, O. Abrikosov, J.-C. Marty, M.-H. Rio, S. Mulet, and S. Bonvalot (2013). “The New ESA Satellite-Only Gravity Field Model via the Direct Approach.” In: *Geophysical Research Letters* 40.14, pp. 3607–3612. DOI: `10.1002/grl.50716`.

Chapron, B., F. Collard, and F. Ardhuin (2005). “Direct Measurements of Ocean Surface Velocity from Space: Interpretation and Validation.” In: *Journal of Geophysical Research: Oceans* 110.C7, n/a–n/a. DOI: `10.1029/2004JC002809`.

Chen, Q., Y. Shen, O. Francis, W. Chen, X. Zhang, and H. Hsu (2018). “Tongji-Grace02s and Tongji-Grace02k: High-Precision Static GRACE-Only Global Earth’s Gravity Field Models Derived by Refined Data Processing Strategies.” In: *Journal of Geophysical Research: Solid Earth* 123.7, pp. 6111–6137. DOI: `10.1029/2018JB015641`.

Ciarlet, P. G. (1978a). *The Finite Element Method for Elliptic Problems*. Studies in Mathematics and Its Applications v. 4. Amsterdam ; New York : New York: North-Holland Pub. Co. ; sole distributors for the U.S.A. and Canada, Elsevier North-Holland.

— (1978b). *The Finite Element Method for Elliptic Problems*. Studies in Mathematics and Its Applications v. 4. Amsterdam ; New York : New York: North-Holland Pub. Co. ; sole distributors for the U.S.A. and Canada, Elsevier North-Holland.

Clough, R. and J. Toche (1966). *Finite Element Stiffness Matrices for Analysis of Plate Bending*. Tech. rep. AFFDL-TR-66-80. Air Force Flight Dynamics Laboratory; University of California, Berkeley, pp. 515–545.

CLS (2016). *Sentinel-1 Product Definition*. Technical Document S1-RS-MDA-52-7441 Issue 3.4. Collecte Localisation Satellites (CLS), p. 129.

Consiglio, D. C. (2020). *WOC North Atlantic 2-D Merged SSH/SST Currents*. DOI: `10.12770/E84FE404-1ED3-4E6F-9B72-F75CD8EB7F7D`.

Čunderlík, R., K. Mikula, and M. Tunega (2013). “Nonlinear Diffusion Filtering of Data on the Earth’s Surface.” In: *Journal of Geodesy* 87.2, pp. 143–160. DOI: `10.1007/s00190-012-0587-y`.

Dahle, C., M. Murböck, F. Flechtner, H. Dobslaw, G. Michalak, K. H. Neumayer, O. Abrykosov, A. Reinhold, R. König, R. Sulzbach, and C. Förste (2019). “The GFZ GRACE RL06 Monthly Gravity Field Time Series: Processing Details and Quality Assessment.” In: *Remote Sensing* 11.18, p. 2116. DOI: `10.3390/rs11182116`.

De Boor, C. (2001). *A Practical Guide to Splines: With 32 Figures*. Rev. ed. Applied Mathematical Sciences v. 27. New York: Springer.

Dettmering, D., M. Schmidt, R. Heinkelmann, and M. Seitz (2011). “Combination of Different Space-Geodetic Observations for Regional Ionosphere Modeling.” In: *Journal of Geodesy* 85.12, pp. 989–998. DOI: `10.1007/s00190-010-0423-1`.

Dilalos, S. and J. D. Alexopoulos (2023). “Regional Gravity Model of Greece Based on Satellite, Marine and Terrestrial Data.” In: *Pure and Applied Geophysics* 180.7, pp. 2807–2826. DOI: `10.1007/s00024-023-03285-z`.

Ditmar, P., P. Visser, and R. Klees (2003). “On the Joint Inversion of SGG and SST Data from the GOCE Mission.” In: *Adv. Geosci.* 1, pp. 87–94. DOI: `10.5194/adgeo-1-87-2003`.

Döll, P., M. Fritsche, A. Eicker, and H. M. Schmied (2014). “Seasonal Water Storage Variations as Impacted by Water Abstractions: Comparing the Output of a Global Hydrological Model with GRACE and GPS Observations.” In: *Surveys in Geophysics* 35.6, pp. 1311–1331. DOI: `10.1007/s10712-014-9282-2`.

Domínguez, V. and F.-J. Sayas (2008). “Algorithm 884: A Simple Matlab Implementation of the Argyris Element.” In: *ACM Trans. Math. Softw.* 35.2, 16:1–16:11. DOI: `10.1145/1377612.1377620`.

Ducet, N., P. Y. Le Traon, and G. Reverdin (2000). "Global High-Resolution Mapping of Ocean Circulation from TOPEX/Poseidon and ERS-1 and -2." In: *Journal of Geophysical Research: Oceans* 105.C8, pp. 19477–19498. DOI: `10.1029/2000JC900063`.

Durmaz, M. and M. O. Karslioglu (2015). "Regional Vertical Total Electron Content (VTEC) Modeling Together with Satellite and Receiver Differential Code Biases (DCBs) Using Semi-Parametric Multivariate Adaptive Regression B-splines (SP-BMARS)." In: *Journal of Geodesy* 89.4, pp. 347–360. DOI: `10.1007/s00190-014-0779-8`.

Engen, G. and H. Johnsen (2010). *Sentinel-1 Doppler and Ocean Radial Velocity (RVL) Algorithm Definition (v1.2).* Technical Report S1-TN-NRT-53-0658. Tromsø, Norway: Norut, Northern Research Institute, p. 62.

Engwirda, D. (2017). "JIGSAW-GEO (1.0): Locally Orthogonal Staggered Unstructured Grid Generation for General Circulation Modelling on the Sphere." In: *Geoscientific Model Development* 10.6, pp. 2117–2140. DOI: `10.5194/gmd-10-2117-2017`.

— (2019). *JIGSAW(GEO) https://github.com/dengwirda/jigsaw-geo-matlab.*

ESA (2020). *ESA GOCE Online Dissemination.*

European Space Agency (2018). *Airborne Altimetry, Gravity, Lidar and Magnetic Data.* DOI: `10.5270/esa-8ffoo3e`.

Fahrmeir, L., T. Kneib, S. Lang, and B. D. Marx (2021). *Regression: Models, Methods and Applications.* 2nd edition 2021. Berlin: Springer Berlin.

Farahani, H. H., P. Ditmar, R. Klees, X. Liu, Q. Zhao, and J. Guo (2013). "The Static Gravity Field Model DGM-1S from GRACE and GOCE Data: Computation, Validation and an Analysis of GOCE Mission's Added Value." In: *Journal of Geodesy* 87.9, pp. 843–867. DOI: `10.1007/s00190-013-0650-3`.

Farrell, S. L., D. C. McAdoo, S. W. Laxon, H. J. Zwally, D. Yi, A. Ridout, and K. Giles (2012). "Mean Dynamic Topography of the Arctic Ocean." In: *Geophysical Research Letters* 39.1, p. L01601. DOI: `10.1029/2011GL050052`.

Fernández, J., H. Peter, C. Fernández, J. Berzosa, M. Fernández, L. Bao, M. Á. Muñoz, S. Lara, E. Terradillos, P. Féménias, and C. Nogueira (2024). "The Copernicus POD Service." In: *Advances in Space Research* 74.6, pp. 2615–2648. DOI: `10.1016/j.asr.2024.02.056`.

Flechtner, F., C. Reigber, R. Rummel, and G. Balmino (2021). "Satellite Gravimetry: A Review of Its Realization." In: *Surveys in Geophysics* 42.5, pp. 1029–1074. DOI: `10.1007/s10712-021-09658-0`.

Floberghagen, R., M. Fehringer, D. Lamarre, D. Muzi, B. Frommknecht, C. Steiger, J. Piñeiro, and A. da Costa (2011). "Mission Design, Operation and Exploitation of the Gravity Field and Steady-State Ocean Circulation Explorer Mission." In: *Journal of Geodesy* 85.11, pp. 749–758. DOI: `10.1007/s00190-011-0498-3`.

Forsberg, R., H. Skourup, O. B. Andersen, P. Knudsen, S. Laxon, A. Ridout, J. Johannesen, F. Siegismund, H. Drange, C. C. Tscherning, D. Arabelos, A. Braun, and V. Renganathan (2007). *Combination of Spaceborne, Airborne and In-Situ Gravity Measurements in Support of Arctic Sea Ice Thickness Mapping.* Report.

Förste, C., S. Bruinsma, O. Abrikosov, S. Rudenko, J.-M. Lemoine, J.-C. Marty, K. H. Neumayer, and R. Biancale (2016). *EIGEN-6S4 A Time-Variable Satellite-Only Gravity Field Model to d/o 300 Based on LAGEOS, GRACE and GOCE Data from the Collaboration of GFZ Potsdam and GRGS Toulouse.* DOI: `10.5880/icgem.2016.008`.

Förste, C., S. Bruinsma, O. Abrikosov, J.-M. Lemoine, J. C. Marty, F. Flechtner, G. Balmino, F. Barthelmes, and R. Biancale (2014). *EIGEN-6C4 The Latest Combined Global Gravity Field Model Including GOCE Data up to Degree and Order 2190 of GFZ Potsdam and GRGS Toulouse.* DOI: `10.5880/icgem.2015.1`.

Förste, C., R. Schmidt, R. Stubenvoll, F. Flechtner, U. Meyer, R. König, H. Neumayer, R. Biancale, J.-M. Lemoine, S. Bruinsma, S. Loyer, F. Barthelmes, and S. Esselborn (2008). "The GeoForschungsZentrum Potsdam/Groupe de Recherche de Gèodésie Spatiale Satellite-Only and

Combined Gravity Field Models: EIGEN-GL04S1 and EIGEN-GL04C." In: *Journal of Geodesy* 82.6, pp. 331–346. DOI: `10.1007/s00190-007-0183-8`.

Foster, E. L., T. Iliescu, and D. R. Wells (2014). "A Conforming Finite Element Discretization of the Streamfunction Form of the Unsteady Quasi-Geostrophic Equations." In: *arXiv:1405.7836 [math]*. arXiv: `1405.7836 [math]`.

Foster, E. L. (2013). "Finite Elements for the Quasi-Geostrophic Equations of the Ocean." PhD thesis. Blacksburg, Virginia: Virginia Polytechnica Institute and State University.

Fu, L.-L. (2014). "Ocean Surface Topography." In: *Encyclopedia of Remote Sensing*. Ed. by E. G. Njoku. Encyclopedia of Earth Sciences Series. Springer New York, pp. 455–461. DOI: `10.1007/978-0-387-36699-9_167`.

Gates, M., A. Charara, J. Kurzak, A. YarKhan, M. A. Farhan, D. Sukkari, and J. Dongarra (2020). *SLATE Users' Guide*. SLATE Working Notes 10, ICL-UT-19-01. Innovative Computing Laboratory, University of Tennessee.

Gates, M., J. Kurzak, A. Charara, A. YarKhan, and J. Dongarra (2019). "SLATE: Design of a Modern Distributed and Accelerated Linear Algebra Library." In: *Proceedings of the International Conference for High Performance Computing, Networking, Storage and Analysis*. SC '19. New York, NY, USA: Association for Computing Machinery, pp. 1–18. DOI: `10.1145/3295500.3356223`.

Gatti, A., M. Reguzzoni, F. Migliaccio, and F. Sansò (2016). "Computation and Assessment of the Fifth Release of the GOCE-only Space-Wise Solution." In: *1st Joint Commission 2 and IGFS Meeting*. Thessaloniki, Greece: Poster. DOI: `10.13140/RG.2.2.28625.94569`.

George, A. and J. W. H. Liu (1981). *Computer Solution of Large Sparse Positive Definite Systems*. Prentice-Hall Series in Computational Mathematics. Englewood Cliffs, N.J: Prentice-Hall.

Gerlach, C., N. Sneeuw, P. Visser, and D. Švehla (2003). "CHAMP Gravity Field Recovery Using the Energy Balance Approach." In: *Adv. Geosci.* 1, pp. 73–80. DOI: `10.5194/adgeo-1-73-2003`.

Gerlach, C. and R. Rummel (2013). "Global Height System Unification with GOCE: A Simulation Study on the Indirect Bias Term in the GBVP Approach." In: *Journal of Geodesy* 87.1, pp. 57–67. DOI: `10.1007/s00190-012-0579-y`.

Gilardoni, M., M. Reguzzoni, and A. Albertella (2015). "Global Mean Dynamic Topography Based on GOCE Data and Wiener Filters." In: *EGU General Assembly Conference Abstracts*. Vol. 17, p. 8216.

Gilbert, J. R., C. Moler, and R. Schreiber (1992). "Sparse Matrices in MATLAB: Design and Implementation." In: *SIAM Journal on Matrix Analysis and Applications* 13.1, pp. 333–356. DOI: `10.1137/0613024`.

Gonzalez, F. I., C. L. Rufenach, and R. A. Shuchman (1981). "Ocean Surface Current Detection by Synthetic Aperture Radar." In: *Oceanography from Space*. Marine Science. Springer, Boston, MA, pp. 511–523. DOI: `10.1007/978-1-4613-3315-9_59`.

Greenwood, J. A., A. Nathan, G. Neumann, W. J. Pierson, F. C. Jackson, and T. E. Pease (1969). "Radar Altimetry from a Spacecraft and Its Potential Applications to Geodesy." In: *Remote Sensing of Environment* 1.1, pp. 59–70. DOI: `10.1016/S0034-4257(69)90099-6`.

Gruber, T., C. Gerlach, and R. Haagmans (2012). "Intercontinental Height Datum Connection with GOCE and GPS-levelling Data." In: *Journal of Geodetic Science* 2.4, pp. 270–280. DOI: `10.2478/v10156-012-0001-y`.

Gruber, T., P. N. a. M. Visser, C. Ackermann, and M. Hosse (2011). "Validation of GOCE Gravity Field Models by Means of Orbit Residuals and Geoid Comparisons." In: *Journal of Geodesy* 85.11, pp. 845–860. DOI: `10.1007/s00190-011-0486-7`.

Hahn, H. G. (1975). *Methode Der Finiten Elemente in Der Festigkeitslehre*. Frankfurt am Main: Akademische Verlagsgesellschaft.

Hajduch, G., P. Vincent, K. Cordier, R. Husson, C. Peureux, K. Schmidt, R. Piantanida, A. Recchia, N. Franceschi, A. Mouche, A. Grouazel, F. Collard, H. Johnsen, and G. Guitton (2021). *S-1A & S-1B Annual Performance Report for 2020*. Tech. rep.

Hajduch, G., P. Vincent, K. Cordier, R. Husson, C. Peureux, K. Schmidt, R. Piantanida, A. Recchia, N. Franceschi, A. Mouche, A. Grouazel, F. Collard, H. Johnsen, and G. Guitton (2022). *S-1A & S-1B Annual Performance Report for 2021.* Tech. rep.

Hansen, M. W., F. Collard, K. F. Dagestad, J. A. Johannessen, P. Fabry, and B. Chapron (2011). "Retrieval of Sea Surface Range Velocities From Envisat ASAR Doppler Centroid Measurements." In: *IEEE Transactions on Geoscience and Remote Sensing* 49.10, pp. 3582–3592. DOI: `10.1109/TGRS.2011.2153864`.

Harmening, C. and H. Neuner (2020). "A Spatio-Temporal Deformation Model for Laser Scanning Point Clouds." In: *Journal of Geodesy* 94.2, p. 26. DOI: `10.1007/s00190-020-01352-0`.

Hayes, M. H. (1996). *Statistical Digital Signal Processing and Modeling.* New York: John Wiley & Sons.

Heiskanen, W. A. and H. Moritz (1993). *Physical Geodesy.* reprint. Technical University, Graz: Institute of Physical Geodesy.

Hofmann-Wellenhof, B. and H. Moritz (2005). *Physical Geodesy.* Vienna: Springer.

Hwang, C., H.-Y. Hsu, and R.-J. Jang (2002). "Global Mean Sea Surface and Marine Gravity Anomaly from Multi-Satellite Altimetry: Applications of Deflection-Geoid and Inverse Vening Meinesz Formulae." In: *Journal of Geodesy* 76.8, pp. 407–418. DOI: `10.1007/s00190-002-0265-6`.

ICGEM (2017). *ICGEM International Center for Global Gravity Field Models.*

Ilk, K. H., J. Kusche, and S. Rudolph (2002). "A Contribution to Data Combination in Ill-Posed Downward Continuation Problems." In: *Journal of Geodynamics.* Earth's Gravity and Magnetic Fields from Space 33.1–2, pp. 75–99. DOI: `10.1016/S0264-3707(01)00056-4`.

Ince, E. S., F. Barthelmes, S. Reißland, K. Elger, C. Förste, F. Flechtner, and H. Schuh (2019). "ICGEM – 15 Years of Successful Collection and Distribution of Global Gravitational Models, Associated Services, and Future Plans." In: *Earth System Science Data* 11.2, pp. 647–674. DOI: `10.5194/essd-11-647-2019`.

Jäggi, A., H. Bock, U. Meyer, G. Beutler, and J. van den IJssel (2015). "GOCE: Assessment of GPS-only Gravity Field Determination." In: *Journal of Geodesy* 89.1, pp. 33–48. DOI: `10.1007/s00190-014-0759-z`.

Janjić, T., J. Schröter, A. Albertella, W. Bosch, R. Rummel, R. Savcenko, J. Schwabe, and M. Scheinert (2012). "Assimilation of Geodetic Dynamic Ocean Topography Using Ensemble Based Kalman Filter." In: *Journal of Geodynamics.* Mass Transport and Mass Distribution in the System Earth 59, pp. 92–98. DOI: `10.1016/j.jog.2011.07.001`.

Jason-3 Team (2021). *Jason-3 Products Handbook.* Product Handbook SALP-MU-M-OP-16118-CN. NASA/JPL/CNES/NOAA/EUMETSAT.

Jayne, S. R. (2006). "Circulation of the North Atlantic Ocean from Altimetry and the Gravity Recovery and Climate Experiment Geoid." In: *Journal of Geophysical Research: Oceans* 111.C3, p. C03005. DOI: `10.1029/2005JC003128`.

Jensen, L., A. Eicker, H. Dobslaw, T. Stacke, and V. Humphrey (2019). "Long-Term Wetting and Drying Trends in Land Water Storage Derived From GRACE and CMIP5 Models." In: *Journal of Geophysical Research: Atmospheres* 124.17-18, pp. 9808–9823. DOI: `10.1029/2018JD029989`.

Jin, T., J. Li, and W. Jiang (2016). "The Global Mean Sea Surface Model WHU2013." In: *Geodesy and Geodynamics.* Special Issue: Geodetic and Geophysical Observations and Applications and Implications 7.3, pp. 202–209. DOI: `10.1016/j.geog.2016.04.006`.

Johannessen, J. A., B. Chapron, F. Collard, V. Kudryavtsev, A. Mouche, D. Akimov, and K.-F. Dagestad (2008). "Direct Ocean Surface Velocity Measurements from Space: Improved Quantitative Interpretation of Envisat ASAR Observations." In: *Geophysical Research Letters* 35.22. DOI: `10.1029/2008GL035709`.

Johannessen, J. A., B. Chapron, F. Collard, and B. Backeberg (2014). "Use of SAR Data to Monitor the Greater Agulhas Current." In: *Remote Sensing of the African Seas.* Springer, Dordrecht, pp. 251–262. DOI: `10.1007/978-94-017-8008-7_13`.

Jousset, S. (2023). *Mean Dynamic Topography MDT CNES_CLS 2022*. DOI: `10.24400/527896/A01-2023.003`.

Kaula, W. M. et al. (1970). *The Terrestrial Environment: Solid-Earth and Ocean Physics*. Massachusetts Institute of Technology NASA CR-1579. Williams College, Williamstown, Massachusetts: Massachusetts Institute of Technology, National Aeronautics and Space Administration, p. 158.

Keller, W. (2008). *Wavelets in Geodesy and Geodynamics*. De Gruyter.

Keller, W. and A. Borkowski (2019). "Thin Plate Spline Interpolation." In: *Journal of Geodesy* 93.9, pp. 1251–1269. DOI: `10.1007/s00190-019-01240-2`.

Klees, R., D. C. Slobbe, and H. H. Farahani (2018). "A Methodology for Least-Squares Local Quasi-Geoid Modelling Using a Noisy Satellite-Only Gravity Field Model." In: *Journal of Geodesy* 92.4, pp. 431–442. DOI: `10.1007/s00190-017-1076-0`.

— (2019). "How to Deal with the High Condition Number of the Noise Covariance Matrix of Gravity Field Functionals Synthesised from a Satellite-Only Global Gravity Field Model?" In: *Journal of Geodesy* 93.1, pp. 29–44. DOI: `10.1007/s00190-018-1136-0`.

Kleiner, B., R. D. Martin, and D. J. Thomson (1979). "Robust Estimation of Power Spectra." In: *Journal of the Royal Statistical Society. Series B (Methodological)* 41.3, pp. 313–351. DOI: `10.1111/j.2517-6161.1979.tb01087.x`. JSTOR: `2985062`.

Knudsen, P., O. B. Andersen, N. Maximenko, and J. Hafner (2022). *A New Combined Mean Dynamic Topography Model – DTUUH22MDT*. Poster Presented at the LPS2022. Bonn, Germany.

Knudsen, P., R. Bingham, O. Andersen, and M.-H. Rio (2011). "A Global Mean Dynamic Topography and Ocean Circulation Estimation Using a Preliminary GOCE Gravity Model." In: *Journal of Geodesy* 85.11, pp. 861–879. DOI: `10.1007/s00190-011-0485-8`.

Koch, K.-R. and J. Kusche (2002). "Regularization of Geopotential Determination from Satellite Data by Variance Components." In: *Journal of Geodesy* 76.5, pp. 259–268. DOI: `10.1007/s00190-002-0245-x`.

Koch, K.-R. (1999). *Parameter Estimation and Hypothesis Testing in Linear Models*. 2nd ed. Berlin, Heidelberg: Springer Berlin Heidelberg.

Köhler, J., C. Esch, K. Gutjahr, and W.-D. Schuh (2019). "Eine Nivellement gestützte Methode zur Erzeugung langer DInSAR Zeitreihen mittels B-Splines." In: DOI: `10.15488/4518`.

König, R., Z. Chen, C. Reigber, and P. Schwintzer (1999). "Improvement in Global Gravity Field Recovery Using GFZ-1 Satellite Laser Tracking Data." In: *Journal of Geodesy* 73.8, pp. 398–406. DOI: `10.1007/s001900050259`.

Krasbutter, I., J. M. Brockmann, B. Kargoll, W.-D. Schuh, H. Goiginger, and R. Pail (2011). "Refinement of the Stochastic Model of GOCE Scientific Data in a Long Time Series." In: *4th International GOCE User Workshop*. Munich, Germany.

Krasbutter, I., J. M. Brockmann, B. Kargoll, and W.-D. Schuh (2014). "Adjustment of Digital Filters for Decorrelation of GOCE SGG Data." In: *Observation of the System Earth from Space - CHAMP, GRACE, GOCE and Future Missions*. Ed. by F. Flechtner, N. Sneeuw, and W.-D. Schuh. Advanced Technologies in Earth Sciences. Springer Berlin Heidelberg, pp. 109–114. DOI: `10.1007/978-3-642-32135-1_14`.

Kurtenbach, E., A. Eicker, T. Mayer-Gürr, M. Holschneider, M. Hayn, M. Fuhrmann, and J. Kusche (2012). "Improved Daily GRACE Gravity Field Solutions Using a Kalman Smoother." In: *Journal of Geodynamics*. Mass Transport and Mass Distribution in the System Earth 59–60, pp. 39–48. DOI: `10.1016/j.jog.2012.02.006`.

Kurzak, J., P. Wu, M. Gates, I. Yamazaki, P. Luszczek, G. Ragghianti, and J. Dongarra (2017). *Designing SLATE: Software for Linear Algebra Targeting Exascale*. SLATE Working Notes 3, ICL-UT-17-06. Innovative Computing Laboratory, University of Tennessee.

Kusche, J. and R. Klees (2002). "Regularization of Gravity Field Estimation from Satellite Gravity Gradients." In: *Journal of Geodesy* 76.6-7, pp. 359–368. DOI: `10.1007/s00190-002-0257-6`.

Kusche, J., V. Klemann, and N. Sneeuw (2014). “Mass Distribution and Mass Transport in the Earth System: Recent Scientific Progress Due to Interdisciplinary Research.” In: *Surveys in Geophysics* 35.6, pp. 1243–1249. DOI: `10.1007/s10712-014-9308-9`.

Kvas, A., S. Behzadpour, M. Ellmer, B. Klinger, S. Strasser, N. Zehentner, and T. Mayer-Gürr (2019a). “ITSG-Grace2018: Overview and Evaluation of a New GRACE-Only Gravity Field Time Series.” In: *Journal of Geophysical Research: Solid Earth* 124.8, pp. 9332–9344. DOI: `10.1029/2019JB017415`.

Kvas, A. and T. Mayer-Gürr (2019). “GRACE Gravity Field Recovery with Background Model Uncertainties.” In: *Journal of Geodesy* 93.12, pp. 2543–2552. DOI: `10.1007/s00190-019-01314-1`.

Landerer, F. W., F. M. Flechtner, H. Save, F. H. Webb, T. Bandikova, W. I. Bertiger, S. V. Bettadpur, S. H. Byun, C. Dahle, H. Dobslaw, E. Fahnestock, N. Harvey, Z. Kang, G. L. H. Kruizinga, B. D. Loomis, C. McCullough, M. Murböck, P. Nagel, M. Paik, N. Pie, S. Poole, D. Strekalov, M. E. Tamisiea, F. Wang, M. M. Watkins, H.-Y. Wen, D. N. Wiese, and D.-N. Yuan (2020). “Extending the Global Mass Change Data Record: GRACE Follow-On Instrument and Science Data Performance.” In: *Geophysical Research Letters* 47.12, e2020GL088306. DOI: `10.1029/2020GL088306`.

Lasser, M. (2023). “Noise Modelling for GRACE Follow-On Observables in the Celestial Mechanics Approach.” Single. Bern: Universität Bern. DOI: `10.48549/4127`.

Li, W.-K., Q.-L. Mu, M. Yang, W. Feng, and M. Zhong (2023). “Iterative Approaches for Regional Moho Determination Using On-Orbit Gravity Gradients: A Case Study in Qinghai–Tibet Plateau and Its near Zone.” In: *Geophysical Journal International* 235.1, pp. 765–777. DOI: `10.1093/gji/ggad281`.

Lieb, V., M. Schmidt, D. Dettmering, and K. Börger (2016). “Combination of Various Observation Techniques for Regional Modeling of the Gravity Field.” In: *Journal of Geophysical Research: Solid Earth* 121.5, pp. 3825–3845. DOI: `10.1002/2015JB012586`.

Löcher, A. (2010). “Möglichkeiten Der Nutzung Kinematischer Satellitenbahnen Zur Bestimmung Des Gravitationsfeldes Der Erde.” PhD thesis. Bonn, Germany: Institute of Geodesy and Geoinformation, University of Bonn.

Löcher, A. and J. Kusche (2020). “A Hybrid Approach for Recovering High-Resolution Temporal Gravity Fields from Satellite Laser Ranging.” In: *Journal of Geodesy* 95.1, p. 6. DOI: `10.1007/s00190-020-01460-x`.

Lück, C., J. Kusche, R. Rietbroek, and A. Löcher (2018). “Time-Variable Gravity Fields and Ocean Mass Change from 37 Months of Kinematic Swarm Orbits.” In: *Solid Earth* 9.2, pp. 323–339. DOI: `10.5194/se-9-323-2018`.

Lumpkin, R. and M. Pazos (2007). “Measuring Surface Currents with Surface Velocity Program Drifters: The Instrument, Its Data, and Some Recent Results‖. Chapter Two of Lagrangian Analysis.” In: *Lagrangian Analysis and Prediction of Coastal and Ocean Dynamics*. University Press.

Madsen, S. N. (1989). “Estimating the Doppler Centroid of SAR Data.” In: *IEEE Transactions on Aerospace and Electronic Systems* 25.2, pp. 134–140. DOI: `10.1109/7.18675`.

Maier, A., S. Krauss, W. Hausleitner, and O. Baur (2012). “Contribution of Satellite Laser Ranging to Combined Gravity Field Models.” In: *Advances in Space Research* 49.3, pp. 556–565. DOI: `10.1016/j.asr.2011.10.026`.

Maximenko, N., P. Niiler, L. Centurioni, M.-H. Rio, O. Melnichenko, D. Chambers, V. Zlotnicki, and B. Galperin (2009). “Mean Dynamic Topography of the Ocean Derived from Satellite and Drifting Buoy Data Using Three Different Techniques.” In: *Journal of Atmospheric and Oceanic Technology* 26.9, pp. 1910–1919. DOI: `10.1175/2009JTECHO672.1`.

Mayer-Gürr, T., K. H. Ilk, A. Eicker, and M. Feuchtinger (2005). “ITG-CHAMP01: A CHAMP Gravity Field Model from Short Kinematic Arcs over a One-Year Observation Period.” In: *Journal of Geodesy* 78.7-8, pp. 462–480. DOI: `10.1007/s00190-004-0413-2`.

Mayer-Gürr, T., S. Behzadpur, M. Ellmer, A. Kvas, B. Klinger, S. Strasser, and N. Zehentner (2018). *ITSG-Grace2018 - Monthly, Daily and Static Gravity Field Solutions from GRACE.* DOI: `10.5880/icgem.2018.003`.

Meissl, P. (1982). *Least Squares Adjustment A Modern Approach.* Tech. rep. 43. A-8010 Graz, Steyrergasse 30: Geodätische Institute der Technischen Universität Graz.

Moiseev, A., J. A. Johannessen, and H. Johnsen (2022). "Towards Retrieving Reliable Ocean Surface Currents in the Coastal Zone From the Sentinel-1 Doppler Shift Observations." In: *Journal of Geophysical Research: Oceans* 127.5, e2021JC018201. DOI: `10.1029/2021JC018201`.

Moiseev, A., H. Johnsen, M. W. Hansen, and J. A. Johannessen (2020a). "Evaluation of Radial Ocean Surface Currents Derived From Sentinel-1 IW Doppler Shift Using Coastal Radar and Lagrangian Surface Drifter Observations." In: *Journal of Geophysical Research: Oceans* 125.4, e2019JC015743. DOI: `10.1029/2019JC015743`.

Moiseev, A., H. Johnsen, J. A. Johannessen, F. Collard, and G. Guitton (2020b). "On Removal of Sea State Contribution to Sentinel-1 Doppler Shift for Retrieving Reliable Ocean Surface Current." In: *Journal of Geophysical Research: Oceans* 125.9, e2020JC016288. DOI: `10.1029/2020JC016288`.

Moritz, H. (1973). *Least-Squares Collocation.* Tech. rep. A 75. München: Deutsche Geodätische Komission.

— (1974). *Advanced Least-Squares Methods.* Tech. rep. 175. Columbus, Ohio: Ohio State University (OSU).

Mouche, A. A., F. Collard, B. Chapron, K. F. Dagestad, G. Guitton, J. A. Johannessen, V. Kerbaol, and M. W. Hansen (2012). "On the Use of Doppler Shift for Sea Surface Wind Retrieval From SAR." In: *IEEE Transactions on Geoscience and Remote Sensing* 50.7, pp. 2901–2909. DOI: `10.1109/TGRS.2011.2174998`.

Mulet, S., M.-H. Rio, H. Etienne, C. Artana, M. Cancet, G. Dibarboure, H. Feng, R. Husson, N. Picot, C. Provost, and P. T. Strub (2021a). "The New CNES-CLS18 Global Mean Dynamic Topography." In: *Ocean Science Discussions*, pp. 1–31. DOI: `10.5194/os-2020-117`.

— (2021b). "The New CNES-CLS18 Global Mean Dynamic Topography." In: *Ocean Science* 17.3, pp. 789–808. DOI: `10.5194/os-17-789-2021`.

Müller, J., R. Pail, and D. D. G. (Erdmessung) (2022). "Geodesy 2030." In: *zfv – Zeitschrift für Geodäsie, Geoinformation und Landmanagement*, pp. 1–12. DOI: `10.12902/zfv-0392-2022`.

Nerem, R. S., B. D. Beckley, J. T. Fasullo, B. D. Hamlington, D. Masters, and G. T. Mitchum (2018). "Climate-Change–Driven Accelerated Sea-Level Rise Detected in the Altimeter Era." In: *Proceedings of the National Academy of Sciences*, p. 201717312. DOI: `10.1073/pnas.1717312115`.

NERSC (2022). *Sentinel-1 IW Ocean Surface Current Radial Velocity over Agulhas Region from ESA WOC Project.* Tech. rep. V2.0. Plouzane, France: Obtained from CERSAT / Ifremer.

Neyers, C. (2017). "Integration von radialen SAR Doppler Ozeanoberflächengeschwindigkeitsmessungen in die Berechnung der Dynamischen Ozeantopographie." M.Sc. Thesis. Bonn, Germany: Universität Bonn.

Neyers, C., J. M. Brockmann, and W.-D. Schuh (2022c). *Can We Refine a Local Marine Geoid by Exploiting Sentinel-1 RVL Observations? – A Qualitative Study of the Agulhas Region WOC IW-mode Radial Surface VeLocity Data Set.* Talk at Frontiers of Geodetic Science. Essen, Germany.

Oppenheim, A. V., R. W. Schafer, and J. R. Buck (1999). *Discrete-Time Signal Processing.* 2nd ed. Upper Saddle River, N.J: Prentice Hall.

Pail, R., T. Fecher, D. Barnes, J. F. Factor, S. A. Holmes, T. Gruber, and P. Zingerle (2018). "Short Note: The Experimental Geopotential Model XGM2016." In: *Journal of Geodesy* 92.4, pp. 443–451. DOI: `10.1007/s00190-017-1070-6`.

Pail, R., H. Goiginger, W.-D. Schuh, E. Höck, J. M. Brockmann, T. Fecher, T. Gruber, T. Mayer-Gürr, J. Kusche, A. Jäggi, and D. Rieser (2010). "Combined Satellite Gravity Field Model

GOCO01S Derived from GOCE and GRACE." In: *Geophysical Research Letters* 37, p. L20314. DOI: `10.1029/2010GL044906`.

Pail, R. and G. Plank (2003). "Comparison of Numerical Solution Strategies for Gravity Field Recovery from GOCE SGG Observations Implemented on a Parallel Platform." In: *Advances in Geosciences* 1, pp. 39–45. DOI: `10.5194/adgeo-1-39-2003`.

Pail, R., R. Bingham, C. Braitenberg, H. Dobslaw, A. Eicker, A. Güntner, M. Horwath, E. Ivins, L. Longuevergne, I. Panet, and B. Wouters (2015). "Science and User Needs for Observing Global Mass Transport to Understand Global Change and to Benefit Society." In: *Surveys in Geophysics* 36.6, pp. 743–772. DOI: `10.1007/s10712-015-9348-9`.

Pail, R., S. Bruinsma, F. Migliaccio, C. Förste, H. Goiginger, W.-D. Schuh, E. Höck, M. Reguzzoni, J. M. Brockmann, O. Abrikosov, M. Veicherts, T. Fecher, R. Mayrhofer, I. Krasbutter, F. Sansò, and C. C. Tscherning (2011). "First GOCE Gravity Field Models Derived by Three Different Approaches." In: *Journal of Geodesy* 85.11, p. 819. DOI: `10.1007/s00190-011-0467-x`.

Pail, R., T. Fecher, D. Barnes, J. Factor, S. Holmes, T. Gruber, and Zingerle Philipp (2017). *The Experimental Gravity Field Model XGM2016*. DOI: `10.5880/ICGEM.2017.003`.

Pavlis, N. K., S. A. Holmes, S. C. Kenyon, and J. K. Factor (2012). "The Development and Evaluation of the Earth Gravitational Model 2008 (EGM2008)." In: *Journal of Geophysical Research: Solid Earth* 117.B4, B04406. DOI: `10.1029/2011JB008916`.

Peter, H., U. Meyer, M. Lasser, and A. Jäggi (2022). "COST-G Gravity Field Models for Precise Orbit Determination of Low Earth Orbiting Satellites." In: *Advances in Space Research* 69.12, pp. 4155–4168. DOI: `10.1016/j.asr.2022.04.005`.

Plag, H.-P. and M. R. Pearlman (2009). *Global Geodetic Observing System: Meeting the Requirements of a Global Society on a Changing Planet in 2020*. Berlin: Springer.

Pujol, M.-I., Y. Faugère, G. Taburet, S. Dupuy, C. Pelloquin, M. Ablain, and N. Picot (2016). "DUACS DT2014: The New Multi-Mission Altimeter Data Set Reprocessed over 20 Years." In: *Ocean Science* 12.5, pp. 1067–1090. DOI: `10.5194/os-12-1067-2016`.

Pujol, M.-I., P. Schaeffer, Y. Faugère, M. Raynal, G. Dibarboure, and N. Picot (2018). "Gauging the Improvement of Recent Mean Sea Surface Models: A New Approach for Identifying and Quantifying Their Errors." In: *Journal of Geophysical Research: Oceans* 123.8, pp. 5889–5911. DOI: `10.1029/2017JC013503`.

Qiu, B., S. Chen, P. Klein, J. Wang, H. Torres, L.-L. Fu, and D. Menemenlis (2018). "Seasonality in Transition Scale from Balanced to Unbalanced Motions in the World Ocean." In: *Journal of Physical Oceanography* 48.3, pp. 591–605. DOI: `10.1175/JPO-D-17-0169.1`.

Reigber, C., G. Balmino, P. Schwintzer, R. Biancale, A. Bode, J.-M. Lemoine, R. König, S. Loyer, H. Neumayer, J.-C. Marty, F. Barthelmes, F. Perosanz, and S. Y. Zhu (2003). "Global Gravity Field Recovery Using Solely GPS Tracking and Accelerometer Data from Champ." In: *Space Science Reviews* 108.1, pp. 55–66. DOI: `10.1023/A:1026217713133`.

Reigber, C., P. Schwintzer, and H. Lühr (1999). "The CHAMP Geopotential Mission." In: *Bolletino di Geofisica Teorica ed Applicata* 40.3-4, pp. 285–289.

Reigber, C., G. Balmino, P. Schwintzer, R. Biancale, A. Bode, J.-M. Lemoine, R. König, S. Loyer, H. Neumayer, J.-C. Marty, F. Barthelmes, F. Perosanz, and S. Y. Zhu (2002). "A High-Quality Global Gravity Field Model from CHAMP GPS Tracking Data and Accelerometry (EIGEN-1S)." In: *Geophysical Research Letters* 29.14, pp. 37-1-37–4. DOI: `10.1029/2002GL015064`.

Reigber, C., H. Lühr, P. Schwintzer, and J. Wickert, eds. (2005). *Earth Observation with CHAMP: Results from Three Years in Orbit*. Berlin ; New York: Springer.

Rio, M.-H., S. Guinehut, and G. Larnicol (2011). "New CNES-CLS09 Global Mean Dynamic Topography Computed from the Combination of GRACE Data, Altimetry, and in Situ Measurements." In: *Journal of Geophysical Research: Oceans* 116.C7, p. C07018. DOI: `10.1029/2010JC006505`.

Rio, M.-H. and F. Hernandez (2004). “A Mean Dynamic Topography Computed over the World Ocean from Altimetry, in Situ Measurements, and a Geoid Model.” In: *Journal of Geophysical Research: Oceans* 109.C12, p. C12032. DOI: `10.1029/2003JC002226`.

Rio, M.-H., S. Mulet, and N. Picot (2014). “Beyond GOCE for the Ocean Circulation Estimate: Synergetic Use of Altimetry, Gravimetry, and in Situ Data Provides New Insight into Geostrophic and Ekman Currents.” In: *Geophysical Research Letters* 41.24, 2014GL061773. DOI: `10.1002/2014GL061773`.

Rio, M.-H., P.-M. Poulain, A. Pascual, E. Mauri, G. Larnicol, and R. Santoleri (2007). “A Mean Dynamic Topography of the Mediterranean Sea Computed from Altimetric Data, in-Situ Measurements and a General Circulation Model.” In: *Journal of Marine Systems*. Marine Environmental Monitoring and Prediction 65.1, pp. 484–508. DOI: `10.1016/j.jmarsys.2005.02.006`.

Roemmich, D. H., R. E. Davis, S. C. Riser, W. B. Owens, R. L. Molinari, S. L. Garzoli, and G. C. Johnson (2003). *The Argo Project. Global Ocean Observations for Understanding and Prediction of Climate Variability.* Tech. rep. SCRIPPS INSTITUTION OF OCEANOGRAPHY LA JOLLA CA, SCRIPPS INSTITUTION OF OCEANOGRAPHY LA JOLLA CA.

Romeiser, R., J. Johannessen, B. Chapron, F. Collard, V. Kudryavtsev, H. Runge, and S. Suchandt (2010). “Direct Surface Current Field Imaging from Space by Along-Track InSAR and Conventional SAR.” In: *Oceanography from Space*. Springer, Dordrecht, pp. 73–91. DOI: `10.1007/978-90-481-8681-5_5`.

Rothacher, M., D. Angermann, T. Artz, W. Bosch, H. Drewes, M. Gerstl, R. Kelm, D. König, R. König, B. Meisel, H. Müller, A. Nothnagel, N. Panafidina, B. Richter, S. Rudenko, W. Schwegmann, M. Seitz, P. Steigenberger, S. Tesmer, V. Tesmer, and D. Thaller (2011). “GGOS-D: Homogeneous Reprocessing and Rigorous Combination of Space Geodetic Observations.” In: *Journal of Geodesy* 85.10, pp. 679–705. DOI: `10.1007/s00190-011-0475-x`.

Rummel, R., G. Balmino, J. Johannessen, P. Visser, and P. Woodworth (2002). “Dedicated Gravity Field Missions—Principles and Aims.” In: *Journal of Geodynamics*. Earth’s Gravity and Magnetic Fields from Space 33.1–2, pp. 3–20. DOI: `10.1016/S0264-3707(01)00050-3`.

Rummel, R. (2001). “Global Unification of Height Systems and GOCE.” In: *Gravity, Geoid and Geodynamics 2000*. Ed. by F. Sansò and M. G. Sideris. Vol. 123. Berlin, Heidelberg: Springer Berlin Heidelberg, pp. 13–20. DOI: `10.1007/978-3-662-04827-6_3`.

— (2020). “Earth’s Gravity from Space.” In: *Rendiconti Lincei. Scienze Fisiche e Naturali*. DOI: `10.1007/s12210-020-00889-8`.

Rummel, R., W. Yi, and C. Stummer (2011). “GOCE Gravitational Gradiometry.” In: *Journal of Geodesy* 85.11, p. 777. DOI: `10.1007/s00190-011-0500-0`.

Sánchez-Reales, J. M., O. B. Andersen, and M. I. Vigo (2016). “Improving Surface Geostrophic Current from a GOCE-Derived Mean Dynamic Topography Using Edge-Enhancing Diffusion Filtering.” In: *Pure and Applied Geophysics* 173.3, pp. 871–884. DOI: `10.1007/s00024-015-1050-9`.

Schaeffer, P., Y. Faugére, J. F. Legeais, A. Ollivier, T. Guinle, and N. Picot (2012). “The CNES_CLS11 Global Mean Sea Surface Computed from 16 Years of Satellite Altimeter Data.” In: *Marine Geodesy* 35.sup1, pp. 3–19. DOI: `10.1080/01490419.2012.718231`.

Schaeffler, P., M.-I. Pujol, A. Faugère, A. Guillot, and N. Picot (2016). *New Mean Sea Surface CNES CLS 2015 Focusing on the Use of Geodetic Missions of Cryosat-2 and Jason-1*. Poster. Talk. La Rochelle, France.

Scheinert, M., F. Ferraccioli, J. Schwabe, R. Bell, M. Studinger, D. Damaske, W. Jokat, N. Aleshkova, T. Jordan, G. Leitchenkov, D. D. Blankenship, T. M. Damiani, D. Young, J. R. Cochran, and T. D. Richter (2016). “New Antarctic Gravity Anomaly Grid for Enhanced Geodetic and Geophysical Studies in Antarctica.” In: *Geophysical Research Letters* 43.2, pp. 600–610. DOI: `10.1002/2015GL067439`.

Schmidt, M., M. Fengler, T. Mayer-Gürr, A. Eicker, J. Kusche, L. Sánchez, and S.-C. Han (2007). “Regional Gravity Modeling in Terms of Spherical Base Functions.” In: *Journal of Geodesy* 81.1, pp. 17–38. DOI: `10.1007/s00190-006-0101-5`.

Schuh, W.-D. (1984). *Analyse Und Konvergenzbeschleunigung Der Methode Der Konjugierten Gradienten Bei Geodätischen Netzen.* Tech. rep. 49. Graz, Austria.

Schuh, W.-D. (1996). *Tailored Numerical Solution Strategies for the Global Determination of the Earth’s Gravity Field.* Tech. rep. 81. Graz, Austria: TU Graz.

Schuh, W.-D., J. M. Brockmann, B. Kargoll, I. Krasbutter, and R. Pail (2010). “Refinement of the Stochastic Model of GOCE Scientific Data and Its Effect on the In-Situ Gravity Field Solution.” In: *ESA Living Planet Symposium.* Bergen: SP-686.

Schuh, W.-D., S. Müller, and J. M. Brockmann (2015). “Completion of Band-Limited Data Sets on the Sphere.” In: *The 1st International Workshop on the Quality of Geodetic Observation and Monitoring Systems (QuGOMS’11).* Ed. by H. Kutterer, F. Seitz, H. Alkhatib, and M. Schmidt. International Association of Geodesy Symposia 140. Springer International Publishing, pp. 171–178. DOI: `10.1007/978-3-319-10828-5_25`.

Schuh, W.-D. (2016). “Signalverarbeitung in der Physikalischen Geodäsie.” In: *Handbuch der Geodäsie.* Ed. by W. Freeden and R. Rummel. Springer Reference Naturwissenschaften. Springer Berlin Heidelberg, pp. 1–49. DOI: `10.1007/978-3-662-46900-2_15-1`.

Sentinel-1-Team (2013). *Sentinel-1 User Handbook 1.0.* Tech. rep.

Shutler, J. D., G. D. Quartly, C. J. Donlon, S. Sathyendranath, T. Platt, B. Chapron, J. A. Johannessen, F. Girard-Ardhuin, P. D. Nightingale, D. K. Woolf, and J. L. Høyer (2016). “Progress in Satellite Remote Sensing for Studying Physical Processes at the Ocean Surface and Its Borders with the Atmosphere and Sea Ice.” In: *Progress in Physical Geography* 40.2, pp. 215–246. DOI: `10.1177/0309133316638957`.

Siegismund, F. (2013). “Assessment of Optimally Filtered Recent Geodetic Mean Dynamic Topographies.” In: *Journal of Geophysical Research: Oceans* 118.1, pp. 108–117. DOI: `10.1029/2012JC008149`.

Siegismund, F. (2020). “A Spectrally Consistent Globally Defined Geodetic Mean Dynamic Ocean Topography.” In: *Journal of Geophysical Research: Oceans* 125.7. DOI: `10.1029/2019JC016031`.

Siemes, C. (2018a). *GOCE Level 1B Gravity Gradient Processing Algorithms.* Technical Report 3397. European Space Agency.

— (2018b). “Improving GOCE Cross-Track Gravity Gradients.” In: *Journal of Geodesy* 92.1, pp. 33–45. DOI: `10.1007/s00190-017-1042-x`.

Siemes, C., M. Rexer, and R. Haagmans (2019a). “GOCE Star Tracker Attitude Quaternion Calibration and Combination.” In: *Advances in Space Research* 63.3, pp. 1133–1146. DOI: `10.1016/j.asr.2018.10.030`.

Siemes, C., M. Rexer, A. Schlicht, and R. Haagmans (2019b). “GOCE Gradiometer Data Calibration.” In: *Journal of Geodesy* 93.9, pp. 1603–1630. DOI: `10.1007/s00190-019-01271-9`.

Sneeuw, N., C. Lorenz, B. Devaraju, M. J. Tourian, J. Riegger, H. Kunstmann, and A. Bárdossy (2014). “Estimating Runoff Using Hydro-Geodetic Approaches.” In: *Surveys in Geophysics* 35.6, pp. 1333–1359. DOI: `10.1007/s10712-014-9300-4`.

Sośnica, K., A. Jäggi, U. Meyer, D. Thaller, G. Beutler, D. Arnold, and R. Dach (2015). “Time Variable Earth’s Gravity Field from SLR Satellites.” In: *Journal of Geodesy* 89.10, pp. 945–960. DOI: `10.1007/s00190-015-0825-1`.

Stewart, R. H. (2008). *Introduction to Physical Oceanography.* Tallahassee: Theorangegrove.

Sünkel, H. (1985). “Fourier Analysis of Geodetic Networks.” In: *Optimization and Design of Geodetic Networks.* Ed. by E. W. Grafarend and F. Sansò. Berlin, Heidelberg: Springer, pp. 257–300. DOI: `10.1007/978-3-642-70659-2_12`.

Taburet, G., A. Sanchez-Roman, M. Ballarotta, M.-I. Pujol, J.-F. Legeais, F. Fournier, Y. Faugere, and G. Dibarboure (2019). “DUACS DT2018: 25 Years of Reprocessed Sea Level Altimetry Products.” In: *Ocean Science* 15.5, pp. 1207–1224. DOI: `10.5194/os-15-1207-2019`.

Talpe, M. J., R. S. Nerem, E. Forootan, M. Schmidt, F. G. Lemoine, E. M. Enderlin, and F. W. Landerer (2017). "Ice Mass Change in Greenland and Antarctica between 1993 and 2013 from Satellite Gravity Measurements." In: *Journal of Geodesy* 91.11, pp. 1283–1298. DOI: `10.1007/s00190-017-1025-y`.

Tapley, B. D., D. P. Chambers, S. Bettadpur, and J. C. Ries (2003). "Large Scale Ocean Circulation from the GRACE GGM01 Geoid." In: *Geophysical Research Letters* 30.22, p. 2163. DOI: `10.1029/2003GL018622`.

Tapley, B. D., S. Bettadpur, J. C. Ries, P. F. Thompson, and M. M. Watkins (2004). "GRACE Measurements of Mass Variability in the Earth System." In: *Science* 305.5683, pp. 503–505. DOI: `10.1126/science.1099192`.

Taylor, M. A., B. A. Wingate, and L. P. Bos (2005). "Several New Quadrature Formulas for Polynomial Integration in the Triangle." In: *ArXiv e-prints.*

Traon, P. Y. L., F. Nadal, and N. Ducet (1998). "An Improved Mapping Method of Multisatellite Altimeter Data." In: *Journal of Atmospheric and Oceanic Technology* 15.2, pp. 522–534. DOI: `10.1175/1520-0426(1998)015<0522:AIMMOM>2.0.CO;2`.

Uebbing, B., J. Kusche, R. Rietbroek, and F. W. Landerer (2019). "Processing Choices Affect Ocean Mass Estimates From GRACE." In: *Journal of Geophysical Research: Oceans* 124.2, pp. 1029–1044. DOI: `10.1029/2018JC014341`.

Vergara, O., R. Morrow, M.-I. Pujol, G. Dibarboure, and C. Ubelmann (2023). "Global Submesoscale Diagnosis Using Along-Track Satellite Altimetry." In: *Ocean Science* 19.2, pp. 363–379. DOI: `10.5194/os-19-363-2023`.

Vianna, M. L. and V. V. Menezes (2010). "Mean Mesoscale Global Ocean Currents from Geodetic Pre-GOCE MDTs with a Synthesis of the North Pacific Circulation." In: *Journal of Geophysical Research: Oceans* 115.C2, p. C02016. DOI: `10.1029/2009JC005494`.

Volkov, D. L. and V. Zlotnicki (2012). "Performance of GOCE and GRACE-derived Mean Dynamic Topographies in Resolving Antarctic Circumpolar Current Fronts." In: *Ocean Dynamics* 62.6, pp. 893–905. DOI: `10.1007/s10236-012-0541-9`.

Wackernagel, H. (2010). *Multivariate Geostatistics.* 3., rd ed. Softcover version of original hardcover edition 2003. Berlin: Springer Berlin.

Woodworth, P. L., M. Gravelle, M. Marcos, G. Wöppelmann, and C. W. Hughes (2015). "The Status of Measurement of the Mediterranean Mean Dynamic Topography by Geodetic Techniques." In: *Journal of Geodesy* 89.8, pp. 811–827. DOI: `10.1007/s00190-015-0817-1`.

Wu, H., J. Müller, and P. Brieden (2017). *The GOCE-only Global Gravity Field Model IfE_GOCE05s.* DOI: `10.5880/ICGEM.2017.006`.

Wunsch, C. and E. M. Gaposchkin (1980). "On Using Satellite Altimetry to Determine the General Circulation of the Oceans with Application to Geoid Improvement." In: *Reviews of Geophysics* 18.4, pp. 725–745. DOI: `10.1029/RG018i004p00725`.

Wunsch, C. and D. Stammer (1998). "Satellite Altimetry, the Marine Geoid, and the Oceanic General Circulation." In: *Annual Review of Earth and Planetary Sciences* 26.1, pp. 219–253. DOI: `10.1146/annurev.earth.26.1.219`.

Yu, X., A. L. Ponte, N. Lahaye, Z. Caspar-Cohen, and D. Menemenlis (2021). "Geostrophy Assessment and Momentum Balance of the Global Oceans in a Tide- and Eddy-Resolving Model." In: *Journal of Geophysical Research: Oceans* 126.10, e2021JC017422. DOI: `10.1029/2021JC017422`.

Zehentner, N. and T. Mayer-Gürr (2016). "Precise Orbit Determination Based on Raw GPS Measurements." In: *Journal of Geodesy* 90.3, pp. 275–286. DOI: `10.1007/s00190-015-0872-7`.

Zingerle, P., R. Pail, T. Gruber, and X. Oikonomidou (2020). "The Combined Global Gravity Field Model XGM2019e." In: *Journal of Geodesy* 94.7, p. 66. DOI: `10.1007/s00190-020-01398-0`.